

SSC – 480

STRENGTH OF WELDED ALUMINUM IN TENSION



**Ship
Structure
Committee**

2025

This document has been approved
for public release and sale; its
distribution is unlimited.

This page intentionally left blank

Member Agencies:

*American Bureau of Shipping
Defence Research and Development Canada
Maritime Administration
Military Sealift Command
Naval Sea Systems Command
Office of Naval Research
Society of Naval Architects & Marine Engineers
Transport Canada
United States Coast Guard*



Ship
Structure
Committee

Address Correspondence to:

COMMANDANT (CG-ENG-2/SSC)
ATTN (EXECUTIVE DIRECTOR/SHIP
STRUCTURE COMMITTEE)
US COAST GUARD
2703 MARTIN LUTHER KING JR. AVE SE
WASHINGTON DC 20593-7509
Website: <http://www.shipstructure.org>

SSC – 480


SR – 1486


STRENGTH OF WELDED ALUMINUM IN TENSION

Proper understanding of the behavior of welded aluminum components is essential for ensuring the safety and reliability of aluminum marine vessels. These vessels consist of various configurations of welded stiffened panels whose tensile behavior may not be well characterized. The change of the mechanical properties across the heat affected zone (HAZ) of the welded component should be accounted for when quantifying the ultimate strength of the member. This quantification becomes more challenging with the presence of intersecting welds or when two different alloys, each with its own HAZ properties, are welded together.

This report discusses the results of an investigation into the tensile behavior of welded aluminum components. Experimental testing was conducted to characterize the load-deformation behavior of large-scale welded aluminum specimens and their ultimate tensile capacity. The specimens covered unstiffened and stiffened plates with transverse, longitudinal, and both stiffener types. Furthermore, coupons were extracted from a butt-welded plate to quantify the change in the mechanical properties across the heat affected zone and understand how this change can impact the behavior of the large-scale specimens. Detailed three-dimensional finite element analysis was conducted and utilized to develop better understanding of the behavior of the tested specimens. The results are discussed, and recommendations are made to achieve a more accurate prediction of the tensile capacity of these specimens.

We thank the authors and Project Technical Committee for their dedication and research toward completing the objectives and tasks detailed throughout this paper and continuing the Ship Structure Committee's mission to enhance the safety of life at sea.


W. R. ARGUIN
Rear Admiral, U.S. Coast Guard
Co-Chairman, Ship Structure Committee


P. D. SMALL
Rear Admiral, U.S. Navy
Co-Chairman, Ship Structure Committee

SHIP STRUCTURE COMMITTEE

RDML Wayne Arguin
U. S. Coast Guard Assistant Commandant
for Prevention Policy (CG-5P)
Co-Chair, Ship Structure Committee

RDML Peter Small
Chief Engineer and Deputy Commander
for Naval Systems Engineering (SEA05)
Co-Chair, Ship Structure Committee

Mr. Jeffrey Lantz
Director, Commercial Regulations and Standards (CG-5PS)
U.S. Coast Guard

Mr. Gareth Burton
Vice President, Technology
American Bureau of Shipping

Mr. H. Paul Cojeen
Society of Naval Architects and Marine Engineers

Dr. Malcolm Smith
Head, Warship Performance, DGSTCO
Defense Research & Development Canada - Atlantic

Mr. Kevin Kohlmann
Director, Office of Safety
Maritime Administration

Mr. Luc Tremblay
Executive Director, Domestic Vessel Regulatory Oversight
and Boating Safety, Transport Canada

Mr. Michael Haycock
Deputy Assistant Commandant for Engineering and
Logistics (CG-4D)
U.S. Coast Guard

Mr. Mark Lattner
Group Director, Ship Integrity and Performance Engineering
(SEA 05P)
Naval Sea Systems Command

Mr. Neil Lichtenstein
Deputy Director N7x, Engineering Directorate
Military Sealift Command

Dr. Thomas Fu
Director, Ship Systems and Engineering Research Division
Office of Naval Research

SHIP STRUCTURE EXECUTIVE GROUP & SUB-COMMITTEE

UNITED STATES COAST GUARD (CVE)
CAPT Jennifer Doherty
Mr. Charles Rawson

AMERICAN BUREAU OF SHIPPING
Dr. Qing Yu
Mr. Daniel LaMere
Ms. Christina Wang
Mr. Rich Delpizzo

**SOCIETY OF NAVAL ARCHITECTS AND MARINE
ENGINEERS**
Mr. Frederick Ashcroft
Dr. Roger Basu
Dr. Robert Sielski
Dr. Paul Miller

DEFENSE RESEARCH & DEVELOPMENT CANADA ATLANTIC
Dr. Mahmud Sazidy
Mr. Cameron Munro

MARITIME ADMINISTRATION
Mr. Todd Hiller
Mr. Todd Ripley
Mr. Digvijay Singh

TRANSPORT CANADA
Ms. Dorianne Aubin
Mr. Bashir Ahmed Golam
Ms. Tayyebe Seif

UNITED STATES COAST GUARD (FLEET)
CAPT Doug Graul
Mr. Martin Hecker
Mr. Timothy McAllister
Mr. Debu Ghosh

NAVSEA/NSWCCD
Mr. David Qualley
Mr. Dean Schleicher
Dr. Pradeep Sensharma
Mr. Michael McDonald

MILITARY SEALIFT COMMAND
Ms. Jeannette Viernes

OFFICE OF NAVAL RESEARCH
Dr. Jessica Dibelka

PROJECT TECHNICAL COMMITTEE MEMBERS

The Ship Structure Committee greatly appreciates the contributions of the individuals that volunteered their time to participate on the Project Technical Committee, listed below, and thanks them heartily. They were the subject matter expert representatives of the Ship Structure Committee to the contractor, performing technical oversight during contracting, advising the contractor in cognizant matters pertaining to the contract of which the agencies were aware, and performing technical peer review of the work in progress and upon completion.

Chair:

Mr. Charles Rawson, U.S. Coast Guard

Members:

Dr. Robert Sielski, Society of Naval Architecture and Marine Engineers

Dr. Jonah Klemm-Toole, Colorado School of Mines

Dr. Zhenzhen Yu, Colorado School of Mines

Dr. Paul Hess, StructRel Solutions

Mr. Debu Ghosh, U.S. Coast Guard

Mr. Spencer Johnson, Austal

Dr. Libin Miao, American Bureau of Shipping

Mr. Ajoy Kumar, BMT Designers & Planners

Ms. Jeannette Viernes, Military Sealift Command

Dr. Igor Chavez, University of Newcastle

Mr. Rod Sutherland, NDI Engineering

Ship Structure Committee Executive Director:

LCDR Bryan Andrews, U.S. Coast Guard

1. Report No. SSC-480		2. Government Accession No.		3. Recipient's Catalog No.	
4. Title and Subtitle Strength of Welded Aluminum in Tension				5. Report Date 3 June 2025	
				6. Performing Organization Code	
7. Author(s) Dr. Mohamed Soliman, Ph.D Alaaeldin T. Soliman				8. Performing Organization Report No. SR-1486	
9. Performing Organization Name and Address School of Civil & Environmental Engineering, Oklahoma State University 222 Engineering North, Stillwater, OK 74078				10. Work Unit No. (TRAIS)	
				11. Contract or Grant No.	
12. Sponsoring Agency Name and Address Ship Structure Committee C/O US Coast Guard 2703 Martin Luther King Jr. Ave. SE Washington, DC 20593-7509				13. Type of Report and Period Covered Final Report	
				14. Sponsoring Agency Code CG-5PS	
15. Supplementary Notes					
16. Abstract This report discusses the results of an investigation into the tensile behavior of welded aluminum components. Experimental testing was conducted to characterize the load-deformation behavior of large-scale welded aluminum specimens and their ultimate tensile capacity. The specimens covered unstiffened and stiffened plates with transverse, longitudinal, and both stiffener types. Furthermore, coupons were extracted from a butt-welded plate to quantify the change in the mechanical properties across the heat affected zone and understand how this change can impact the behavior of the large-scale specimens. Detailed three-dimensional finite element analysis was conducted and utilized to develop better understanding of the behavior of the tested specimens. The results are discussed, and recommendations are made to achieve a more accurate prediction of the tensile capacity of these specimens.					
17. Key Words Weld repair, aluminum, low-heat input			18. Distribution Statement Approved for public release; distribution is unlimited. Available from: National Technical Information Service Springfield, VA 22161 (703) 487-465		
19. Security Classif. (of this report) Unclassified		20. Security Classif. (of this page) Unclassified		21. No. of Pages 133	
22. Price					

Conversion Factors
(Approximate conversion to metric measures)

To convert from	to	Function	Value
LENGTH			
inches	meters	divide	39.3701
inches	millimeters	multiply by	25.4000
feet	meters	divide by	3.2808
VOLUME			
cubic feet	cubic meters	divide by	35.3149
cubic inches	cubic meters	divide by	61,024
SECTION MODULUS			
inches ² feet	centimeters ² meters	multiply by	1.9665
inches ² feet	centimeters ³	multiply by	196.6448
inches ³	centimeters ³	multiply by	16.3871
MOMENT OF INERTIA			
inches ² feet ²	centimeters ² meters ²	divide by	1.6684
inches ² feet ²	centimeters ⁴	multiply by	5993.73
inches ⁴	centimeters ⁴	multiply by	41.623
FORCE OR MASS			
long tons	tonnes	multiply by	1.0160
long tons	kilograms	multiply by	1016.047
pounds	tonnes	divide by	2204.62
pounds	kilograms	divide by	2.2046
pounds	Newtons	multiply by	4.4482
PRESSURE OR STRESS			
pounds/inch ²	Newtons/meter ² (Pascals)	multiply by	6894.757
kilo pounds/inch ²	mega Newtons/meter ² (mega Pascals)	multiply by	6.8947
BENDING OR TORQUE			
foot tons	meter tons	divide by	3.2291
foot pounds	kilogram meters	divide by	7.23285
foot pounds	Newton meters	multiply by	1.35582
ENERGY			
foot pounds	Joules	multiply by	1.355826
STRESS INTENSITY			
kilo pound/inch ² inch ^{1/2} (ksi ^{1/2} /in)	mega Newton MNm ^{3/2}	multiply by	1.0998
J-INTEGRAL			
kilo pound/inch	Joules/mm ²	multiply by	0.1753
kilo pound/inch	kilo Joules/m ²	multiply by	175.3



STRENGTH OF WELDED ALUMINUM IN TENSION

Prepared by

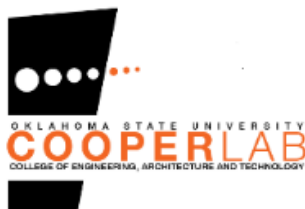
Dr. Mohamed Soliman, Ph.D., Associate Professor
School of Civil & Environmental Engineering, Oklahoma State University
222 Engineering North, Stillwater, OK 74078,
Phone: 405-744-9777, Email: mohamed.soliman@okstate.edu,
Website: <http://www.mohamedsoliman.info>

Alaaeldin T. Soliman, Former M.Sc. Student,
School of Civil & Environmental Engineering, Oklahoma State University

Submitted to

Ship Structure Committee

March 2024



ABSTRACT

This report discusses the results of an investigation into the tensile behavior of welded aluminum components. Experimental testing was conducted to characterize the load-deformation behavior of large-scale welded aluminum specimens and their ultimate tensile capacity. The specimens covered unstiffened and stiffened plates with transverse, longitudinal, and both stiffener types. Furthermore, coupons were extracted from a butt-welded plate to quantify the change in the mechanical properties across the heat affected zone and understand how this change can impact the behavior of the large-scale specimens. Detailed three-dimensional finite element analysis was conducted and utilized to develop better understanding of the behavior of the tested specimens. The results are discussed, and recommendations are made to achieve a more accurate prediction of the tensile capacity of these specimens.

EXECUTIVE SUMMARY

Proper understanding of the behavior of welded aluminum components is essential for ensuring the safety and reliability of aluminum marine vessels. These vessels consist of various configurations of welded stiffened panels whose tensile behavior may not be well characterized. The change of the mechanical properties across the heat affected zone (HAZ) of the welded component should be accounted for when quantifying the ultimate strength of the member. This quantification becomes more challenging with the presence of intersecting welds or when two different alloys, each with its own HAZ properties, are welded together.

The tensile behavior of these complex configurations has not been experimentally investigated in literature, especially on a larger scale closer to that adopted in ships. Therefore, a comprehensive testing program, covering AA5083-H116 and AA6061-T6511 alloys, was conducted to characterize the tensile behavior of welded components made of both alloys. Baseline information on the mechanical properties of the utilized alloys, and their HAZ, was established through small-scale coupon testing. Next, large-scale testing was conducted on specimens consisting of flat plates, in addition to plates with transversely welded stiffeners, longitudinally welded stiffeners, and with both stiffener types. In total, twelve large-scale specimens were tested with three replicas for each specimen type to shed some light on the uncertainty of the behavior. Numerical finite element analysis was conducted to develop a better understanding of the behavior of these welded specimens and identify the underlying parameters that govern the response. Available strength prediction models are evaluated and compared to the experimental results.

The experimental results showed the expected increase in strength that accompanies the addition of longitudinal stiffeners; however, the inclusion of transversally welded stiffener did not have a significant impact on the capacity of the AA5083 specimens. The experimental results, however, highlighted the drop in ductility that occurs for the specimens with both stiffener types. The conducted testing and analysis also showed that available strength prediction models may not provide consistent safety factors for different specimen types and highlighted the importance of considering strain compatibility when quantifying the ultimate tensile strength of some of these specimens.

ACKNOWLEDGMENTS

The authors gratefully acknowledge the financial support from the United States Coast Guard (USCG), Award number SR-1486. The authors would like to thank Mr. Charles Rawson, Naval Architecture Division of the USCG, and the Project Technical Committee for their guidance and help throughout the duration of the project. The contribution of AUSTAL, USA, in the form of donating the fabricated specimens that were essential for completing this research, is greatly acknowledged. Special thanks to Mr. Spencer Johnson and Mr. Shawn Wilber from AUSTAL, USA for their help during the design and fabrication phases of the project. The authors would also like to acknowledge W&W|AFCO STEEL for donating the fabricated steel grip assemblies. Finally, we would like to thank the team of graduate, undergraduate, and high school research assistants at Oklahoma State University who helped with the experimental program. This team included Cody James, Aditya Nayak, Seth Prizznick, Jacob Schindall, Cooper Waddell, Jaxson Spears, Della Thomas, Hunter Moulayiansis, Ahmad Shanawaz, Carter Israelson, Joshua Exline, Yassin Soliman, Jocelynn Swann, Diego Valencia, and Mr. David Porter, the lab supervisor for Bert Cooper Engineering Laboratory at Oklahoma State University.

TABLE OF CONTENTS

Section	Page
1 INTRODUCTION	1
2 LITERATURE REVIEW	4
2.1 MECHANICAL PROPERTIES ACROSS THE HAZ.....	4
2.2 RESIDUAL STRESSES AND THEIR DISTRIBUTION IN WELDED ALUMINUM JOINTS	7
2.3 VARIABILITY IN THE MECHANICAL PROPERTIES OF ALUMINUM ALLOYS ..	12
2.4 TENSILE STRENGTH PREDICTION OF WELDED ALUMINUM PANELS	16
2.4.1 Aluminum Design Methods.....	16
2.4.2 FE modelling for predicting the tensile strength of welded aluminum panels	17
3 EXPERIMENTAL TESTING PROGRAM	22
3.1 ANCILLARY TESTING.....	22
3.2 LARGE SCALE EXPERIMENTAL SETUP.....	24
3.2.1 Original Test Setup.....	24
3.2.1.1 Upper and Lower Steel Grip Assemblies.....	26
3.2.2 Updated Test Setup	28
3.2.3 Hydraulic System and Test Control	35
3.2.4 Test Matrix for the Large-Scale Testing Program.....	37
3.3 ALUMINUM SPECIMEN DESIGN.....	37
3.3.1 Flat Plate Specimens	40
3.3.2 Transverse Stiffener Specimens	41
3.3.3 Longitudinal Stiffener Specimens.....	43
3.3.4 Longitudinal and Transverse Stiffener Specimens	44
3.3.5 Connection between Steel End Plate and Aluminum End Plate	45
3.4 INSTRUMENTATION	46
3.5 TEST PROCEDURE	49
3.5.1 Ancillary Testing.....	49
3.5.2 Large-Scale Testing.....	50
3.6 TESTING OF THE INITIAL ALUMINUM SPECIMEN	51
4 EXPERIMENTAL RESULTS	54
4.1 ANCILLARY TESTING.....	54

4.2	LARGE-SCALE TESTING.....	61
4.2.1	Testing Results	61
4.2.1.1	Flat Plate Specimen Results.....	61
4.2.1.2	Transverse Stiffener Specimen Results	70
4.2.1.3	Longitudinal Stiffener Specimen Results	78
4.2.1.4	Longitudinal and Transverse Stiffener Specimen Results	86
5	FINITE ELEMENT MODELLING	95
5.1	MODEL GEOMETRY	95
5.2	MATERIAL MODELING.....	97
5.2.1	Aluminum Stress-Strain Behavior	97
5.2.2	Ductile Damage Model	99
5.3	OTHER MODEL ATTRIBUTES.....	100
5.4	FINITE ELEMENT MODELLING RESULTS	105
6	DISCUSSION.....	113
6.1	EFFECT OF SPECIMEN SIZE ON STRENGTH AND DUCTILITY	113
6.2	EFFECT OF WELDING ON THE BEHAVIOR OF WELDED ALUMINUM COMPONENTS	115
6.3	ULTIMATE STRENGTH PREDICTION	117
6.4	SIMPLIFICATIONS TO THE FINITE ELEMENT MODELING PROCEDURE	121
6.4.1	Effect of the residual stresses.....	122
6.4.2	Effect of modeling the weld lines	123
6.4.3	Simplified mechanical properties of the HAZ	125
7	CONCLUSIONS AND RECOMMENDATIONS FOR FUTURE WORK	128
7.1	CONCLUSIONS.....	128
7.2	RECOMMENDATIONS FOR FUTURE WORK	129
8	REFERENCES	131

LIST OF TABLES

Table	Page
Table 2.1: Magnitude and distribution of residual stresses in AA5083-H116 reported in literature	10
Table 2.2: Magnitude and distribution of residual stresses in AA6061-T6 reported in literature	11
Table 2.3: Mechanical properties of AA5083-H116.	15
Table 2.4: Mechanical properties of AA6061-T6.....	15
Table 3.1: Test matrix for the large-scale testing program.....	37
Table 3.2: Mechanical properties of AA5083-H116 utilized in specimen design.....	39
Table 3.3: Mechanical properties of AA6061-T6 utilized in specimen design.	39
Table 4.1: Stress-strain characteristics of AA5083-H116 HAZ coupons.....	57
Table 4.2: Stress-strain characteristics of AA6061-T6511 HAZ coupons	57
Table 4.3: Stress-strain characteristics of 5183 weld metal coupons	58
Table 4.4: Strength characteristics of AA5083-H116 BM Coupons	60
Table 4.5: Strength characteristics of AA6061-T6511 BM Coupons.....	60
Table 4.6: Results of flat plate specimens	61
Table 4.7: Results of Transverse Stiffener Specimens	71
Table 4.8: Results of Longitudinal Stiffener Specimens	79
Table 4.9: Results of Longitudinal and Transverse Stiffener Specimens.....	91
Table 5.1: Modified Ramberg-Osgood model parameters.	99
Table 6.1: Comparison of the specimen capacity obtained from the experimental results, FE modeling, and the <i>Aluminum Design Manual</i> (AA 2020).	118
Table 6.2: Comparison of the ultimate elongation between the experimental results and FEM.	121

LIST OF FIGURES

Figure	Page
Figure 2.1: Typical hardness profile of butt welded joint (adapted from Pérez et al. (2016)).	5
Figure 2.2: Illustrative figure showing the residual stress distribution from butt welds (a) deposition of butt weld, (b) contraction of butt weld, (c) restraint forces between BM and weld, (d) formation of longitudinal residual stresses, and (e) formation of transverse residual stresses (Gurney, 1979).	9
Figure 2.3: Stress-Strain curves for the HAZ of AA6061-T6 (adapted from Nazemi and Ghrib (2019)).	20
Figure 3.1: Dimensions of welded specimen for coupon testing in millimeters.	23
Figure 3.2: Dimensions of coupons that are to be cut using a waterjet in millimeters.	24
Figure 3.3: The 1,500 KN Universal Testing Machine.	25
Figure 3.4: 3D render of the original test setup showing various specimen components.	25
Figure 3.5: Original test setup with assembly in place.	26
Figure 3.6: 3D render for the Steel Grip Assembly.	27
Figure 3.7: Detailed dimensions of the Steel Grip Assembly in millimeters.	28
Figure 3.8: General layout of the updated test setup.	29
Figure 3.9: 3D render of the updated test setup showing various specimen components.	29
Figure 3.10: Overall dimensions of the updated test setup in millimeters.	30
Figure 3.11: Detailed layout of the modified steel grip assemblies (a) dimensions of the modified upper and lower steel grip plates in millimeters, and (b) 3D render of the modified upper steel grip plate.	30
Figure 3.12: Loading Beam (W16×89) with upper pin connection and the spacer.	31
Figure 3.13: Various components of Load Column 1.	32
Figure 3.14: Various components of Load Column 2.	32
Figure 3.15: Connection to the strong floor.	33
Figure 3.16: View of the lateral support system attached to the loading beam.	34
Figure 3.17: Closeup view on the roller bearing that accommodates the in-plane movement.	34
Figure 3.18: The updated test setup.	35
Figure 3.19: Components of the hydraulic system in Load Column 1.	36
Figure 3.20: Components of the hydraulic system in Load Column 2.	36
Figure 3.21: Comparison between the steel grip assemblies: (a) original test setup and (b) updated test setup.	38
Figure 3.22: General layout of the Flat Plate Specimen.	39
Figure 3.23: Dimensions of the main test plate in millimeters.	40

Figure 3.24: Dimensions of upper and lower aluminum end plate in millimeters.	41
Figure 3.25: Dimensions of the connection stiffeners in millimeters.	41
Figure 3.26: Dimensions of the flat plate specimen (in millimeters).	42
Figure 3.27: General layout of the transverse stiffener specimen (a) dimensions (in millimeters) and (b) 3D render of the T specimen.	42
Figure 3.28: Dimensions of the longitudinal stiffener in millimeters.	43
Figure 3.29: Dimensions of the smaller connection stiffeners found in L and LT Specimens.	43
Figure 3.30: General layout of the longitudinal stiffener specimen (a) dimensions (in millimeters) and (b) 3D render of the L specimen.	44
Figure 3.31: General layout of the longitudinal and transverse stiffener specimen (a) dimensions (in millimeters) and (b) 3D render of the LT specimen.	44
Figure 3.32: Dimensions of the steel plate washer in millimeters.	45
Figure 3.33: The utilized bolt assembly.	45
Figure 3.34: NI cDAQ-9178 with the different cards attached for recording data.	46
Figure 3.35: Location of the strain gauges for different types of specimens (a) F specimens, (b) T specimens, (c) L specimens, and (d) LT specimens.	47
Figure 3.36: Attachment of the LVDTs for different specimens (a) F specimens, (b) T specimens, (c) L specimens, and (d) LT specimens.	48
Figure 3.37: Components of the DIC system.	49
Figure 3.38: Components of the initial aluminum specimen (a) The initial aluminum specimen along with the BM and HAZ plates (b) The steel grip assembly.	51
Figure 3.39: The initial aluminum specimen during testing (a) location of the extensometer, (b) general view, and (c) location of the strain gauges.	52
Figure 3.40: Original test setup for the initial aluminum specimen.	53
Figure 3.41: Initial test specimen after failure: (a) general view and (b) close up view of the fracture surface.	53
Figure 4.1: Coupons used in ancillary testing (a) location of HAZ coupons after they were extracted from the welded specimen, (b) HAZ coupons for AA5083-H116, (c) HAZ coupons for AA6061-T6 (d) BM coupons for AA6061-T6 (e) BM coupons for AA5083-H116.	54
Figure 4.2: Close-up view for one of the AA5083-H116 HAZ coupons after the test was completed.	55
Figure 4.3: Stress-Strain curves across the HAZ for AA5083-H116.	55
Figure 4.4: Stress-Strain curves across the HAZ for AA6061-T6511.	56
Figure 4.5: Stress-Strain curves of the base metal coupons of AA5083-H116.	59
Figure 4.6: Stress-Strain curves of the base metal coupons of AA6061-T6511.	59
Figure 4.7: Load-deformation curves of flat plate specimens.	62
Figure 4.8: Flat plat specimen post failure (a) F1, (b) F2, and (c) F3.	64

Figure 4.9 Fracture surfaces of Specimen F3: (a) upper fracture surface and (b) lower fracture surface (other specimens showed similar behavior)	65
Figure 4.10: DIC results for specimen F1 (a) strain before the onset of serration, (b) strain at the onset of the first serration, and (c) strain towards the end of the test.	67
Figure 4.11: DIC results for specimen F2 (a) strain before the onset of serration, (b) strain at the onset of the first serration, and (c) strain towards the end of the test.	68
Figure 4.12: DIC results for specimen F1 (a) strain at the beginning of the test, (b) strain at the onset of the first serration, and (c) strain towards the end of the test.	69
Figure 4.13: Specimen F1 results: (a) load vs time showing the onset of serrations, and (b) strain vs time showing strain readings and how they react to the onset of serrations.	70
Figure 4.14: Load-deformation curves for all transverse stiffener specimens.....	71
Figure 4.15: Failure of the T specimens: (a) general location of failure, (b) upper fracture surface of Specimen T2, and (c) lower fracture surface of T2.....	72
Figure 4.16: Transverse stiffener specimen post failure (a) T1 (b) T2 (c) T3	74
Figure 4.17: DIC results for specimen T1 (a) strain before the onset of serrations, (b) strain at the onset of the first serration, and (c) strain towards the end of the test.	75
Figure 4.18: DIC results for specimen T2 (a) strain before the onset of serrations, (b) strain at the onset of the first serration, and (c) strain towards the end of the test.	76
Figure 4.19: DIC results for specimen T3 (a) strain before the onset of serrations, (b) strain at the onset of the first serration, and (c) strain towards the end of the test.	77
Figure 4.20: Load-deformation curves for all longitudinal stiffener specimens.	78
Figure 4.21 Failure surfaces of Specimen L2 (a) lower 5083 surface, (b) lower 6061 surface, (c) upper 5083 surface, and (d) upper 6061 surface.....	80
Figure 4.22: Longitudinal stiffener specimen post failure (a) L1 (b) L2 (c) L3.....	82
Figure 4.23: DIC results for specimen L1 (a) strain in the beginning of the test, (b) strain just before the onset of the first serration, and (c) strain after the single serration where the specimen failed shortly after. (The shown segment is the main test plate)	83
Figure 4.24: DIC results for specimen L2 (a) strain in the beginning of the test, (b) strain just before the onset of the first serration, and (c) strain after the single serration where the specimen failed shortly after. (Left segment is the main test plate and the right segment is the stiffener).....	84
Figure 4.25: DIC results for specimen L3 (a) strain in the beginning of the test, (b) strain just before the onset of the first serration, and (c) strain after the single serration where the specimen failed shortly after. (Left segment is the main test plate and the right segment is the stiffener).....	85
Figure 4.26: Load-deformation curves for all LT specimens.	86
Figure 4.27 Lower failure surface of Specimen LT2 with focus are covering: (a) the AA5083 failure surface and (b) the AA8061 surface.....	87
Figure 4.28: Longitudinal and transverse stiffener specimen post failure (a) LT1, (b) LT2, and (c) LT3.....	89

Figure 4.29: Failure of the LT specimen (a) fracture of the longitudinal stiffener and (b) necking of the stiffener on the other side of the fracture location.	90
Figure 4.30: DIC results of specimen LT 1 (a) strain in the beginning of the test, (b) strain in the middle of the test, and (c) strain before the end of the test. (Left segment is the main test plate and the right segment is the stiffener)	92
Figure 4.31: DIC results of specimen LT 2 (a) strain in the beginning of the test, (b) strain in the middle of the test, and (c) strain before the end of the test. (Left segment is the main test plate and the right segment is the stiffener)	93
Figure 4.32: DIC results of specimen LT 3 (a) strain in the beginning of the test, (b) strain in the middle of the test, and (c) strain before the end of the test. (Left segment is the main test plate and the right segment is the stiffener)	94
Figure 5.1: Model geometry of the F specimen (a) 3D view of the FE model, (b) different components in the FE model.....	95
Figure 5.2: Model geometry of the T specimen (a) 3D view of the FE model, (b) different components in the FE model.....	96
Figure 5.3: Model geometry of the L specimen (a) 3D view of the FE model, (b) different components in the FE model.....	96
Figure 5.4: Model geometry of the LT specimen (a) 3D view of the FE model, (b) different components in the FE model.....	97
Figure 5.5: Comparison between the original and modified Ramberg-Osgood model vs the experimental profile reported in Yun et al. (2021).	98
Figure 5.6: Illustrative figure for the Ductile Damage Model.	100
Figure 5.7: Meshing of different model components: (a) mesh orientation of the main test plate, (b) mesh orientation of the longitudinal stiffener, and (c) mesh orientation of the transverse stiffener found in T specimens.....	101
Figure 5.8: Tie constraint between connection stiffeners and main test plate.	101
Figure 5.9: Close-up view on the HAZ sectioning in the LT specimen FE model.....	102
Figure 5.10: Close-up view on the weld lines used to connect the different parts in the LT specimen FE model.	103
Figure 5.11: Boundary conditions across all FE models (a) bottom fixed support at the lower aluminum end plate, and (b) displacement applied from the upper aluminum end plate.	103
Figure 5.12: Predefined fields of residual stresses in L Specimen FE model.....	104
Figure 5.13: Internal and kinematic energy on one of the finite element models.	105
Figure 5.14: Finite element model results for flat plate specimens.	106
Figure 5.15: Behavior of flat plate specimen FE model (a) overall failure and (b) close-up view on the failure.	106
Figure 5.16: Finite element model results for transverse stiffener specimens.....	107

Figure 5.17: Comparison between the failure location of the experimental test and FE model in T specimens (a) failure of specimen T3 and (b) close-up view on the failure in the FE model.	108
Figure 5.18: Finite element model results for longitudinal stiffener specimens.....	109
Figure 5.19: Overall failure of longitudinal stiffener specimen FE model.....	109
Figure 5.20: Behavior of longitudinal stiffener specimen FE model (a) failure of the main test plate and (b) overall failure.....	110
Figure 5.21: Finite element model results for the LT specimens.	111
Figure 5.22: Overall failure of longitudinal and transverse stiffener specimen FE model.....	111
Figure 5.23: Behavior of the FE model of LT specimens (a) failure of the stiffener prior to the overall failure, (b) overall failure, and (c) failure of specimen T3 in the same manner (note the post failure orientation of the transverse stiffener that was captured by the FE model).	112
Figure 6.1: Stress-Strain curves of large scale and small-scale base metal tests of AA5083.....	113
Figure 6.2: Different shapes of serrations of AA5083 (a) close-up view on the shape of the serrations in the small-scale coupons (b) close-up on the shape of serrations in the large-scale flat plate specimen.	115
Figure 6.3: Visual appearance of serrations (a) closely spaced serrations in the small-scale coupons, and (b) widely spaced serrations in large-scale specimens.	115
Figure 6.4: Load-deformation curves for the average of each stiffener configuration.	117
Figure 6.5: Stress-strain profiles of different components governing the strength of the LT specimens.....	120
Figure 6.6: Load-defomration curves of Specimen T3 along with the original FE results and the FE results without residual stresses.	122
Figure 6.7: Load-defomration curves of Specimen L2 along with the original FE results and the FE results without residual stresses.	123
Figure 6.8: Load-defomration curves of Specimen T3 along with the original FE results and the FE results with no weld lines.	124
Figure 6.9: Load-defomration curves of Specimen L2 along with the original FE results and the FE results with no weld lines.	124
Figure 6.10: Load-defomration curves of Specimen LT3 along with the original FE results and the FE results with no weld lines.	125
Figure 6.11: Load-deformation curves of Specimen T3, the original FE model, and FE models with different HAZ zones assigned to the full extent of the HAZ.	126
Figure 6.12: Load-deformation curves showing the average LT specimen, the original FEM and FE models with different HAZ zones assigned to the full extent of the HAZ.....	127

1 INTRODUCTION

Aluminum alloys are widely used in marine structures due to their good formability, high strength-to-weight ratio, and lightweight characteristics. They also have high resistance to corrosion which makes them especially suitable for utilization in aggressive marine environments. Aluminum alloys used in marine structures include the 4xxx, 5xxx, and 6xxx series alloys. The 4xxx-series is an aluminum-silicon alloy used primarily in castings or as the weld filler metal for other aluminum alloys. The 5xxx-series is an aluminum-magnesium alloy with high corrosion resistance that is suitable for components in direct contact with sea water. The aluminum-magnesium-silicon 6xxx-series alloys are utilized to manufacture extruded sections with adequate corrosion resistance for marine environments. The widely used aluminum alloys in marine construction include AA5083-H116, AA6061-T6, AA6082, and AA5086. The AA5083-H116 is typically rolled and commonly utilized as the hull plate, while AA6061-T6 comes as extruded sections and is generally used for stiffeners.

Despite these appealing characteristics, the structural behavior and fabrication methods of aluminum structural components can be significantly different compared to those of traditional steel vessels. This can pose challenges associated with their use in ship building and requires more research to properly understand their behavior and develop appropriate design techniques that ensure the reliability and longevity of the vessel. A main factor that affects the behavior of aluminum alloys when utilized in ship building is the inferior mechanical properties of the weld heat affected zone (HAZ) of some alloys when compared to those of the base metal. The HAZ is the area within the structural component that is affected by the heat generated from the welding process. As a result of heating, the mechanical properties across the HAZ deteriorate due to the phase transformation of the hardening precipitates from the strong needle-like form (i.e., β'') to the granular, more porous form (i.e., β). This phase transformation is caused by the high, concentrated heat input applied to this small area (Torres & Vargas, 2013). The welding process also creates residual stress fields that get locked into the material and may affect the structural behavior under subsequent loading applied during the service life. For a typical stiffened panel, the welding process creates high tensile residual stresses at the stiffener weld lines and compressive stresses in between the stiffeners (Paik et al., 2008). The high tensile residual stresses around the welds may

promote the growth of cracks in the weld zone and may affect the load bearing capacity of the panel (Lu et al., 2020).

An additional challenge associated with aluminum design is the variability in the reported mechanical properties of commonly used alloys having the same temper and heat treatment. For example, Lakshminarayanan et al. (2009), Pérez et al. (2016), and Arun and Ramachandran (2015) reported a tensile yield strength ranging from 240 MPa (34.8 ksi) to 300 MPa (43.5 ksi) for AA6061-T6. The ultimate tensile strength for the same alloy ranged from 295 MPa (42.8 ksi) to 335 MPa (48.6 ksi) in these studies. Design codes and standards, e.g., *European Committee for Standardization (EN) 485-2* (CEN, 2013) and the *Aluminum Design Manual* published by the Aluminum Association (AA 2020) typically adopt conservative values of the mechanical properties to maintain an acceptable reliability level for the designed components. For this particular alloy (i.e., AA6061-T6), the EN 485-2 (CEN 2013) and the *Aluminum Design Manual* (AA 2020) specify yield and ultimate strengths of 240 MPa (34.8 ksi) and 290 MPa (42 ksi), respectively. This level of conservatism may unnecessarily increase the initial construction cost of the ship and increase its weight leading to higher running costs throughout the service life.

This variability in the mechanical properties can be attributed to several parameters that have been shown to impact the reported values of mechanical properties. These parameters include the strain rate of loading, specimen size, and rolling direction, among others. For instance, Zhang et al. (2022) studied the effect of the strain rate on the obtained mechanical properties of AA6061-T6. Tensile tests were conducted with strain rates ranging from 0.001/s to 4732/s. The reported yield strengths varied from 220 MPa (32 ksi) to 300 MPa (43.5 ksi) with the large increase in the strength occurring past a strain rate of 984/s. A study conducted by Clausen et al. (2001) investigated the effect of specimen geometry and rolling direction on the mechanical properties of AA6082 and AA7108. Large and small coupons were extracted from different rolling directions and tested under tensile loading. Both aluminum alloys showed a change in the yield strength when the coupon size changed. In addition, the mechanical properties exhibited a decrease in strength when the rolling direction shifted from 0° to 45° and an increase when it changes from 45° to 90°. Accordingly, in addition to the inherent randomness arising from the alloying process, more uncertainty in predicting the behavior is introduced due to the fabrication process and the testing procedure used to establish the mechanical properties.

Welding is the primary fabrication method used in ship construction. For aluminum ship construction, the weld filler metal may be weaker than the base metal or its HAZ; thus, the weld strength may govern the capacity of the connection. The welds in this case are referred to as under-matched welds. The fabrication of stiffened panels with longitudinal and transverse stiffeners requires weld lines in various orientations leading to the potential of intersecting welds and/or HAZs. Quantifying the strength of the panel in these situations becomes even more challenging. A recent study by Collette (2022) investigated, experimentally and through finite element modeling (FEM), the effect of undermatched welds on the tensile strength of aluminum plates with transversally welded stiffeners. The study concluded that these types of welds could pose a possible risk to ship hull girders due to the localization of plastic deformation in the undermatched regions. However, no analysis was conducted to investigate the effect of other welding orientations, also common in ship construction, on the tensile behavior of aluminum components.

To address this need, this report investigates, both experimentally and numerically, the behavior of large-scale welded aluminum components consisting of non-load carrying fillet welds, load carrying fillet welds, and a combination of both types. In this report, load carrying fillet welds refer to those welds transferring forces in the main direction of loading of the shell plate, while non load carrying welds do not participate in the primary load transfer mechanism. AA5083-H116 (ASTM B928) and AA6061-T6511 (ASTM B221) are the aluminum alloys covered in the research. The AA5083 aluminum alloy is used as the main plate material that is stiffened by AA6061 plates. Large-scale testing is conducted on four configurations of specimens: a flat plate specimen, longitudinally stiffened specimen, transversely stiffened specimen, and a specimen that combined both stiffener types. The change in the mechanical properties across the HAZ is investigated through an experimental testing program on small-scale coupons extracted from welded specimens. Finite element (FE) analysis is also conducted in ABAQUS environment to develop better understanding of the behavior. This FE analysis included the fillet weld lines, residual stresses, and variation of the mechanical properties across the HAZ. The report first discusses available literature, then presents the details of the experimental investigation and the finite element analysis. Finally, it discusses the results and investigates possible simplifications to the finite element procedure to reduce the computational cost of the analysis.

2 LITERATURE REVIEW

The non-heat-treated (5xxx-series) and the heat-treated (6xxx-series) aluminum alloys are used widely across the marine industry. The 5xxx-series alloys are primarily composed of aluminum and magnesium, while the 6xxx-series alloys mainly consist of aluminum, magnesium, and silicon. The 5xxx-series alloys are usually produced as rolled plates and they gain their strength after being strain hardened (cold rolled) at the mill. On the other hand, 6xxx-series components are usually produced as extruded shapes. The corrosion resistance of the 5xxx-series alloys is generally better than that of the 6xxx-series alloys. As a result, 5xxx-series are typically utilized in hull plating with the 6xxx-series alloys as extruded stiffeners that are welded to the plating. This construction configuration with two different aluminum alloys welded using a different filler metal, each with its own load-deformation behavior, poses a challenge in predicting the ultimate strength of welded aluminum panels under tensile loading. The issue of strength prediction is exacerbated by the high variability in the mechanical properties of the utilized materials and the significant impact of the welding process on the mechanical properties of some aluminum alloys. The following subsections discuss the key aspects that are involved in predicting the ultimate strength of welded aluminum stiffened panels.

2.1 MECHANICAL PROPERTIES ACROSS THE HAZ

The mechanical properties across the heat affected zone have a significant influence on the behavior of welded aluminum structures. After the welding process, the area in the vicinity of the welds can be divided into three zones: the weld zone (WZ), heat affected zone (HAZ), and the base metal (BM). The *Aluminum Design Manual* (AA 2020) defines the HAZ to extend 25 mm (1-in) from the centerline of the groove weld or the heel of a fillet weld. Several researchers investigated the change in the mechanical properties within the HAZ (e.g., Nazemi & Ghrib, 2019; Collette, 2022; Hakem et al., 2019; Du et al., 2022). Typical Vickers microhardness (ASTM, 2017) profiles reported in literature (e.g., Hernandez et al., 2013; Pérez et al., 2016; Ilman et al., 2020) show that the WZ and HAZ have lower hardness compared to that of the BM. Figure 2.1 shows a typical hardness profile for a butt weld joint completed with gas metal arc welding (GMAW) as reported in Pérez et al., (2016). These lower hardness values have been shown to correlate with low yield and ultimate tensile strengths for the relevant zones (Lakshminarayanan et al., 2009, Du et al., 2022).

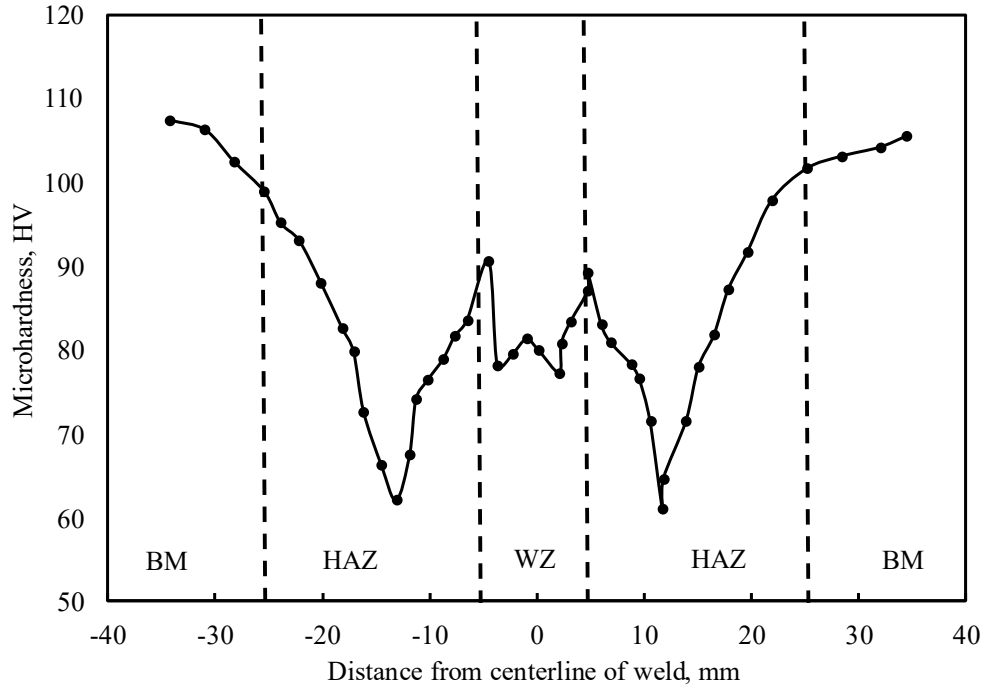


Figure 2.1: Typical hardness profile of butt welded joint (adapted from Pérez et al. (2016)).

The composition of aluminum alloys plays an important role in shaping their strength characteristics. This composition also leads to the deterioration in mechanical properties after welding. Magnesium and silicon, commonly used as alloying elements, react together forming a strengthening precipitate, Mg_2Si . This strengthening precipitate is dispersed homogeneously across the aluminum matrix (Lakshminarayanan et al., 2009) leading to an increase in the yield and ultimate tensile strengths. The welding process affects this strengthening precipitate leading to a change in the mechanical properties (Lakshminarayanan et al., 2009). In general, heat-treated and non-heat-treated alloys require a different choice of welding filler metal. Heat-treated alloys (e.g., 6xxx-series) use filler metals with a different chemical composition than their own to avoid hot cracking along the weld lines; especially at the HAZ (Arun & Ramachandran, 2015). Non-heat-treated alloys (e.g., 5xxx-series) can use a filler alloy that contains the same chemical compositions as the BM. A good example is the 4xxx-series filler alloys that have silicon added to reduce the melting point leading to more fluidity in the molten state (Arun & Ramachandran, 2015). However, for some 6xxx-series alloys, the additional silicon introduced from the filler metal during the welding process lowers the quantity of the Mg_2Si precipitate in the WZ and HAZ compared to the BM region. This goes to the fact that there is not enough magnesium available to react with this surplus amount of silicon to create the strengthening precipitate. As a result, the

mechanical properties in the WZ and HAZ deteriorate after fusion welding (Lakshminarayanan et al., 2009). When silicon becomes excessive in aluminum alloys, chances of intergranular corrosion increase which explains why the 6xxx series alloys are slightly less corrosion resistant than 5xxx series alloys (Davis, 2001).

Another reason that causes the decrease in strength and hardness across the HAZ is the existence of porosity after welding. Several studies have investigated the effect of porosity on the mechanical properties of welded aluminum connections. Liu et al. (2012) investigated the mechanical properties of AA5083 butt welds after being welded using gas tungsten arc welding (GTAW) and GMAW. Scanning electron microscopy (SEM) of both weldments showed the presence of considerable porosity in the GMAW weldment and no porosity in the GTAW weldment. Porosity can be attributed to the presence of hydrogen which is highly soluble in molten aluminum but is of low solubility in the solid state (Poolperm et al., 2020). Hydrogen can be sourced from the base metal, filler metal, and/or shielding gas. Huang et al. (2019) studied the metallurgical and mechanical properties of AA5083 GMAW groove welds for different plate thicknesses and concluded that increasing the plate thickness will in turn increase the porosity in the welded joints. Increasing the thickness will lead to more weld passes and faster solidification rates that may increase the porosity (Bakar et al., 2012).

Heat input also plays a critical role in determining the grain size within the HAZ and, in turn, the extent of deterioration in the mechanical properties. Welding processes such as GTAW and GMAW vary with respect to their heat input levels. GMAW generates more heat because direct current is used and its filler metal is always connected to the positive polarity; however, the GTAW uses alternating current and, thus, the heat input at one end of the electrode is maximum and minimum on the other end (Lakshminarayanan et al., 2009; Arun & Ramachandran, 2015). Accordingly, constant high heat generation is observed with GMAW, while varying heat generation is observed with GTAW. The constant heat generated with GMAW slows down the cooling rate because peak temperatures of the molten weld pool will be reached more frequently. Unfortunately, this creates a fusion zone with wide dendritic spacing leading to inferior mechanical properties (Lakshminarayanan et al., 2009). On the other hand, the heat generated during the GTAW is not as high; this results in a higher cooling rate creating narrower dendritic spacing in the fusion zone (Cruz et al., 2010). This zone possesses better mechanical properties as compared

to those found in the same region in the GMAW weldments (Lakshminarayanan et al., 2009). Bakar et al. (2012) studied the effect of double-sided welds on the microstructure of AA6061 GMAW welded plates. They concluded that the heat from the second pass, alongside the not fully dissipated heat of the first weld pass, altered the cooling rate and resulted in dissolving of the grain boundaries and the drop in the hardness values in those regions.

Although several researchers investigated the change of the mechanical properties across the HAZ, it is still challenging to characterize the stress-strain behavior at different locations across the HAZ. In literature, several studies correlate the change in the hardness across the HAZ to a corresponding change in the yield and ultimate strengths (e.g., Ilman et al., 2020; Pérez et al., 2016). However, such correlation is subjected to significant uncertainty and may not lead to the proper stress-strain profile of the studied region (Collette, 2022). Other researchers used the sectioning approach to characterize the change in mechanical properties across the HAZ (Wang et al. 2006). In this approach, thin coupons are extracted from the HAZ and subjected to tensile testing resulting in more accurate representation of the load-deformation behavior of different regions within the HAZ. More recent studies implemented digital image correlation (DIC) with virtual force method (VFM) to establish such characterization (Nazemi and Ghrib, 2019). In this report, characterizing the stress-strain profiles of different regions within the HAZ is established by extracting coupons from a welded specimens combining the two utilized alloys.

2.2 RESIDUAL STRESSES AND THEIR DISTRIBUTION IN WELDED ALUMINUM JOINTS

Residual stresses and distortion arise from the welding process of aluminum alloys. These stresses may affect the behavior of the welded aluminum component. Residual stresses are stresses that remain in the structural component after welding or fabrication. These stresses would be in the state of global force equilibrium as they are not caused by external loads. Most manufacturing processes result in the development of these stresses due to volume changes that accompany phase transformations, different cooling rates within the same component, and the differential plastic flow characteristics (Nazemi, 2015). The difference in cooling rate within the elements of the same component is the main contributor to the development of residual stresses during and after the welding process (Rossini et al., 2012). Typically, the external surfaces will cool at a faster rate compared to the heated part in the center of the section/plate. As the center of the heated region

starts to cool down, its contraction will be constrained by the cooler external surfaces leading to the development of compressive residual stresses on the external surfaces and tensile stresses at the center. Another factor that can lead to the development of these residual stresses is the localized non-uniform heating during the welding process which is related to the type of welding process and the skill of the welder (James, 2011).

Residual stresses can impact the structural integrity of welded panels subjected to tensile loads (Poolperm et al., 2020). The development of tensile residual stresses in welded connections increase the probability of crack initiation at the weld toe leading to a lower fatigue resistance (Fricke, 2005). Tensile residual stresses can also lead to stress concentration cracking that can be found in the weld ripples and at the start/stop position along longitudinal welds (Mutombo & Du, 2011). Compressive residual stresses, on the other hand, can reduce the propagation rate of cracks leading to a potential positive effect on the fatigue life of the component (Fricke, 2005; Rossini et al., 2012). The overall impact of residual stresses on the fatigue life of a component depends on the geometry, size of the structure, welding technique, material properties, and residual stress distribution.

Several studies in literature focused on quantifying the magnitude of residual stresses due to welding and their distribution. Zhang et al. (2009) concluded that the magnitude of residual stresses in the longitudinal direction of GTAW butt welds is higher than the magnitude in the transverse direction. Further from the weld line, the compressive residual stresses will need to balance out the tensile residual stresses located near the welding region. These tensile residual stresses in the longitudinal direction may reach the yield strength of the base metal in some cases. However, the residual stresses in the transverse direction depend on the welding procedure and the clamping condition of the plates at the far ends parallel to the weld. If it is free, then only compressive residual stresses will be induced due to the Poisson's effect supplementing the restrained longitudinal contraction. If it is clamped mechanically, which is the typical case, the compressive residual stresses induced from the Poisson's effect will get superimposed with some tensile stresses in the transverse direction (McClung, 2007). Figure 2.2 demonstrates the typical distribution of longitudinal and transverse residual stresses in a butt welded joint. Hosseinabadi and Khedmati (2021) compiled and summarized the welding imperfections and extent of the HAZ in their review study on the ultimate strength of welded aluminum structural elements. Following

a similar format, Table 2.1 and Table 2.2 compile existing information from literature regarding the magnitude and distribution of residual stresses in AA5083-H116 and AA6061-T6, respectively. Note that this research utilized T6511 temper; however, the mechanical properties of this temper are expected to be very similar to those of the T6 (ASTM B221).

Based on these tables, it is apparent that several studies reported a tensile residual stress due to welding of 67% of the yield stress of the base metal for AA5083. Some of these studies reported values for the compressive residual stresses outside the HAZ while others simply indicated that they balance out the tensile residual stresses. On the other hand, variability can be seen in the reported tensile residual stresses for the AA6061-T6 due to the different types of welds used (i.e., butt welds, fillet welds).

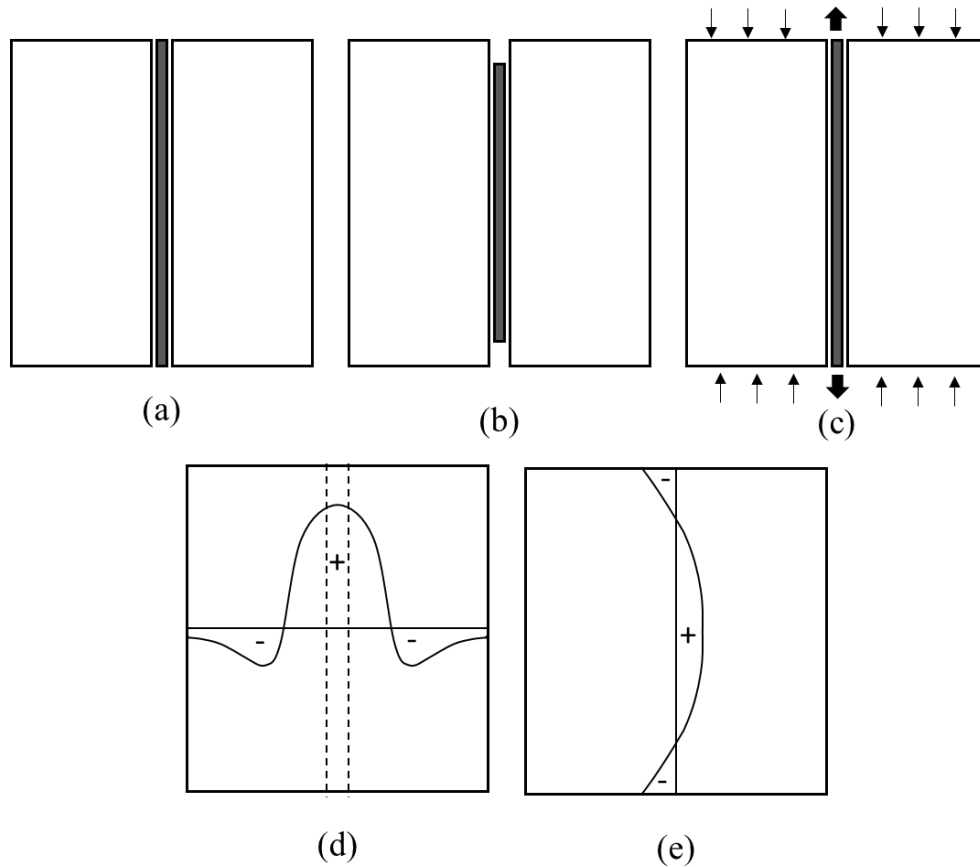


Figure 2.2: Illustrative figure showing the residual stress distribution from butt welds (a) deposition of butt weld, (b) contraction of butt weld, (c) restraint forces between BM and weld, (d) formation of longitudinal residual stresses, and (e) formation of transverse residual stresses (Gurney, 1979).

Table 2.1: Magnitude and distribution of residual stresses in AA5083-H116 reported in literature

Reference	Type of weld	Welding Residual Stress		Residual Stress Distribution	HAZ	
		Tensile, RTS ¹	Compressive, RCS ²		HAZ extent	$F_{y \text{ HAZ}}$
Zha and Moan (2001)	T Fillet Welds	$F_{y \text{ RTS}} = F_{y \text{ HAZ}}$	In equilibrium with forces arising from tensile residual stresses	<ul style="list-style-type: none"> Plate: Rectangular distribution with tension in HAZ and compression in BM Stiffener: Rectangular distribution with tension at weld tip and compression or tension based on tendon force 	25 mm for 5xxx series; 12.5 mm for 6xxx series (better to be determined by hardness test)	$F_{y \text{ HAZ}} = 0.67 F_{y \text{ BM}}$
Paik et al. (2005)	Metal Inert Gas (MIG) T Fillet Welds (8mm thick plate with 120 mm stiffener height)	$F_{y \text{ HAZ}} = 0.67 F_{y \text{ BM}}$ (plate and stiffener)	$F_{y \text{ HAZ}} = -0.12 F_{y \text{ BM}}$ (plate) $F_{y \text{ HAZ}} = -0.08 F_{y \text{ BM}}$ (stiffener)	<ul style="list-style-type: none"> Plate: Rectangular distribution with tension in HAZ and compression in between stiffeners Stiffener: Rectangular distribution with tension in welded tip and compression on free end 	22.87 mm for plate 13.06 mm for stiffener	$F_{y \text{ HAZ}} = 0.67 F_{y \text{ BM}}$
Paik et al. (2008)	MIG T Fillet Welds	$F_{y \text{ RTS}} = F_{y \text{ HAZ}}$	$\frac{F_{y \text{ RCS}}}{F_{y \text{ BM}}} = -0.161$ average for plate $\frac{F_{y \text{ RCS}}}{F_{y \text{ BM}}} = -0.137$ average for stiffener	Similar to Paik et al. (2005)	23.1mm (average)	$\frac{F_{y \text{ HAZ}}}{F_{y \text{ BM}}} = 0.777$ (average)
Benson et al. (2013)	No experiment conducted	$F_{y \text{ RTS}} = 0.95 F_{y \text{ HAZ}}$	In equilibrium with tensile residual stresses	<ul style="list-style-type: none"> Plate: Rectangular distribution with tension in HAZ and compression in free end 	25 mm	$F_{y \text{ HAZ}} = 0.67 F_{y \text{ BM}}$
Farajkhah and Liu (2016b)	Model was verified by tested data in (Masubuchi, 1980)	<ul style="list-style-type: none"> Plate $F_{y \text{ RTS}} = (0.72-0.77) F_{y \text{ BM}}$ Stiffener $F_{y \text{ RTS}} = (0.82-0.87) F_{y \text{ BM}}$ 	<ul style="list-style-type: none"> Plate $F_{y \text{ RCS}} = (-0.18 \text{ to } -0.36) F_{y \text{ BM}}$ Stiffener $F_{y \text{ RCS}} = (-0.024 \text{ to } -0.07) F_{y \text{ BM}}$ 	<ul style="list-style-type: none"> Plate: Rectangular distribution with tension in HAZ and compression in free ends Stiffener: Rectangular distribution with tension in welded tip and compression on free end 	18 to 28 mm from weld line for 5 and 6 mm thick plates 14 mm from weld line for 8 mm thick plate	$F_{y \text{ HAZ}} = 0.67 F_{y \text{ BM}}$

¹RTS= Residual Tensile Stresses

²RCS= Residual Compressive Stresses

Table 2.2: Magnitude and distribution of residual stresses in AA6061-T6 reported in literature

Reference	Type of weld	Welding Residual Stress		Residual Stress Distribution	HAZ	
		Tensile, RTS ¹	Compressive, RCS ²		HAZ extent (mm)	$F_{y \text{ HAZ}}$
Yi et al. (2015)	Double Pulse-MIG Fillet welds	Max of 175 MPa (25.4 ksi) in HAZ (5mm away from weld centerline)	Max of -60 MPa (-8.7 ksi) (20 mm away from weld centerline)	<ul style="list-style-type: none"> • Tensile in HAZ with the curve down. • Compressive stresses balance out tensile stresses. • Stresses were taken from the plate only. 	Not reported	Not reported
Yi et al. (2019)	Double Pulse-MIG Butt welds	Max of 190 MPa (27.5 ksi) in HAZ (5mm away from weld centerline)	Max of -60 MPa (-8.7 ksi) (35mm away from weld centerline)	<ul style="list-style-type: none"> • Tensile in HAZ with the curve down. • Compressive stresses balance out tensile stresses. • Stresses were taken from the plate only. 	Not reported	Not reported
Farajkhah et al. (2017)	MIG Butt Welds	<ul style="list-style-type: none"> • Max of 263 MPa (38.2 ksi) in HAZ (21mm away from weld centerline) • 9 mm thickness 	<ul style="list-style-type: none"> • Range of -30 to -39 MPa (-4.35 to -5.65 ksi) (these balance out the tensile residual stresses) • 9 mm thickness 	<ul style="list-style-type: none"> • The tensile residual stress zone had a width of 80 mm (40 mm from the centerline) • Increasing plate thickness, increased residual stresses (4-, 6-, and 9-mm thickness were tested) 	<ul style="list-style-type: none"> • 15mm from weld line for 4- and 6-mm thick plates • 21mm from weld line for 9 mm thick plate 	$F_{y \text{ HAZ}} = 0.60 F_{y \text{ BM}}$
Yi and Park (2022)	GMAW Fillet Welds	<ul style="list-style-type: none"> • 112.5 MPa (16.3 ksi) in HAZ (10 mm away from weld centerline) • 10 mm thickness 	<ul style="list-style-type: none"> • -12.2 MPa (-1.8 ksi) (80 mm away from weld centerline) • 100 mm thickness 	<ul style="list-style-type: none"> • Tensile in HAZ with curve down. • Compressive stresses balances out tensile stresses • Stresses were taken from plate only 	Not reported	$F_{y \text{ HAZ}} = 0.63 F_{y \text{ BM}}$
Zhao et al. (2021)	MIG Butt Welds	<ul style="list-style-type: none"> • 89.9 MPa (13 ksi) in HAZ (15mm away from weld centerline) • 10.5 mm thickness 	<ul style="list-style-type: none"> • -88.9 MPa (-12.9 ksi) (90 mm away from weld centerline) • 10.5 mm thickness 	<ul style="list-style-type: none"> • Tensile in HAZ with curve down. • Compressive stresses balances out tensile stresses 	11.4	Not reported

¹RTS= Residual Tensile Stresses

²RCS= Residual Compressive Stresses

2.3 VARIABILITY IN THE MECHANICAL PROPERTIES OF ALUMINUM ALLOYS

The literature review conducted as part of this work highlighted the presence of high variability in the reported mechanical properties of aluminum alloys. A main parameter that significantly impacts the mechanical properties is the chemical composition of the aluminum alloy. Tercelj et al. (2013) investigated the effect of the chemical composition on the mechanical properties of AA6082. The study concluded that a small increase in the alloying elements can have a major impact on the mechanical properties. For instance, a 33% increase in manganese leads to 5% increase in the elongation. However, copper has an opposite effect on the elongation. The same study also shows that the relationship between the mechanical property of interest (e.g., the yield stress) and the content of alloying elements is far more complex than just a linear proportionality with the content of a single alloying element. In addition to the chemical composition, material production parameters such as the extrusion ratio and ram speed affect the mechanical properties. Material elongation increased with the increase in the extrusion ratio and decrease in the ram speed. The yield stress, however, increased with increasing the ram speed (Tercelj et al., 2013).

Heat treatment is another factor that impacts the mechanical properties of aluminum alloys, specifically, the duration and temperature the alloy is subjected to during the precipitation hardening process play an important role (Siddiqui et al., 2000; Ozturk et al., 2010). Other studies in literature highlighted the impact of the specimen attributes and test procedure on the obtained mechanical properties. These include the coupon dimensions and thickness, rolling direction, and strain rate. Børvik et al. (2009) conducted tensile tests on specimens with four different thicknesses (i.e., 15, 20, 25, and 30 mm) made from A5083-H116 to investigate the effect of the thickness on the mechanical properties. The tests reported a yield stress of 278, 230, 152, and 224 MPa (40.3, 33.5, 22, and 32.5 ksi) for the 15, 20, 25, and 30 mm, respectively. This variation was attributed to the different manufacturing mechanisms that can be used to obtain the H116 temper with a particular thickness. Najib et al. (2015) tested the effect of rolling direction on the mechanical properties of AA5083. An increase in the ultimate strength as the angle increases from 0° to 90° was observed, while a decrease in the Young's Modulus was noticed.

The strain rate was also shown to affect the load-deformation behavior of aluminum coupons. Tucker et al. (2010) investigated the effect of the strain rate on the material behavior and

the associated failure mechanism of multiple aluminum alloys including AA6061-T6 through a group of tensile, compressive, and torsional tests. The study covered three strain rates: 0.001/s, 1/s, and 1000/s and reported similar values of ultimate tensile strength and elongation at the two lower rates, while an increase in the ultimate tensile strength and elongation (6.7% and 43%, respectively) occurred at the highest strain rate. Ambriz et al. (2013) also investigated the tensile behavior of AA6061-T6 under different strain rates. Quasi-static and dynamic strain rates, equal to 5.25×10^{-4} /s and 1500/s, were applied to tensile coupons. A 5.5% increase in the ultimate tensile strength and 78% increase in elongation were observed with the higher rates, however, a 40% drop in the yield strength was also seen.

As for AA5083-H116, Darras et al. (2013) investigated the load-deformation behavior of AA5083 under strain rates of 0.001/s, 0.01/s, and 0.1/s and concluded that at these strain rates, the ductility and yield strength of this aluminum alloy show very low sensitivity to the strain rate. Other studies in literature suggests that the AA5083-H116 may exhibit a negative strain rate sensitivity at a certain range of strain rates. Clausen et al. (2004) performed tensile tests over four different strain rates: 4×10^{-4} /s, 3.95/s, 122/s, and 1313/s. Normally, increasing the strain rate would lead to an increase in the flow stress; however, the results showed a negative strain rate sensitivity highlighted by a decrease in the flow stress with the increase in the strain rate, as the strain rate increases from 10^{-5} /s to 10/s. After that, a positive strain rate sensitivity was observed. In the case of negative strain rate sensitivity, redistribution of the stresses at the necking zone is prevented due to the softening resulting in fracture to occur in at lower strains. This range of strain rates that can be accompanied by negative strain rate sensitivity is critical since marine vessels can be subjected to strain rates that lie in the 10^{-3} /s region (Giannotti & Stambaugh, 1984).

Among the notable efforts targeted to quantify the variability associated with the mechanical properties of aluminum alloys, Skejić et al. (2021) compiled the mechanical properties of several aluminum alloys from 12,542 coupon tests reported in literature. For the AA6061-T6, the paper reported the yield strength to follow Lognormal distribution with a mean of 263 MPa (38.15 ksi) and a 7% coefficient of variation based on 27 samples. Moreover, a Lognormal distribution with a mean of 279 MPa (40.5 ksi) and a 6% coefficient of variation was reported for the ultimate tensile strength of the same alloy. Although the paper reported the mechanical properties of AA5083, it was not of the same temper as the plates utilized in this report (i.e., H116).

Accordingly, more testing and statistical analysis are still needed to establish the probabilistic descriptors of the mechanical properties of various aluminum alloys.

Studies in literature that reported the mechanical properties of the two alloys utilized in this report were collected as part of this literature survey. Table 2.3 and Table 2.4 present the findings associated with each alloy. The mean value of the yield strength of AA5083-H116 obtained from 10 different studies was 220 MPa (32 ksi) with a coefficient of variation of 8.65%, while the mean of the ultimate tensile strength is 325 MPa (47.2 ksi) with a coefficient of variation of 6.7%. The lower bound for the reported ultimate tensile strength of AA5083 is 300 MPa (43.5 ksi) while the upper bound is 353 MPa (51.2 ksi). For the AA6061-T6 alloy, the mean and coefficient of variation of the tensile yield strength based on 9 published studies is 272 MPa (39.5 ksi) and 7%, respectively. The mean value of the reported ultimate strength is 310 MPa (45 ksi) with a coefficient of variation of 6%. The lower bound of the reported ultimate tensile strength is 262 MPa (38 ksi) while the upper bound is reported as 335 MPa (48.6 ksi). Quantifying the uncertainty associated with these parameters is essential in establishing reliability-based design procedures that reflect the realistic behavior of welded aluminum panels. To maximize the safety of designed structures, design specifications, e.g., *Aluminum Design Manual* (AA 2020) and *Eurocode 9 Design of Aluminum Structures* (CEN 2007), utilize a low bound of the mechanical properties. This conservatism may result in an uneconomical design.

Based on this review, it seems that the variability in the mechanical properties of aluminum alloys stems from two main sources. The first is related to the chemical composition and production techniques while the second is related to the test methods and protocols. Regardless of the source, these uncertainties affect our ability to predict the true strength of the components under normal operational conditions and more research is needed to quantify and reduce these uncertainties. Given this high variability, to aid in understanding the behavior of the tested large-scale specimen, it was decided to conduct a parallel ancillary testing program aiming at quantifying the stress-strain behavior of the material utilized for fabricating the specimens.

Table 2.3: Mechanical properties of AA5083-H116.

Reference	Yield Tensile Strength, F_{ty} MPa (ksi)	Ultimate Tensile Strength, F_{tu} MPa (ksi)
Zha and Moan (2001)	235 (34.075)	349 (50.605)
Romhanji and Popović (2006)	215 (31.175)	305 (44.225)
Collette (2007)	214 (31.03)	300 (43.4)
Paik (2009)	239 (34.655)	353 (51.185)
Cueca et al. (2012)	215 (31.175)	305 (44.225)
Dutra et al. (2015)	220 (31.94)	328 (47.56)
Jesus et al. (2017)	220 (25.375)	300 (43.5)
KumarSingh et al. (2018)	228 (33.06)	317 (45.965)
Huang et al. (2019)	206 (29.87)	305 (44.225)
Ilman et al. (2020)	230 (33.35)	346 (50.126)

Table 2.4: Mechanical properties of AA6061-T6.

Reference	Yield Tensile Strength, F_{ty} MPa (ksi)	Ultimate Tensile Strength, F_{tu} MPa (ksi)
Collette (2007)	240 (34.8)	262 (38)
Lakshminarayanan et al. (2009)	300 (43.79)	335 (48.43)
Ashwani Kumar et al. (2014)	280 (40.6)	310 (44.95)
Khotiyan and Kumar (2014)	280 (40.6)	310 (44.95)
Arun and Ramachandran (2015)	240 (34.8)	295 (42.63)
He et al. (2016)	280 (40.02)	310 (44.95)
Pérez et al. (2016)	270 (39.3)	322 (46.69)
Ramaswamy et al. (2020)	275 (39.875)	318 (46.11)
Zhang et al. (2020b)	276 (40.02)	322 (46.69)

2.4 TENSILE STRENGTH PREDICTION OF WELDED ALUMINUM PANELS

2.4.1 Aluminum Design Methods

The latest form of the *Aluminum Design Manual* (AA 2020), published by the Aluminum Association, adopts the mechanical properties of the base metal reported in the ASTM of the designated aluminum alloy or in accordance with the guidelines put forth by the AWS D1.2 (2014) for welded aluminum alloys. The length of the HAZ, as defined in AA (2020), extends to 25 mm (1-in) from the centerline of the groove weld or the heel of the fillet weld. In the presence of transverse welds, where the entire cross section is heat affected, the strength of the cross section can be computed by multiplying the tensile ultimate strength of the weld-affected wrought material, F_{tuw} by the effective net area, A_e which corresponds in this case to the HAZ. In the presence of longitudinal welds, the strength of the cross section is computed as the sum of the strength of the unaffected material away from the HAZ and the heat affected material in the HAZ. The nominal tensile strength P_n , can be computed as (AA 2020)

$$P_n = ((F_{tu} * (A_e - A_{ewz}))/K_t) + (F_{tuwz} * A_{ewz}) \quad (1)$$

where F_{tu} is the ultimate tensile strength of unaffected zones, A_e is the effective net area, A_{ewz} is the area of the welded zone, K_t is the tension coefficient (taken as 1 for the aluminum alloys utilized on this report), and F_{tuwz} is the tensile ultimate strength of the weld-affected zone which can be computed using the weighted average approach as (AA 2020)

$$F_{tuwz} = ((F_{tuwBM} * A_{BM}) + (F_{tuwFM} * A_{FM}))/A_{wz} \quad (2)$$

$$A_{wz} = A_{BM} + A_{FM}$$

F_{tuwBM} is the tensile ultimate strength of weld-affected base metal given in Table A.4.3 of the *Aluminum Design Manual* (AA 2020), F_{tuwFM} is the tensile ultimate strength of the filler metal given in Table A.4.6 of AA (2020), A_{BM} is the area of the base metal in the weld affected zone, A_{FM} is the area of the filler metal, and A_{wz} is the area of the weld-affected zone that extends 25 mm (1-in) from the heel of the fillet weld. In this report, for the specimen with longitudinal and transverse welds, the entire cross section will be treated as weld-affected in the transverse direction and the specimen is expected to fail in that region.

The European specifications, *Eurocode 9 Design of Aluminum Structures* (CEN 2007), follows a different path for quantifying the design capacity of the HAZ adjacent to fillet welds. It applies a softening factor, $\rho_{u,haz}$, to the HAZ that depends on the alloy, temper, and the welding process (i.e., MIG or Tungsten Inert Gas (TIG)). Furthermore, the width of the HAZ, b_{haz} depends on the welding process and the material thickness. The MIG welding process can be applied to all thicknesses, however, the TIG is used with thickness up to 6 mm. TIG welding on higher thicknesses leads to a larger HAZ and would require a more severe softening factor. The design resistance of the HAZ adjacent to a fillet weld for the tensile forces perpendicular to the failure plane is given in Equation 3. This needs to be checked at the fusion boundary and at the toe of the weld.

$$\sigma_{haz,Ed} \leq \frac{f_{u,haz}}{\gamma_{Mw}} \quad (3)$$

where $\sigma_{haz,Ed}$ is the design normal stress perpendicular to the weld axis, $f_{u,haz}$ is the characteristic strength of the HAZ which relies on the reduction factor discussed before, and the γ_{Mw} is the partial factor for welded joints which 1.25. Similar models are provided for shear forces and combined shear and tensile forces.

Other specifications, such as the *ABS Rules for Building and Classing High-Speed Craft* (ABS 2023) rely on the allowable stress approach for aluminum structural design. The stresses are computed using finite element (FE) analysis and compared against the allowable stress. These allowable stresses are provided as a fraction of the proof stress of the HAZ, the type of structure under consideration, and the type of loading. Proof and ultimate strengths are provided for certain welded aluminum alloys; however, the gauge length is not specified, which makes it difficult to compare these allowable stresses to values reported in other design codes. Unfortunately, the extent of the HAZ is also not explicitly defined. On the other hand, certain weld bend tests and weld qualification procedures are required to ensure that the required ductility of the welds is met.

2.4.2 FE modelling for predicting the tensile strength of welded aluminum panels

Finite element analysis has been utilized in literature to predict the capacity of aluminum components. Dørum et al. (2010) analyzed the failure of welded aluminum connections using solid, shell, and cohesive-zone elements. The solid element model was used as the reference

solution for the other two models; however, its mesh sensitivity and need for a small mesh size to fully capture the strain concentrations increase the modeling effort and computational cost. The shell element model was also found to be mesh sensitive; additionally, strain concentrations occurred at lower load levels when compared to the model with solid elements due to the neglect of the out-of-plane normal stresses. The cohesive-zone model lumped the weakest zone of the HAZ between the solid elements with lengths equal to the surrounding mesh. The results were satisfactory in comparison to the base solid element model especially that this model is mesh insensitive. Unfortunately, no validation with experimental results was conducted.

Sensharma et al. (2011) studied the possibility of modeling the extent and location of the HAZ explicitly in the FE model. The HAZ in their study had its own mechanical properties. Three variants were modelled: all base metal with no HAZ, a single HAZ, and a combination of base metal and HAZ on an aluminum stiffened panel consisting of 3 bays and 4 stiffeners. The results came with all base metal models being unrealistic and all HAZ being too conservative. The analysis was conducted under tensile, compressive, and bending loading. The results from the analysis on the stiffened panel showed an ultimate compressive strength prediction close to the that resulting from the model proposed by Paik et al. (2005). Unfortunately, no comparison to tensile testing results was conducted. The width of the HAZ was assumed to be three times the thickness of the plate; however, this model used shell elements which did not allow modelling of welds. Furthermore, the residual stresses were not included in the analysis. However, the need for considering the HAZ in the FEM was clearly highlighted in their study.

Woelke et al. (2017) studied the effect of modelling undermatched welds, commonly found in ship construction, on the behavior of aluminum welded connections. The study advocates the need to account for undermatched weld properties in the design process since they are associated with a decrease in the strength of the HAZ which generally governs the strength of the connection. Furthermore, the presence of undermatched welds affects the plastic fracture behavior and crack initiation and propagation within the weld metal or the HAZ. In designing large-scale aluminum structures, shell elements with in-plane dimensions greater than the thickness are typically utilized. This may preclude the ability to account for through-thickness deformations that may affect the behavior especially in the presence of undermatched welds. To address this, an approach that includes a calibrated cohesive zone was presented in their study to predict the ductile failure of

aluminum structures with undermatched welds. The results were promising; however, this technique relies on the assumption that plasticity is only localized in the WM and HAZ and that the BM will still be in the elastic domain. Accordingly, it may not be applicable for welded joints with matched welds.

Nazemi and Ghrib (2019) studied the change in mechanical properties across the HAZ in welded aluminum connections. They identified multiple zones within the HAZ each with its own mechanical properties. This can be seen in Figure 2.3 for AA6061-T6. The x-marker in the figure represents the ultimate fracture point. These stress-strain curves were developed from the local strain measurements captured by the DIC technique. Using the DIC, material constitutive models were created using the virtual fields method (Germain, 1986). Furthermore, the results from the material constitutive models were validated using a fully coupled thermal-metallurgical-mechanical simulation. This simulation was divided into three stages. The first included the usage of the standard three-dimensional double ellipsoid heat source model proposed by Goldak et al. (1984) to model the welding on a mesh of 8-node solid elements. The second covered utilizing the metallurgical model proposed by Myhr and Grong (1991) for considering the phase transformations of heat affected aluminum and integrating it into the simulation. The last part is the simulation of a tensile test through the application of a fixed boundary condition at one end and an applied displacement on the opposite end. The finite element results were in good agreement with experimental ones; therefore, the approach was utilized to simulate the behavior of welded plate-column connection.

Farajkhah and Liu (2016a) studied how the fabrication method can affect the ultimate strength of aluminum hull girders. Their study included friction stir welding (FSW), MIG butt welding, and MIG fillet welds. One of the aims of their study was to simulate the three welding procedures and study the welding induced residual stresses, HAZ, and distortions to be used later in quantifying the strength of aluminum hull girders. The simulation of MIG welding was divided into multiple stages. Thermal loads were applied by adopting the birth/death feature in ANSYS (ANSYS, 2015) that mimics the accumulation of the molten metal droplets on the welded specimen. The time-dependent temperature distribution of the welded material was obtained through nonlinear transient thermal analysis. This time dependent temperature distribution was used to represent the increment in the position of the passing weld torch by being added as load

steps. After all the welding sequences were finished, the specimen cooling to room temperatures was also simulated resulting in obtaining the welding induced residual stresses and distortions. To allow for possible separation and/or sliding between the stiffener and plate before the deposition of welding, spring elements were defined in the interface region. Temperature and residual stresses profiles were validated against experimental test results conducted by Masubuchi (1980). The paper reported that the width of the HAZ around the weld line for MIG butt and MIG fillet welds was 30 mm (1.18-in) and 40 mm (1.57-in), respectively. The paper showed that this approach of FEM can simulate the MIG welding process. However, this modeling approach is complex and may not be suitable for large-scale structures.

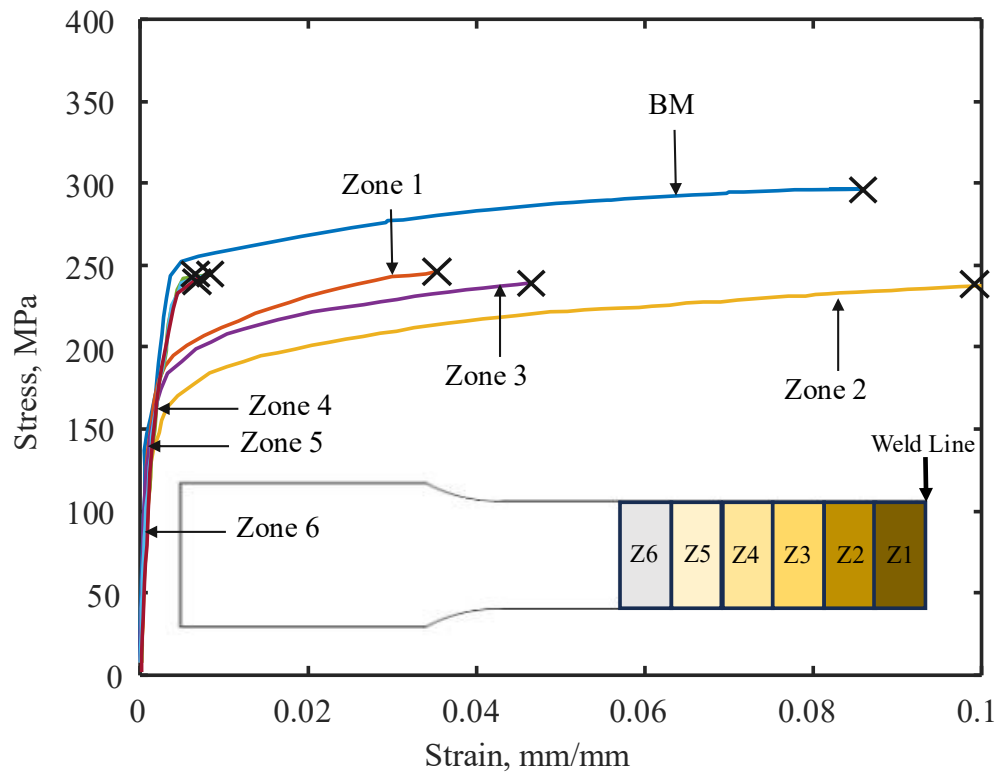


Figure 2.3: Stress-Strain curves for the HAZ of AA6061-T6 (adapted from Nazemi and Ghrib (2019)).

Collette (2022) investigated, experimentally and numerically, the strength of plates with transverse, non-load carrying fillet welds. The finite element model utilized different mechanical properties across the HAZ and included the fillet weld and definition of the residual stresses. Heating was applied to the model then specimen cooling was considered until it reached room temperature. This caused residual stresses to build up at the HAZ and BM within the model. The

mechanical properties across the HAZ were correlated to hardness test data and incorporated into the model through parallel sectioning of the material. The HAZ was divided into four zones with each section given the corresponding mechanical properties. Eighteen large scale specimens with transversely welded stiffeners were experimentally tested to cover two fillet weld sizes (i.e., 5 mm and 8 mm) and continuous versus intermittent fillet welds. The author recommended the use of more regions for the sectioned HAZ to fully capture the change in mechanical properties across the HAZ. It was also noted that correlation between the mechanical properties and hardness test data may be subjected to high variability. Nevertheless, the study showed that localized failures will happen in the HAZ and start at the toe of the weld when using non-load carrying fillet welded connections. In addition, the study highlighted the need for further investigations into the tensile capacity of welded aluminum components since they have a significant influence on the overall behavior of the structure.

Based on this literature survey, it is apparent that several knowledge gaps need to be addressed for the proper quantification of the tensile behavior of welded aluminum components. One of the main gaps is the lack of large-scale experimental data that covers the tensile behavior of aluminum components with different welding configurations. The presence of such experimental data would assist in the proper understanding of the behavior of ship hulls and validating the design approaches. A thorough experimental testing program that quantifies the impact of welding parameters on the behavior of large-scale welded aluminum would also assist in identifying the key factors associated with the reduction of strength/ductility due to welding. Furthermore, additional numerical analysis is necessary to assess the best practices for proper modelling of the welds, HAZ, and residual stresses especially when incorporated in large complex structures. Comprehensive assessment of the variability in the mechanical properties of aluminum alloys coupled with detailed reliability analysis would reflect on optimized design codes that provide safe yet economic designs. This report addresses some of these gaps by presenting the results of a comprehensive experimental program conducted to quantify the tensile behavior of unstiffened and stiffened large-scale aluminum specimens. The stiffened specimens include transversely stiffened components, longitudinally stiffened components, and the combination of both stiffener types in one specimen. In addition, it discusses a detailed finite element approach capable of capturing the actual behavior of these specimens under tensile loading.

3 EXPERIMENTAL TESTING PROGRAM

Experimental testing was conducted to understand the impact of welded stiffeners on the tensile strength of aluminum panels. The investigation included experimental analysis on large-scale specimens to quantify the effect of stiffeners and investigate the efficacy of different modeling strategies. This testing program included 12 specimens covering flat plates, longitudinally stiffened plates, transversally stiffened plates, and plates with both stiffener types. To properly characterize the material behavior and aid in numerical modeling, ancillary testing was conducted on tensile coupons extracted from the base metal and HAZ. The large-scale specimens and fabricated plates utilized for extracting the tensile coupons were fabricated by AUSTAL USA. The large-scale testing was conducted at the Bert Cooper Engineering Laboratory while the ancillary testing was performed in Endeavor Lab, both located in the Stillwater campus of Oklahoma State University. The following subsections present the details of both testing programs.

3.1 ANCILLARY TESTING

As indicated above, the analysis herein covers two types of aluminum alloys commonly used in ship construction, the AA5083-H116 and AA6061-T6511. Each of the tempers of the used aluminum alloys represent a unique process that yields certain mechanical characteristics. For example, the H in the H116 temper represent the work hardened temper type in which strength is elevated through work hardening. Heat treatment thereafter is optional. Specifically, the H116 temper is applied to 5xxx series alloys with a magnesium content higher than 4% and certain corrosion resistance and mechanical properties are required. On the other hand, the T in the T6 temper represent the heat-treated temper type where heat treatment is used to provide strength for the alloy and may or may not be followed by strain hardening. Specifically, the T6511 temper is heat treated and then artificially aged until the precipitation hardening of the alloy has evolved; next, the extrusion is given a permanent set and straightened to meet required construction tolerances. Coupon tests were needed to properly understand the behavior of the large-scale samples and obtain the mechanical properties to be utilized on the numerical analysis. Furthermore, characterizing the change in the mechanical properties across the HAZ for both aluminum alloys would aid in identifying the variables that govern the behavior of welded stiffened panels. To establish these goals, samples from the base metal plates and welded plates that are fabricated using the same electrode and welding technique utilized for the fabrication of

the large-scale specimens were requested from the fabricator. Figure 3.1 shows the details of the welded specimen requested from the fabricator. Tensile coupon specimens were extracted later from this specimen and used to characterize the behavior of the HAZ and BM.

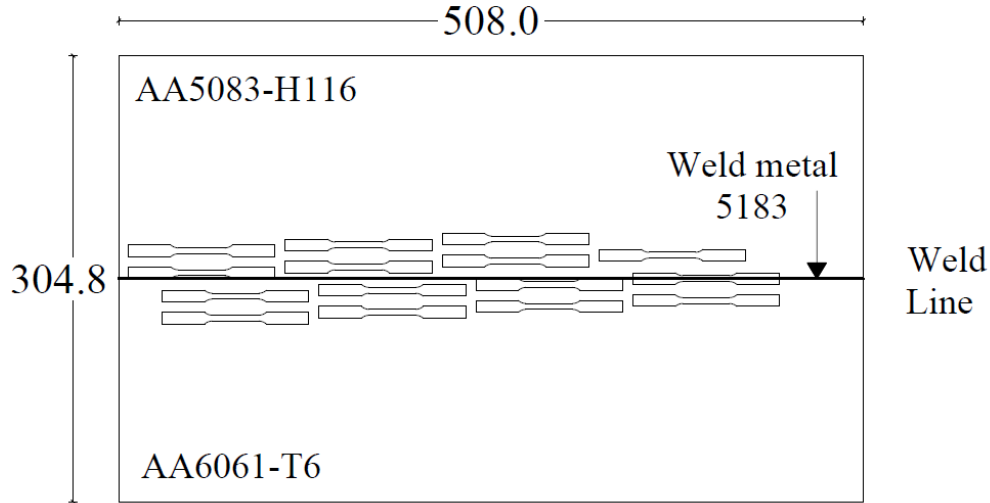


Figure 3.1: Dimensions of welded specimen for coupon testing in millimeters.

The groove welded specimen shown in Figure 3.1, is composed of AA5083-H116 and AA6061-T6 flat plates that were welded using 5183 filler metal. GMAW welding, with 1.2 mm (3/64-in) diameter ER5183 filler metal, was utilized for constructing all specimens in this test program. The welding was completed under constant voltage (CV) and direct current electrode positive (DCEP) with an amperage range of 185 and voltage of 24.5. The weld travel speed was set at 457 mm/minute (18 inch/minute) and the wire feed speed was 11.43 meters/minute (450 inch/minute). Each plate has dimensions of 508×152×12.5 mm (20×6×0.5-in). A single specimen was created from this welding process. Although the large-scale aluminum specimens, as will be discussed later, utilized plates with a thickness of 8 mm (5/16-in), in lieu of the 12.5 mm (0.5-in) thickness of these plates, it was still believed that this specimen can provide baseline information on the mechanical properties of the HAZ and BM. Tensile coupons with dimensions following ASTM B557 (2023) were extracted from this specimen using a water jet cutting. Figure 3.2 shows the detailed dimensions of these coupons. As shown in Figure 3.1, The coupons were staggered to provide ample space to prevent specimen damage and to allow extracting coupons at different locations within the HAZ. The coupons were extracted at 4, 8, 12, 16, 19, 23, and 27 mm from the center line of the weld for each aluminum alloy. Moreover, a single coupon was cut at the centerline of the weld metal to represent the mechanical properties of the 5183 weld metal. This

would enable evaluating the mechanical properties across the HAZ for the AA5083-H116, AA6061-T6511 and for the 5183 filler metal.

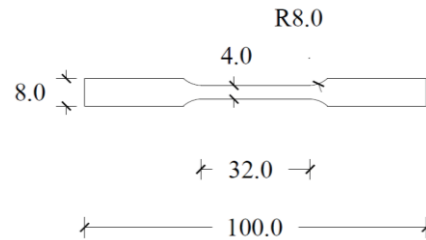


Figure 3.2: Dimensions of coupons that are to be cut using a waterjet in millimeters.

3.2 LARGE SCALE EXPERIMENTAL SETUP

3.2.1 Original Test Setup

The layout of the large-scale aluminum specimens was heavily influenced by the configuration and limitations of the test equipment. Initially, it was intended to utilize a 1,500 KN Instron Universal Testing Machine, shown in Figure 3.3 and available in Bert Cooper lab, for the large-scale specimens. The specimen was designed with an ultimate strength that falls within the capacity of the testing frame following the dimensions of the grip zone of the machine. Figure 3.4 shows the different components of the original test setup. Connection brackets or stiffeners were added between the end plate and test plate to prevent premature failure away from the gauge length.



Figure 3.3: The 1,500 KN Universal Testing Machine.

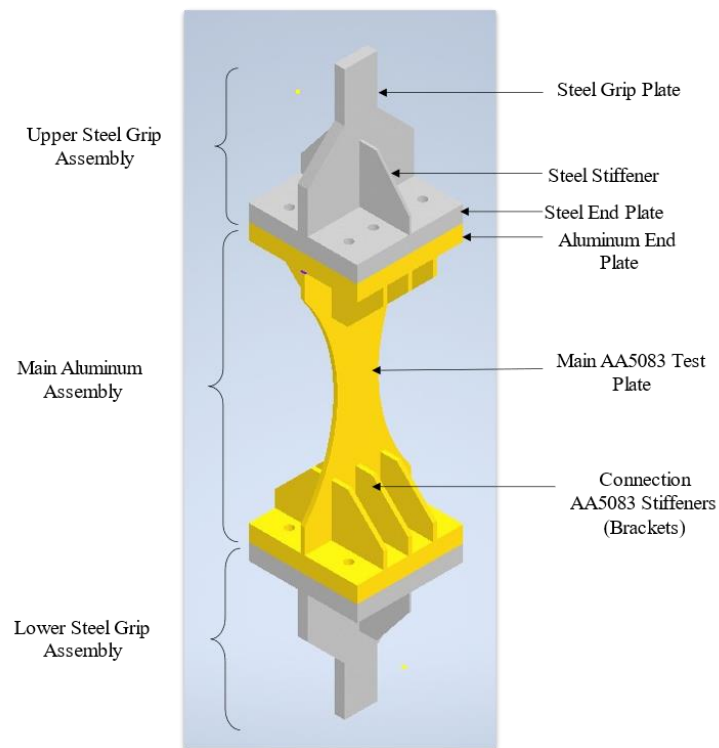


Figure 3.4: 3D render of the original test setup showing various specimen components.

The setup was designed such that the entire assembly would be inserted into the hydraulic grips of the machine with the steel grip assembly connected to the aluminum specimen using steel bolts and square washers on the aluminum side. Figure 3.5 shows the assembly inside the grips of the universal testing machine.



Figure 3.5: Original test setup with assembly in place.

3.2.1.1 Upper and Lower Steel Grip Assemblies

The upper and lower grip assemblies are mainly composed of a grip plate to be inserted into the hydraulic grip slots of the test machine and an end plate that is connected to the aluminum test specimen. Figure 3.6 shows a 3D view of the grip assembly, while Figure 3.7 shows the detailed dimensions of the assembly.

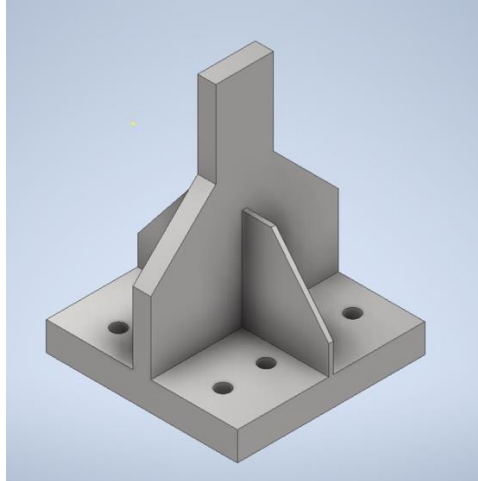


Figure 3.6: 3D render for the Steel Grip Assembly.

The material used for the steel grip assemblies is ASTM A572 Gr. 50 (ASTM A572, 2021). This steel has an ultimate and yield strengths of 449 MPa (65 ksi) and 345 MPa (50 ksi), respectively. This steel grip plate was checked against tensile yield. The steel end plate was designed to resist the bending stresses that would arise during the test using the models in *ANSI/AISC 360* (2016) and Swanson (2003). An 8 mm steel stiffener was added to reduce the stresses on the steel end plate and increase its stiffness. The steel grip plate and the steel end plate were welded using complete joint penetration groove weld based on Table 3.1 of AWS D1.1 (AWS, 2020) with an E70 electrode.

Unfortunately, this setup was eventually not utilized due to testing software malfunctions that occurred while testing the first specimen. Such malfunctions were feared to compromise the integrity experimental results. Therefore, an updated test setup was designed and constructed to complete the experimental testing and ensure the integrity of the results. The new setup utilized the same specimen design with changes applied only to the grip assemblies as will be discussed below.

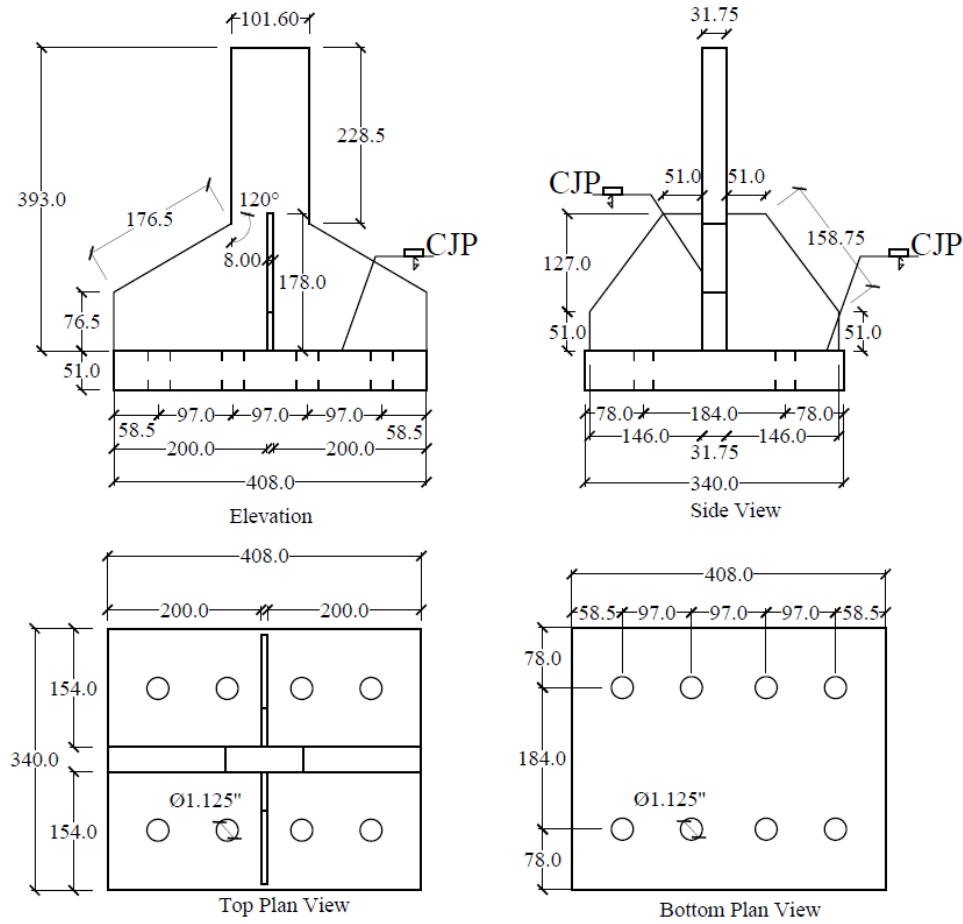


Figure 3.7: Detailed dimensions of the Steel Grip Assembly in millimeters.

3.2.2 Updated Test Setup

The updated test setup was designed to accommodate the layout of the aluminum specimen and the steel grip plates of the original setup since the shift to the new setup occurred after specimen fabrication. Figure 3.8 shows the layout of the updated test setup. The test system is comprised of two 2,570 KN (300 kips) actuators, two load cells, an upper loading beam, and two pin connected grip assemblies. With this setup, the actuators move the loading beam upward and apply tension to the specimen using the bolted connection between the aluminum and steel end plates. As seen in Figure 3.8, the lower steel grip is connected to the strong floor directly. A lateral support system was utilized to prevent the out-of-plane displacement of the loading beam. Figure 3.9 shows a 3D render for the aluminum specimen with the modified grip assemblies, while Figure 3.10 shows the overall dimensions of the test setup. Furthermore, the details of the modified grip assembly used for the upper and lower bolted connections are shown in Figure 3.11.

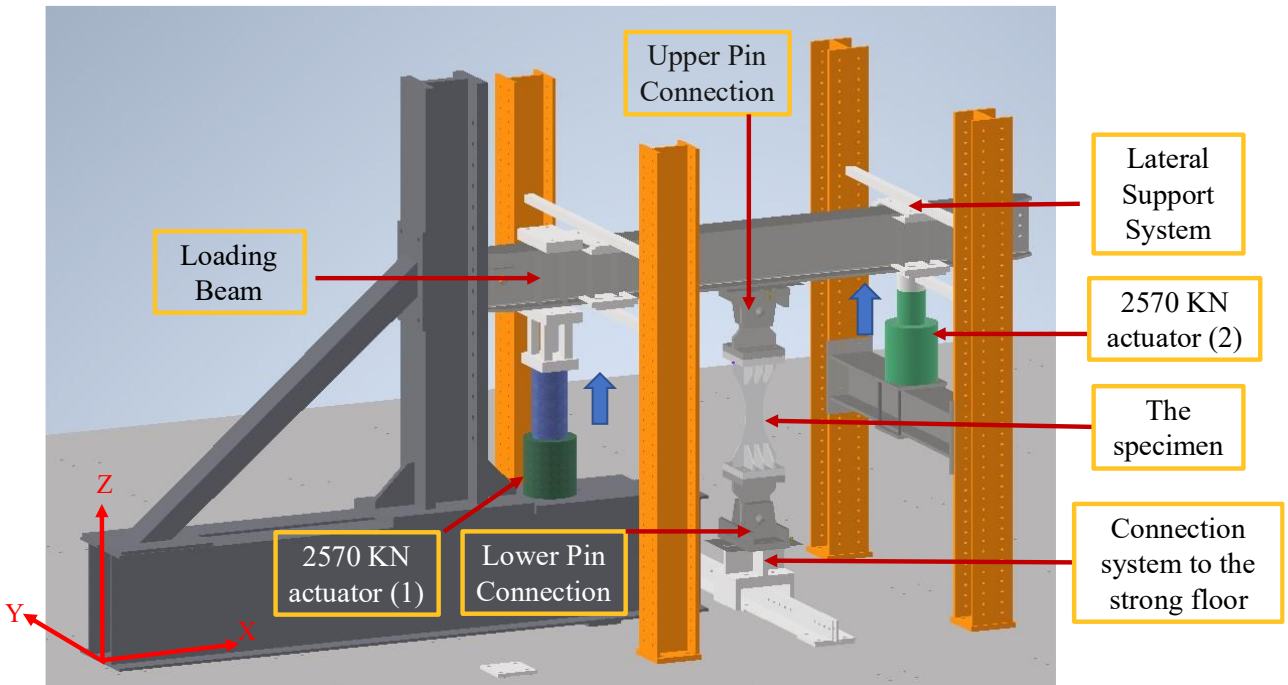


Figure 3.8: General layout of the updated test setup.

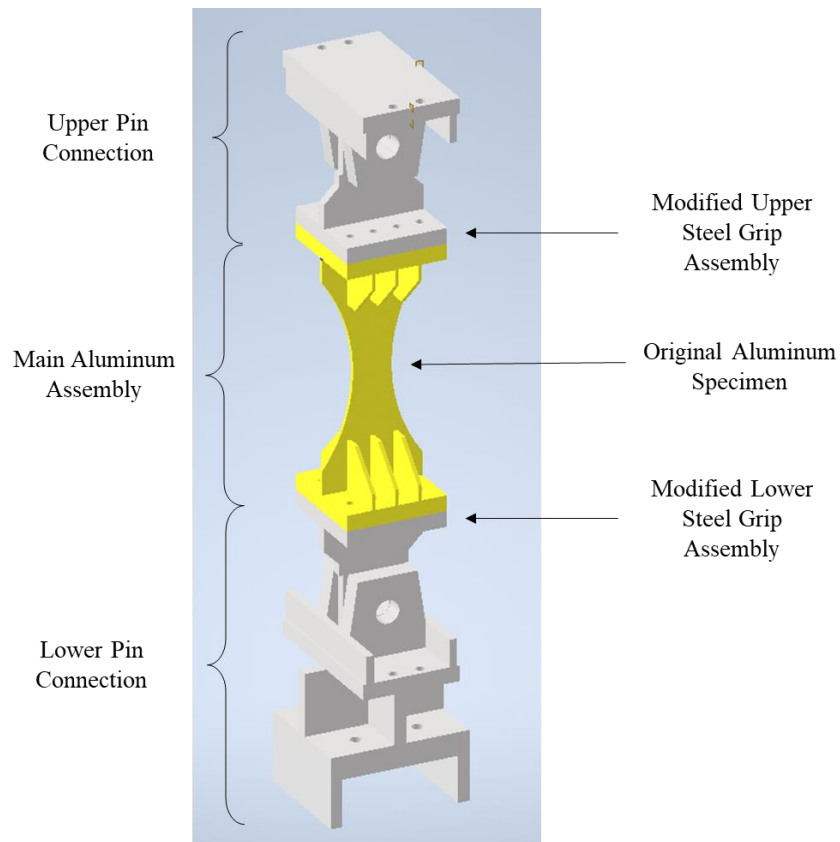


Figure 3.9: 3D render of the updated test setup showing various specimen components.

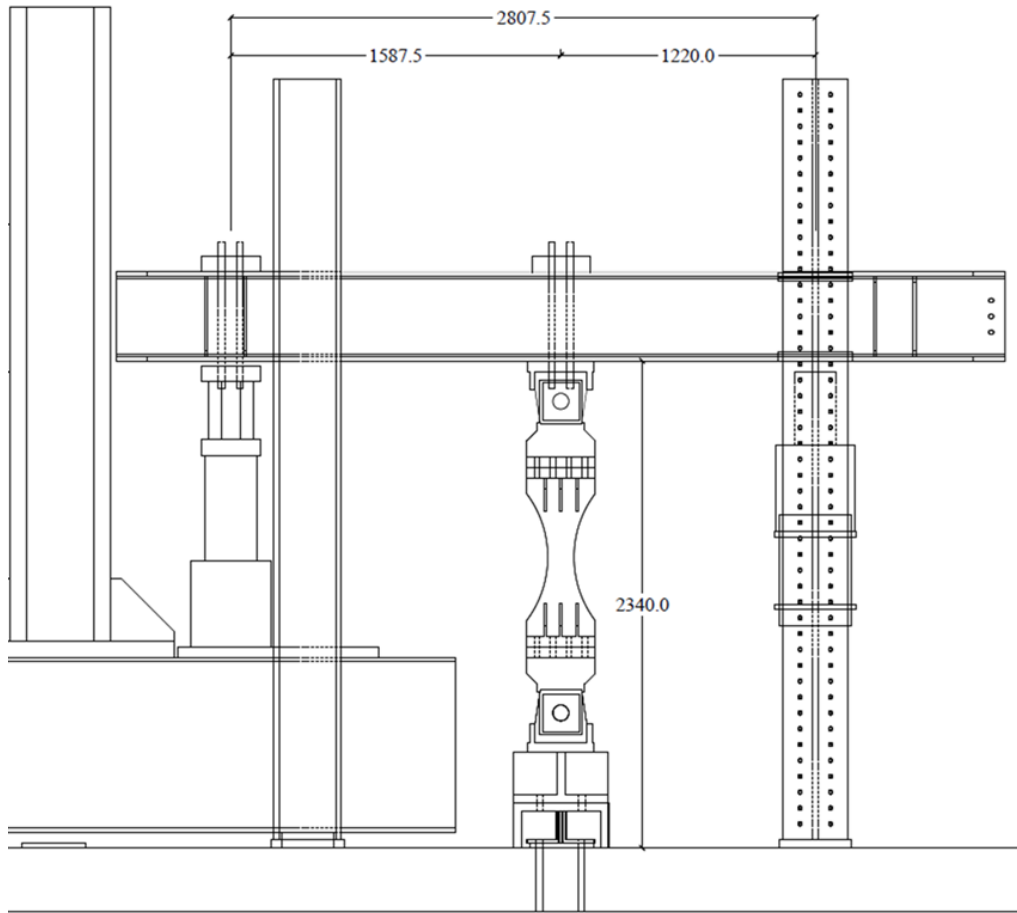


Figure 3.10: Overall dimensions of the updated test setup in millimeters.

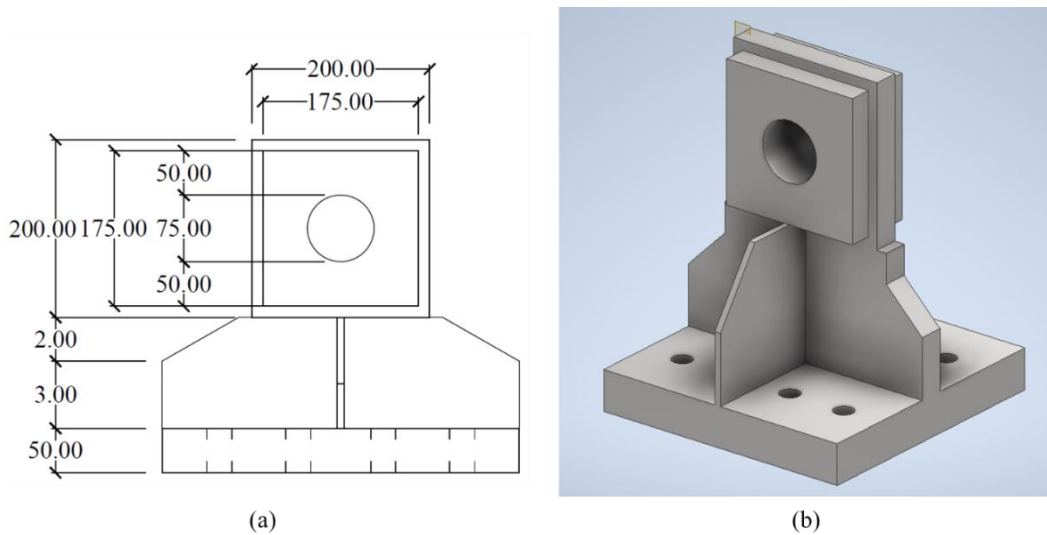


Figure 3.11: Detailed layout of the modified steel grip assemblies (a) dimensions of the modified upper and lower steel grip plates in millimeters, and (b) 3D render of the modified upper steel grip plate.

The upper loading beam is W16×89, made of ASTM A572 Gr. 50 (ASTM A572, 2021) with a span of 4270 mm (14 ft). This beam was checked against lateral torsional buckling and yielding according to *ANSI/AISC 360* (2016). Figure 3.12 shows the loading beam. The loading beam is supported on Load Columns 1 and 2 to accommodate the height of the aluminum specimen and the layout of existing steel frame. Figures 3.13 and 3.14 show, respectively, the details of both load columns. Note that both actuators were equipped with a linear variable displacement transducer (LVDT) to measure actuator displacement. The test specimen was connected to the strong floor, as shown in Figure 3.15, using four 38 mm diameter threaded rods that provide a total capacity of 1,250 KN.

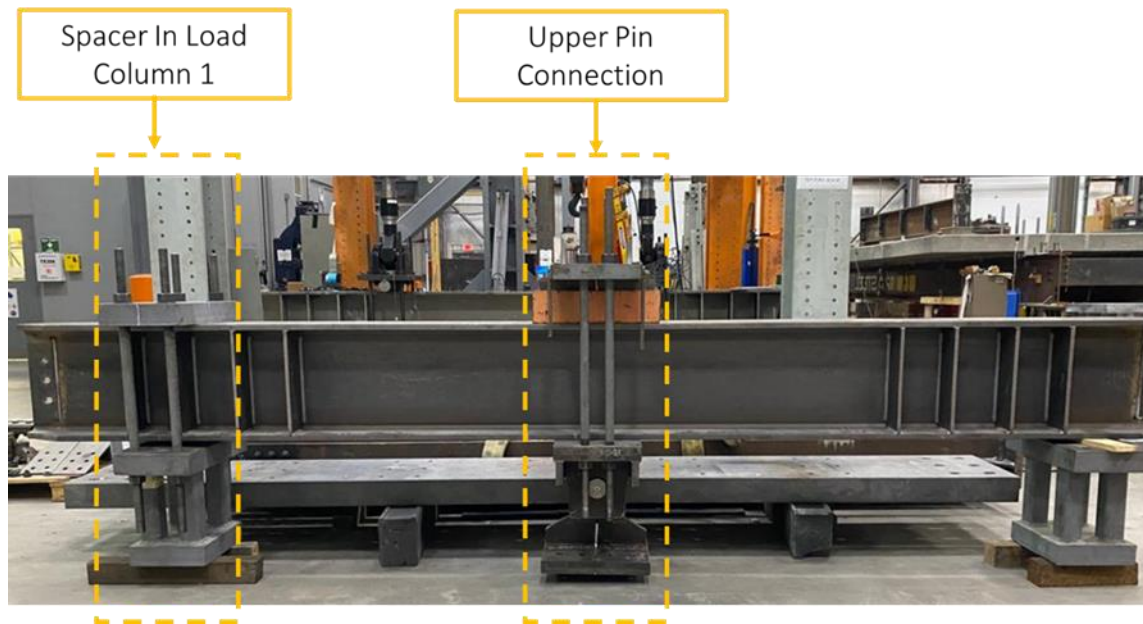


Figure 3.12: Loading Beam (W16×89) with upper pin connection and the spacer.

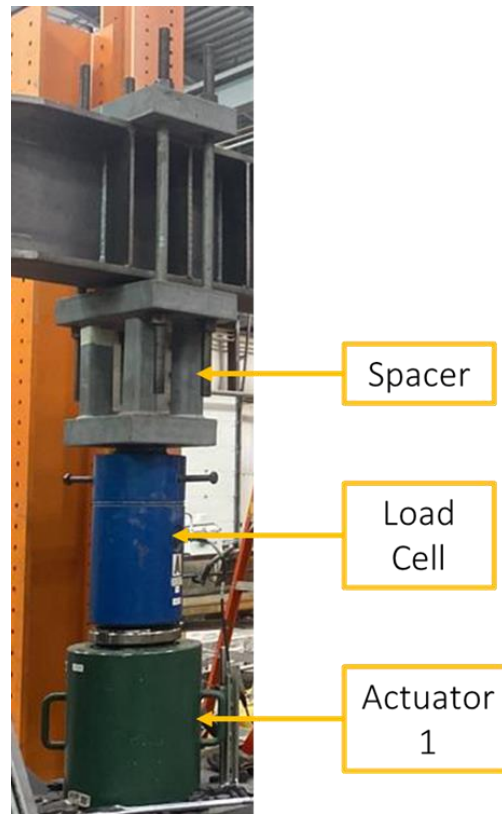


Figure 3.13: Various components of Load Column 1.

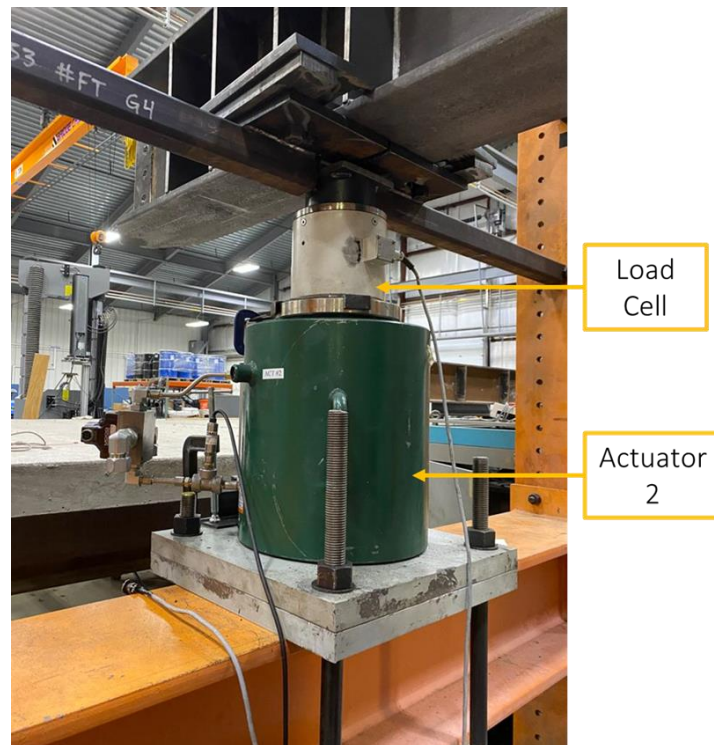


Figure 3.14: Various components of Load Column 2.



Figure 3.15: Connection to the strong floor.

The last component of the updated test setup is a lateral support system that prevents the out-of-plane displacement of the beam while allowing it to move vertically in the plane of the main test plate. The lateral support system is composed of steel tubular sections HSS 2.5×2.5×1/4 with an approximate length of 2,300 mm (90-in). Each of the tubular sections is allowed to move in the plane using roller bearing on both ends. Figure 3.16 shows a view of the lateral load system, while Figure 3.17 shows the roller bearing connection at each end of the tubular sections. As shown in Figure 3.16, the lateral support system is connected to the upper and lower flanges of the loading beam at each load column using high strength bolts. These bolts are installed in long slotted holes to allow for fine adjustments of the lateral support system location to accommodate the as-built characteristics of the loading setup. Figure 3.18 shows a view of the assembled test setup. After assembling the test frame, and without the specimen installed, the loading beam was actuated upward several times using the hydraulic load testing system to ensure that there is no drag introduced by the lateral support system.



Figure 3.16: View of the lateral support system attached to the loading beam.



Figure 3.17: Closeup view on the roller bearing that accommodates the in-plane movement.



Figure 3.18: The updated test setup.

3.2.3 Hydraulic System and Test Control

The Bert Cooper Laboratory is equipped with a 90-GPM MTS SilentFlo hydraulic power unit with a 3,000-psi operating pressure. An MTS FlexTest 60 Controller is utilized to control the two actuators simultaneously during the test. The loading actuators are Simplex hydraulic cylinders retrofitted with 760 series Moog servo valves to allow for fine test control. Two RDP ACT6000C-1613 LVDTs with ± 150 mm (± 6 -in) stroke are used to measure/control actuator displacement. Load Column 1 is equipped with a REVERE USP2F 1,140 KN (250 kips) load cell, while Load Column 2 utilizes a HBM C6A/5MN 5100 KN (1,125 kips) load cell. This system allows for conducting the test under load control or displacement control. Figure 3.19 and Figure 3.20 show both load columns used in this setup.

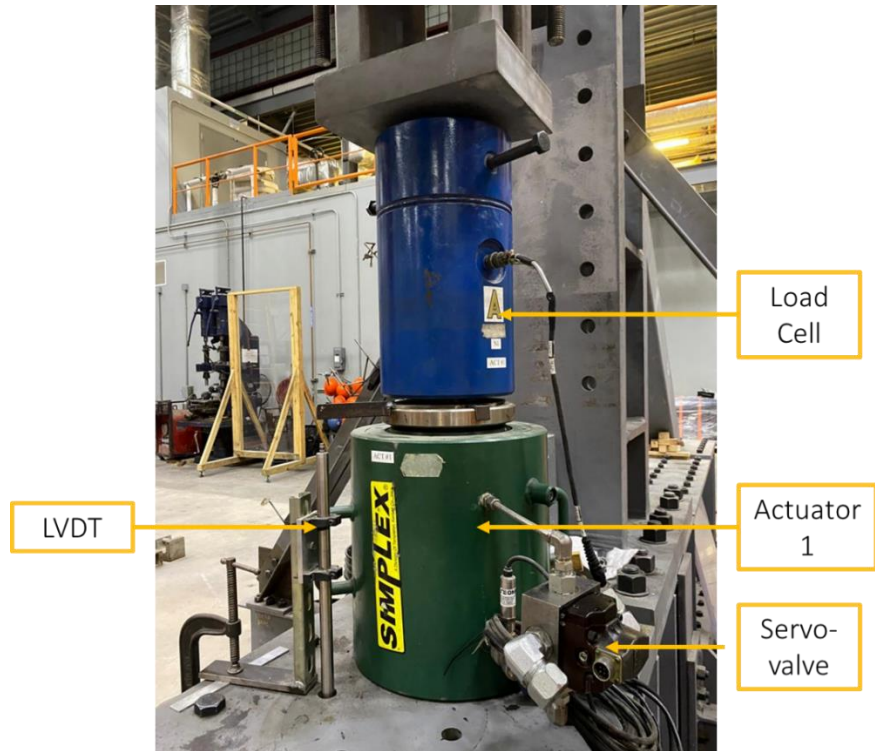


Figure 3.19: Components of the hydraulic system in Load Column 1.

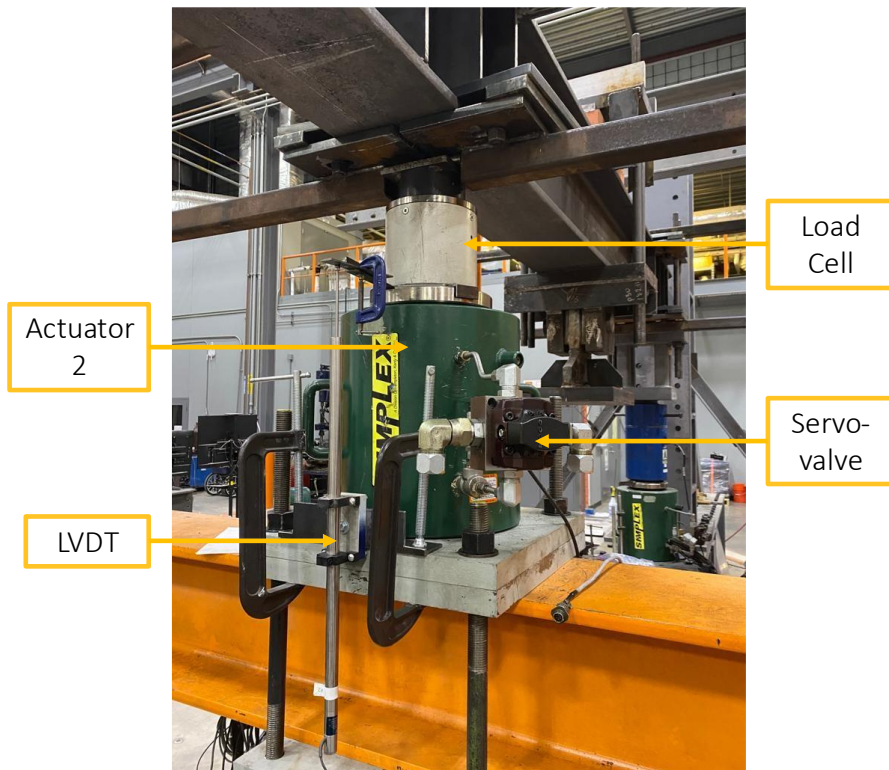


Figure 3.20: Components of the hydraulic system in Load Column 2.

3.2.4 Test Matrix for the Large-Scale Testing Program

The test matrix for the large-scale testing program focused on evaluating the effect of welded stiffeners on the load-deformation behavior of welded aluminum components. Accordingly, the test matrix included flat plates, load-bearing welded stiffeners (i.e., longitudinal stiffeners), non-load-bearing welded stiffeners (i.e., transverse stiffeners), and a combination of both types. In total, twelve specimens were included in the matrix with three specimens of each type to evaluate the variability in the behavior. Table 3.1 shows the adopted test matrix for the large-scale testing program. Other testing variables of interest include the weld technique (i.e., GMAW vs GTAW), weld type (i.e., continuous vs intermittent), and rolling direction. However, given the budgetary limitations, it was decided to focus only on the variables included in Table 3.1.

Table 3.1: Test matrix for the large-scale testing program

Specimen Designation	Number of Specimens	Specimen Type	Fillet Weld Type	Specimen ID
F	3	Flat Plate	--	F1
				F2
				F3
T	3	Transverse Stiffener	Non-Load Carrying	T1
				T2
				T3
L	3	Longitudinal Stiffener	Load Carrying	L1
				L2
				L3
LT	3	Longitudinal & Transverse Stiffener	Non-Load & Load Carrying	LT1
				LT2
				LT3

3.3 ALUMINUM SPECIMEN DESIGN

As indicated above, the large-scale test specimens are composed of an AA5083-H116 main plate with AA6061-T6511 for stiffening plates. Based on discussion with the project review committee, it was decided to limit the thickness of the test specimens to a maximum of 10 mm (13/32-in). The

large-scale test specimens are designed in accordance with the limitations of the original load frame. Accordingly, the height of the test specimen was kept lower than 1,830 mm (72-in) with a maximum load of 1,500 kN (330 kips). One of the main challenges was connecting the aluminum specimen to the test frame. Given the small thickness of the test specimen, it was not possible to directly connect the test plates to the hydraulic grips of the test frame, especially for specimens with longitudinal stiffeners. This led the team to utilize the steel grip assemblies discussed above in Section 3.2.1.1 and required using relatively thick aluminum end plates for the specimen as shown in Figure 3.21. This setup provides flexibility for the width of the specimen and allows for using longitudinal load-bearing stiffeners. Figure 3.22 shows a general layout of the flat plate test specimen.

Another challenge associated with the specimen design was the high variability in the mechanical properties discussed in Section 2.3. As shown in Tables 2.3 and 2.4, the ultimate strength of AA5083-H116 reported in literature ranges from 300 to 353 MPa (43.5 to 51.2 ksi) while for AA6061-T6 it ranges from 262 to 335 MPa (38 to 48.6 ksi). To prevent the premature failure of the test specimen at the end regions, it was decided to utilize a lower bound estimate of the reported mechanical properties for designing the upper and lower connection regions of the test specimen. Additionally, to ensure that the ultimate capacity of the specimen remains below the test machine capacity (i.e., for the original test setup), an upper bound estimate of the mechanical properties was adopted for the design of the main test plate and longitudinal stiffener. The mechanical properties utilized for the specimen design are shown in Tables 3.2 and 3.3 for both aluminum alloys.

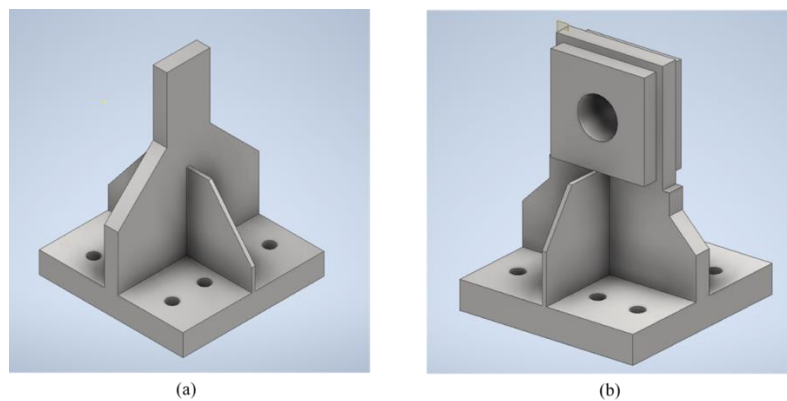


Figure 3.21: Comparison between the steel grip assemblies: (a) original test setup and (b) updated test setup.

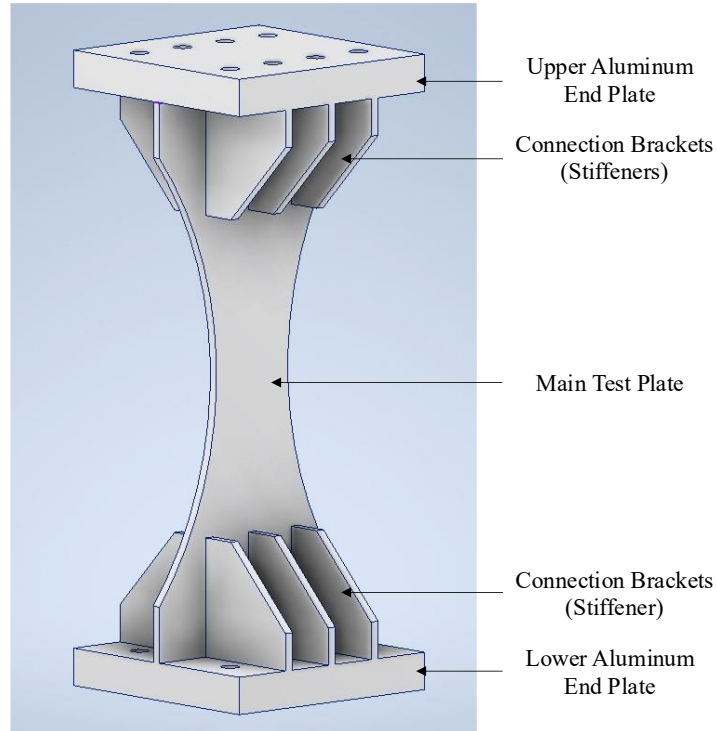


Figure 3.22: General layout of the Flat Plate Specimen.

Table 3.2: Mechanical properties of AA5083-H116 utilized in specimen design.

Bound	Ultimate Tensile Strength, F_{tu} MPa (ksi)	Yield Strength, F_{ty} MPa (ksi)	Reference
Lower	300 (43.4)	214 (31.03)	Collette (2007)
Upper	353 (51.185)	239 (34.655)	Paik (2009)

Table 3.3: Mechanical properties of AA6061-T6 utilized in specimen design.

Bound	Ultimate Tensile Strength, F_{tu} MPa (ksi)	Yield Strength, F_{ty} MPa (ksi)	Reference
Lower	262 (38)	240 (34.8)	Collette (2007)
Upper	335 (48.43)	300 (43.79)	Lakshminarayanan et al. (2009)

3.3.1 Flat Plate Specimens

The flat plate specimen is designated as the control specimen in the large-scale experimental program. As shown in Figure 3.22, the specimen is composed of the main test plate, upper and lower aluminum end plates, and stiffening brackets. The plate is constructed using AA5083-H116 with the dimensions shown in Figure 3.23. As shown, with this layout, the gauge length is chosen as 205 mm (8-in). The plate thickness was chosen to be 8 mm (5/16-in) based on discussion with the fabricator and the project review committee. The main test plate is designed considering an ultimate strength of 353 MPa (51.2 ksi) resulting in an estimated ultimate fracture capacity of 538 KN (121 kips). Single bevel complete groove weld is utilized to connect it to the aluminum end plates. This test plate layout is used for all specimen types.

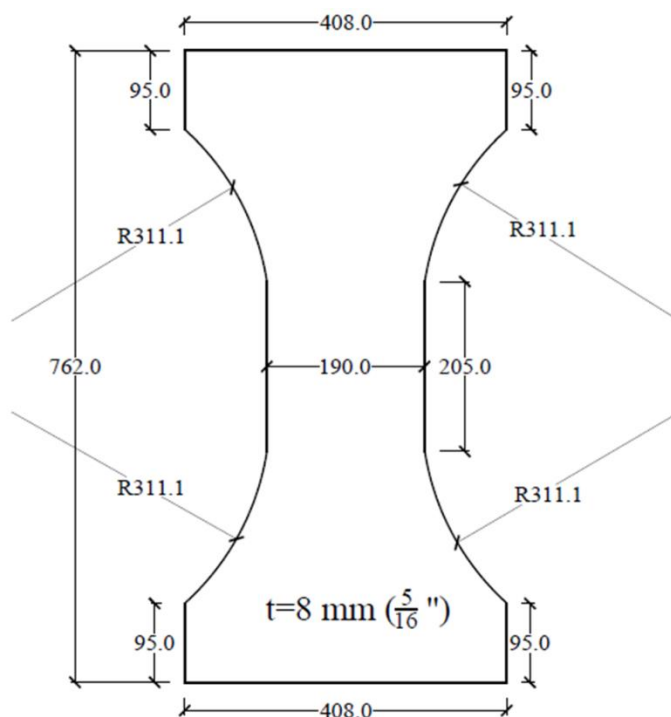


Figure 3.23: Dimensions of the main test plate in millimeters.

The aluminum end plate is constructed from AA5083-H116. The main design consideration was bending stresses considering the effect of prying action. The required plate thickness to eliminate the effect of prying action, based on Equation (9-17a) of *ANSI/AISC 360* (2016), is 47.2 mm (1.86-in). It was conservatively taken as 51 mm (2-in). Note that with the presence of stiffening brackets, the thickness of the end plate can be further reduced; however, it was decided to keep it as 51 mm

(2-in) to ensure rigidity at this critical location. The dimensions of the end plate are shown in Figure 3.24.

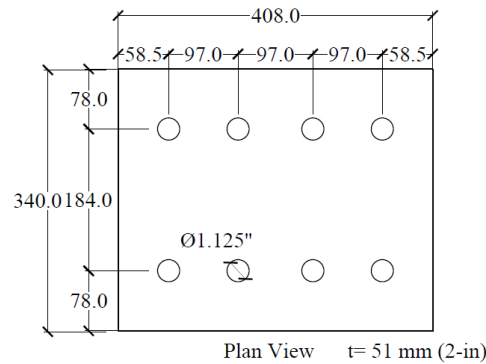


Figure 3.24: Dimensions of upper and lower aluminum end plate in millimeters.

To strengthen the connection between the main test plate and the end plate, and to reduce the possibility of pull-out failure of the main plate, six connection brackets (top & bottom), made of AA5083-H116, were added as shown in Figure 3.22. The stiffeners increased the welded area to ensure that failure occurs within the designated gauge length area. The stiffeners are to be welded using a single bevel complete penetration groove weld. The dimensions of the stiffeners are shown in Figure 3.25 and the dimensions of the flat plate specimen are shown in Figure 3.26.

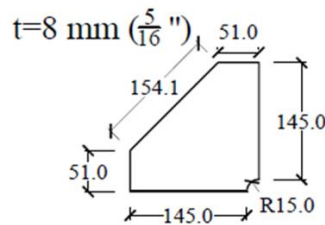


Figure 3.25: Dimensions of the connection stiffeners in millimeters.

An initial flat plate specimen was requested from the fabricator prior to fabricating all specimens to ensure the feasibility of the test setup and the failure occurrence at the desired location.

3.3.2 Transverse Stiffener Specimens

The second set of specimens have transverse stiffeners made of AA6061-T6511 welded to the main AA5083 test plate using four continuous non-load bearing fillet welds with size of 4 mm (3/16-in). The weld filler metal is 5183. The detailed dimensions of the specimen and a 3D render for the specimen are shown in Figure 3.27.

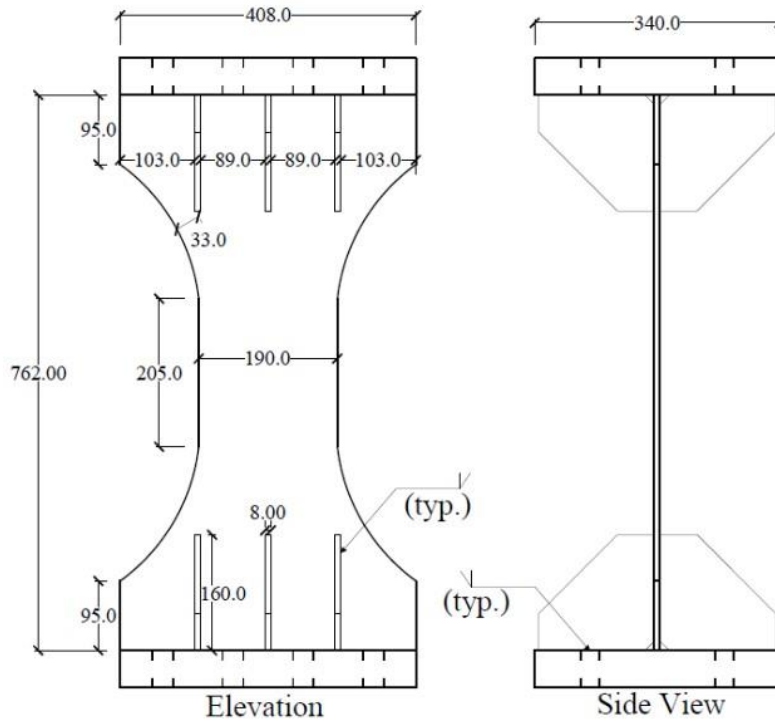


Figure 3.26: Dimensions of the flat plate specimen (in millimeters).

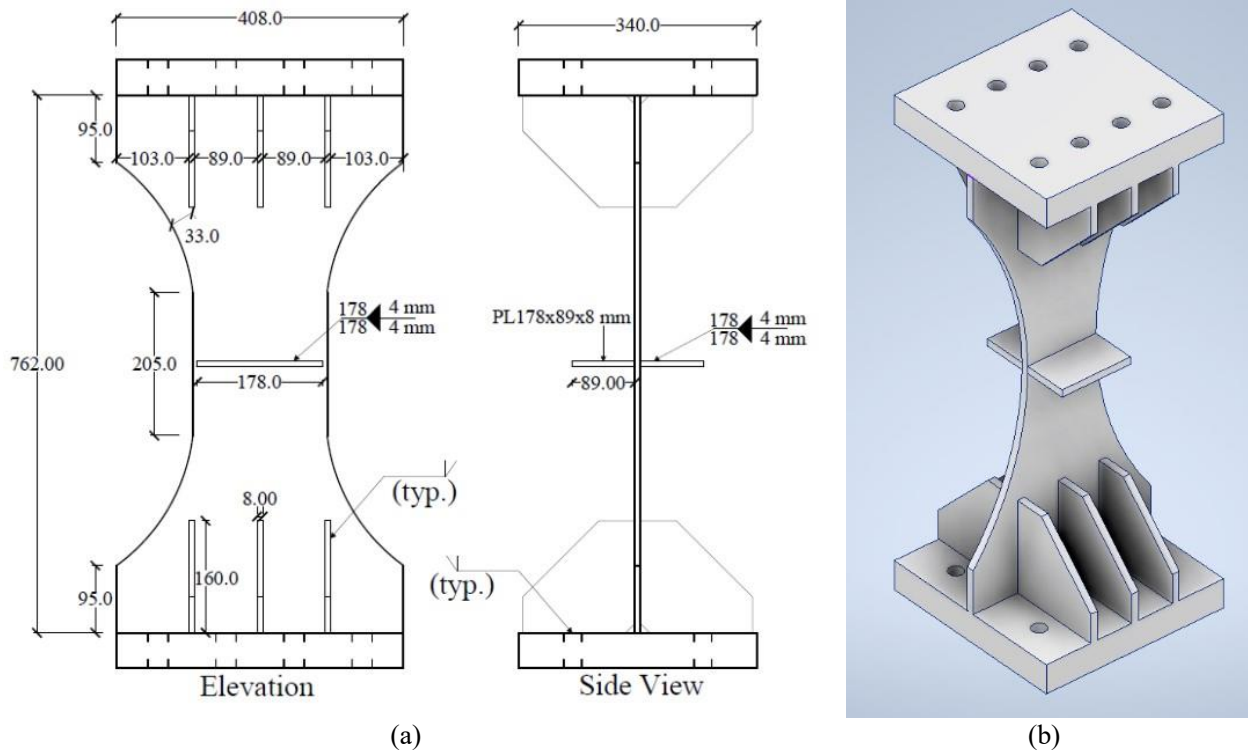


Figure 3.27: General layout of the transverse stiffener specimen (a) dimensions (in millimeters) and (b) 3D render of the T specimen.

3.3.3 Longitudinal Stiffener Specimens

The third set of specimens have longitudinal stiffeners made of AA6061-T6511 welded to the main AA5083 test plate using load bearing fillet welds with size of 4 mm (3/16-in). The dimensions of the longitudinal stiffeners are shown in Figure 3.28. The weld filler is also 5183. With the increased area due to the addition of the longitudinal stiffeners, the ultimate capacity of the specimen was estimated as 855 KN (193 kips). To accommodate the higher force, the layout of the stiffeners at the end connection was modified by utilizing eight stiffeners instead of six. Four of these stiffeners are of the same dimensions as the stiffeners used in Specimens F and T, while four had the dimensions shown in Figure 3.29. The detailed dimensions and a 3D view of the specimen are shown in Figure 3.30.

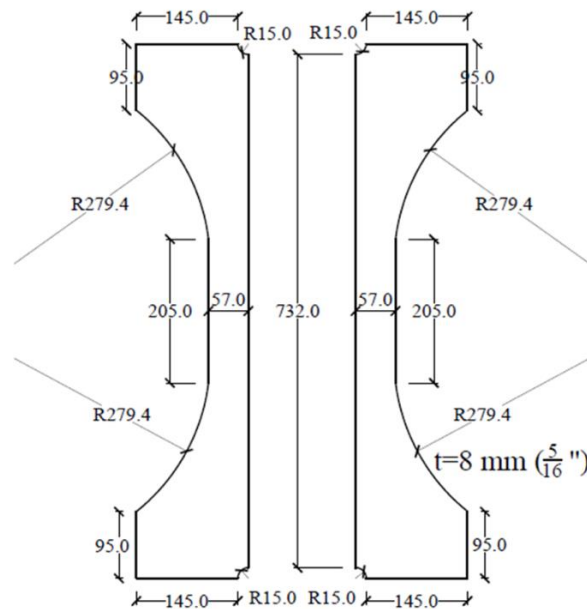


Figure 3.28: Dimensions of the longitudinal stiffener in millimeters.

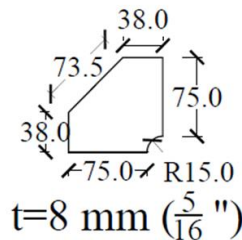


Figure 3.29: Dimensions of the smaller connection stiffeners found in L and LT Specimens.

3.3.5 Connection between Steel End Plate and Aluminum End Plate

The connection between the two end plates is completed utilizing high strength steel bolts. Both the *ANSI/AISC 360* (2016) and the *Aluminum Design Manual* (AA 2020) were reviewed for the design of this connection. Since the *Aluminum Design Manual* (AA 2020) does not permit the use of Group B (e.g., A490) bolts, Group A (e.g., A325) steel bolts with 25.4 mm (1-in) diameter are utilized. With the layout of the end plates shown in Figure 3.24, the ultimate capacity of the bolts based on *ANSI/AISC 360* (2016) is 1,886 kN (424 kips) which provides ample safety factor for the tested samples. To reduce the bearing stresses on the aluminum end plate during testing, square steel plate washers are used on the aluminum side of the connection. A regular hardened F436 steel washer (ASTM F436/F436M, 2019) is used on the steel side. The steel plate washers are made of ASTM A572 Gr. 70 (ASTM A572, 2021) with the dimensions shown in Figure 3.32. Based on these dimensions, a bearing stress of 75 MPa (10.8 ksi) was computed due to the pretensioning load of the bolts. The allowable bearing stress based on AA (2020) is 168 MPa (24 ksi) which is significantly higher than the applied stress. Figure 3.33 shows a picture of the utilized bolt assembly.

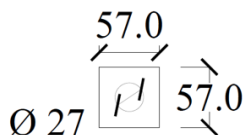


Figure 3.32: Dimensions of the steel plate washer in millimeters.

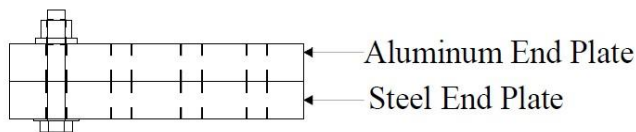


Figure 3.33: The utilized bolt assembly.

3.4 INSTRUMENTATION

Strain gauges, LVDTs, load cells, and digital image correlation (DIC) were used to measure and record strains, displacements in the main test plate and the longitudinal stiffener, and load applied on the aluminum specimen. A National Instruments (NI) cDAQ-9178 was used for data acquisition alongside LabVIEW NXG 3.1 (NI, 2019) to measure and record all data during the test. Figure 3.34 shows the configuration of the NI cDAQ with the different cards that register the strain, load, and displacement from the different sensors. The data acquisition rate was set at 10.0 Hz. The strain gauges and LVDTs were placed on each specimen as shown in Figure 3.35 and Figure 3.36, respectively. Since the strain fields will be acquired using the DIC system, the strain gauges were only placed to monitor and mitigate the out-of-plane eccentricity that may occur while mounting the specimen and tightening the bolts. The displacement was recorded using an AC-LVDT and a DC-LVDT, each with a 150 mm (6-in) stroke that are available in the lab. The LVDTs were placed to measure the gauge length elongation of the test main test plate and the stiffener in a vertical orientation.

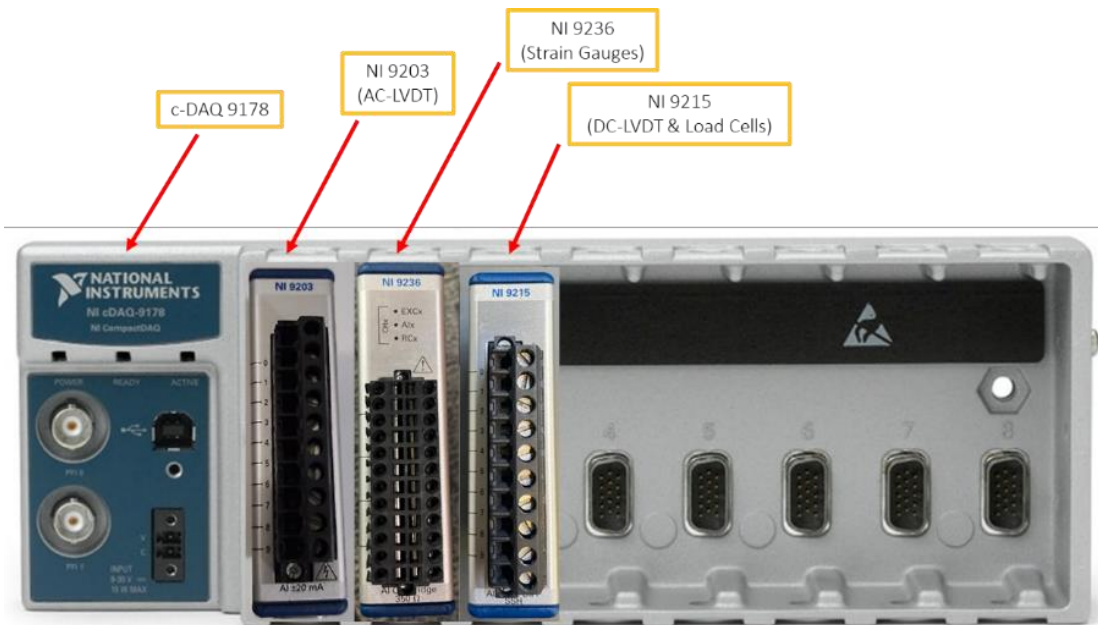


Figure 3.34: NI cDAQ-9178 with the different cards attached for recording data.

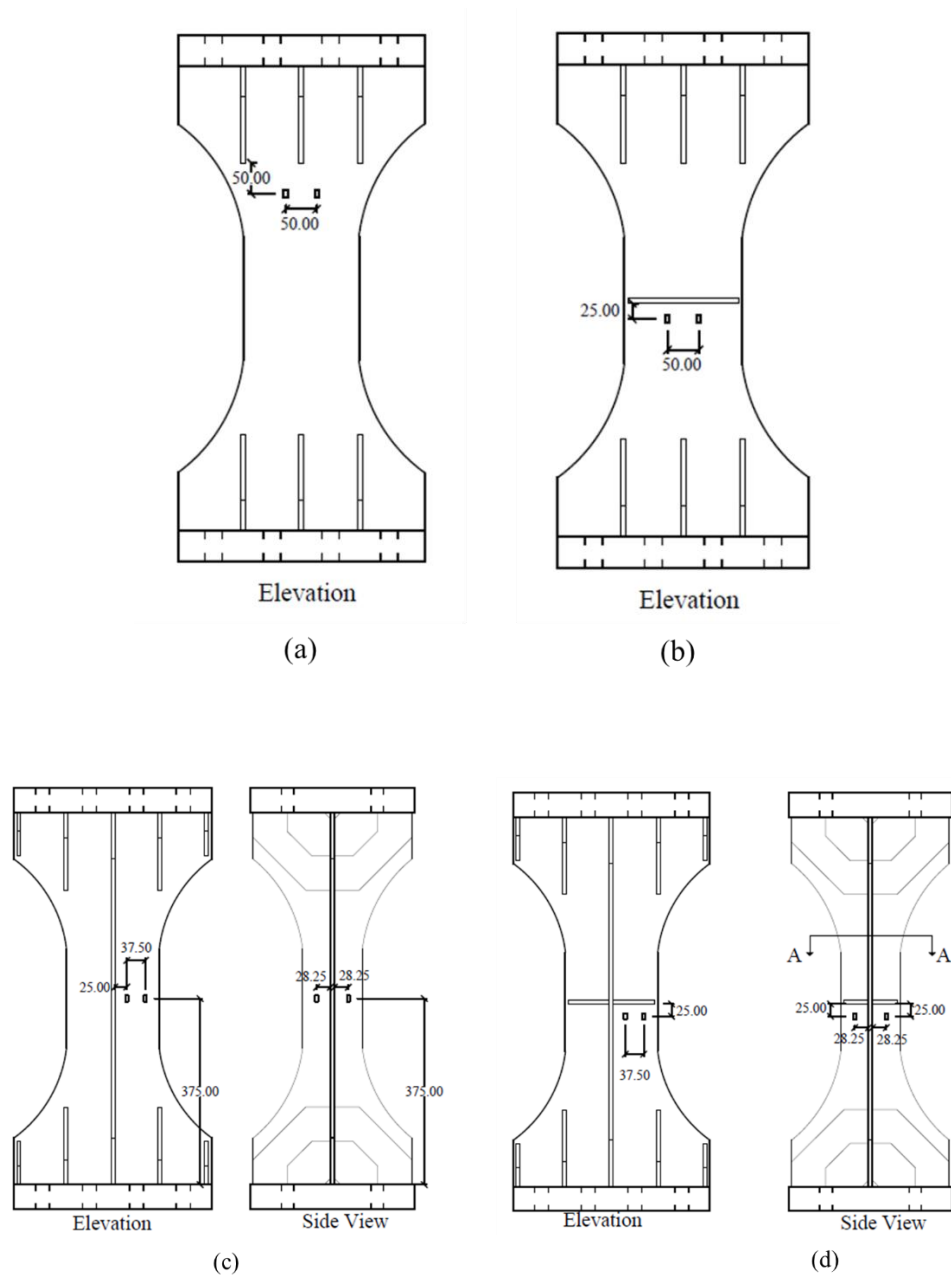
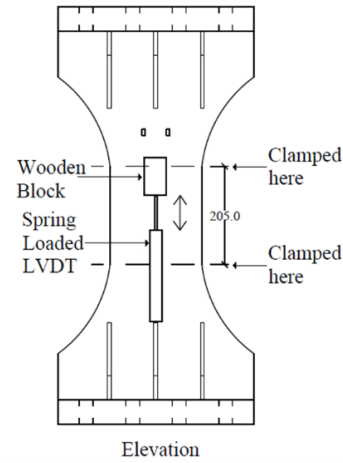
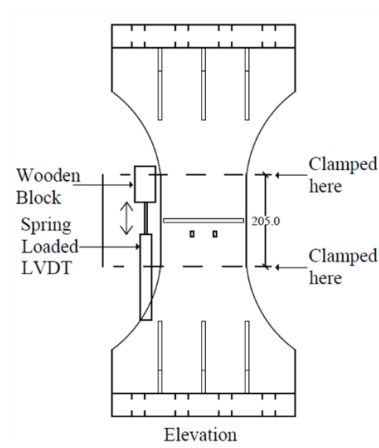


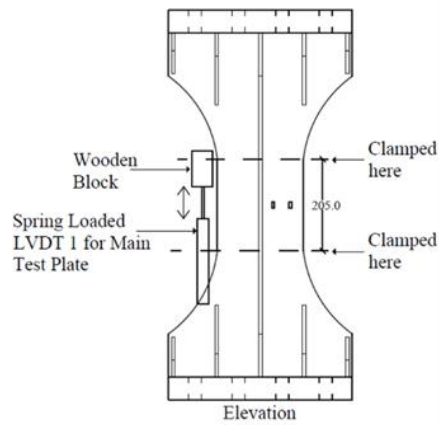
Figure 3.35: Location of the strain gauges for different types of specimens (a) F specimens, (b) T specimens, (c) L specimens, and (d) LT specimens.



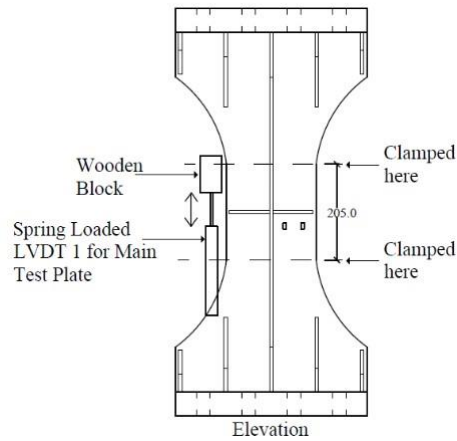
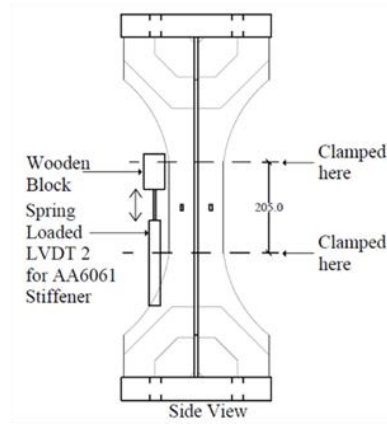
(a)



(b)



(c)



(d)

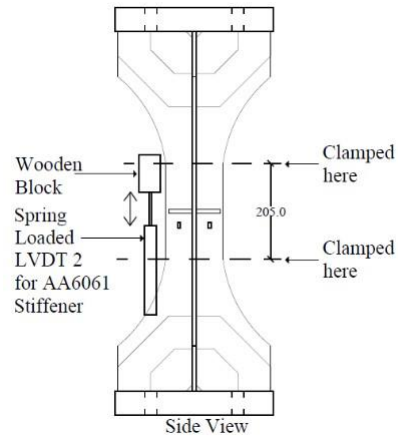


Figure 3.36: Attachment of the LVDTs for different specimens (a) F specimens, (b) T specimens, (c) L specimens, and (d) LT specimens.

The ARAMIS DIC system was a valuable tool that provided a better overall understanding of the behavior of the tested specimens. A large field of view allowed for capturing strain fields in a large area of the specimen. Two cameras with Schneider 24 mm lenses were used to provide a measuring volume of $380 \times 280 \times 240 \text{ mm}^3$ ($15 \times 11 \times 9.45 \text{ in}^3$). The cameras were set at a measuring distance of 697 mm (27.5-in). The DIC system was calibrated prior to every test and the speckle pattern quality was checked to ensure good quality of the results. The DIC system was set to capture three frames per minute given the quasi-static test conditions. Figure 3.37 shows the different components of the ARAMIS DIC setup.



Figure 3.37: Components of the DIC system.

3.5 TEST PROCEDURE

3.5.1 Ancillary Testing

The coupons fabricated for studying the mechanical properties of the BM and HAZ were tested using a universal testing machine in Endeavor Laboratory at Oklahoma State University. A SHIMADZU Testing Machine with 300 KN capacity (67.5 kips) was used to conduct the testing. A 25 mm (1-in) EPSILON E100267 extensometer was used to measure the elongation of the gauge length for all the coupons. This type of extensometer was installed at the beginning of the test and only removed after the failure of the coupon to obtain the full load-deformation profile of the specimen. All the tests were conducted under a controlled constant crosshead displacement rate of 0.6 mm/min.

Since the main aim of this testing program is to investigate the effect of the different welding orientations on the strength of welded aluminum, a quasi-static loading condition was chosen. Huang & Young (2014) recommended a loading rate of 0.4 mm/min that would increase after reaching the ultimate strength to 0.8 mm/min. The initial large-scale test specimen did not display a necking behavior after reaching the ultimate strength; accordingly, a constant loading rate of 0.6 mm/min was adopted for all the specimens tested in this program. Although the load-deformation behavior of some aluminum alloys may not be sensitive to the strain rate of loading (ASTM B557, 2023), negative strain rate sensitivity was reported for AA5083 within the range $10^{-5}/s$ to $10/s$ in Clausen et al. (2004). The study by Clausen et al. (2004) shows a drop in the ultimate strength and increase in the elongation when the strain rate increased from $10^{-5}/s$ to $10/s$. Similar behavior has also been reported in (Tian et al., 2018). The actual strain rate that a ship may be subjected to under normal sea operation is still not well characterized. Giannotti & Stambaugh, (1984) presented research results estimating that marine vessels may be subjected to strain rates up to $10^{-3}/s$ due to sea loading; accordingly, their behavior under normal operation can fall within the strain-rate-dependent region. However, to date, no definitive answers can be found in literature regarding the actual strain rates a ship is subjected to or regarding the effect of the strain rates on the behavior. The chosen load rate in this program resulted in an average nominal strain rate of approximately $5.0 \times 10^{-5}/s$.

3.5.2 Large-Scale Testing

The test procedure presented herein was developed and followed for all large-scale testing. The first step in testing is creating the DIC speckle pattern on the specimen using spray paint. This step was crucial in obtaining high quality DIC results; therefore, after painting, the quality of the speckle pattern was checked using the ARAMIS Software. The specimen was repainted if the average number of pixels per speckle is significantly higher than 7. The painted surface was then protected using plastic wrap to prevent staining during instrumentation and specimen handling. Strain gauges were then applied at their designated locations. These strain gauges were used to assess the out-of-plane eccentricity during specimen mounting. Eccentric loading may occur if the bolts on one side are fully tightened before the opposite side. Accordingly, care was taken to tighten the specimen bolts using multiple passes to minimize the eccentricity. The lower end plate of the specimen is first connected to the lower steel grip assembly, then the fasteners of the upper connection are tightened. After the specimen is placed in position, the DIC system is calibrated

and set in position for image acquisition. The LVDTs are then mounted carefully and securely to the specimen using steel clamps. Observational cameras are set around the specimen to monitor the condition of the specimen from a remote location during the test. Next, the test starts and is conducted under displacement control routine with 0.6 mm/min actuator displacement rate.

3.6 TESTING OF THE INITIAL ALUMINUM SPECIMEN

To ensure that the designed specimens and test setup will be able to fulfill the desired outcome of the testing program, an initial flat plate specimen was requested from the fabricator (i.e., AUSTAL) before manufacturing the remaining specimens. The flat plate specimen arrived at the lab along with two plates of AA5083-H116 and AA6061-T6511 and the welded specimen to be used for ancillary testing. At the same time, the steel fabricator (i.e., W&W|AFCO Steel) delivered the steel grip plates with the bolt assemblies. Figure 3.38 shows the aluminum components and the steel grip plates. Testing of the initial specimen followed the original testing setup discussed in Section 3.2.1. The aluminum specimen was instrumented with strain gauges and the DIC speckle pattern was applied. A 205 mm (8-in) INSTRON I3543-0800-100T-ST extensometer was used to measure the elongation of the gauge length. Again, this test was conducted under displacement control with a crosshead displacement rate of 0.6 mm/min. Figures 3.39 and Figure 3.40 show multiple views of the specimen and testing setup.

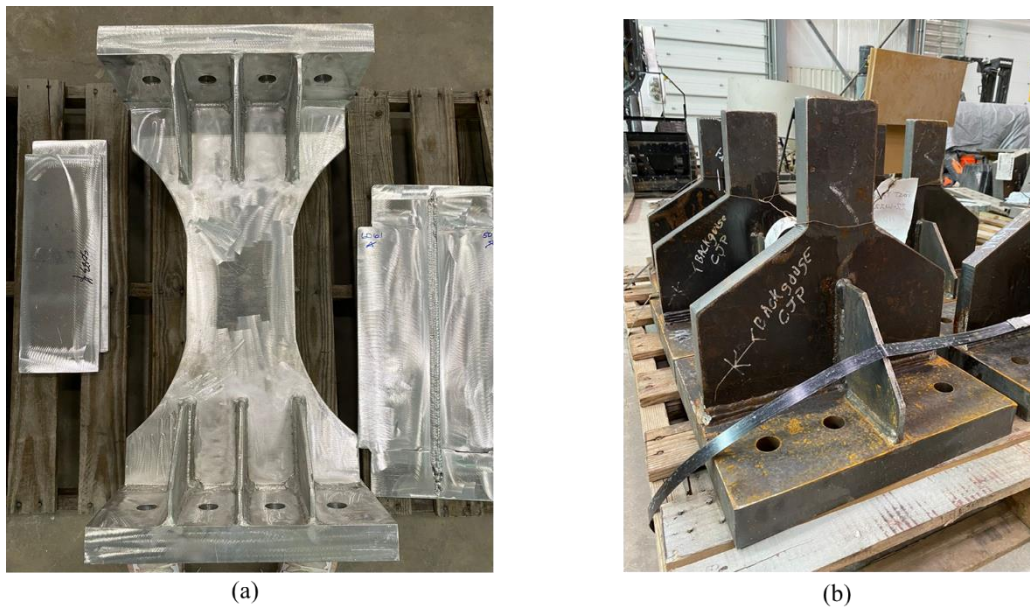


Figure 3.38: Components of the initial aluminum specimen (a) The initial aluminum specimen along with the BM and HAZ plates (b) The steel grip assembly.

While conducting this test, the team experienced multiple software malfunctions that caused the test to be stopped and restarted three times. In one of these software malfunction events, the test data was lost without possibility of retrieval. To ensure the integrity of the test data and prevent future issues while conducting these important tests, the updated test setup was created (see Section 3.2.2) and used to test the 12 specimens included in the test matrix and delivered by AUSTAL in January 2023. Nevertheless, the initial specimen failed during the third testing attempt (attempts were driven by software malfunction) at 530 KN (119 kips). Figure 3.41 shows the location of the failure of the aluminum specimen. This initial test confirmed the feasibility of the testing setup with the bolted connection and the proper design of the end plate region of the specimen.

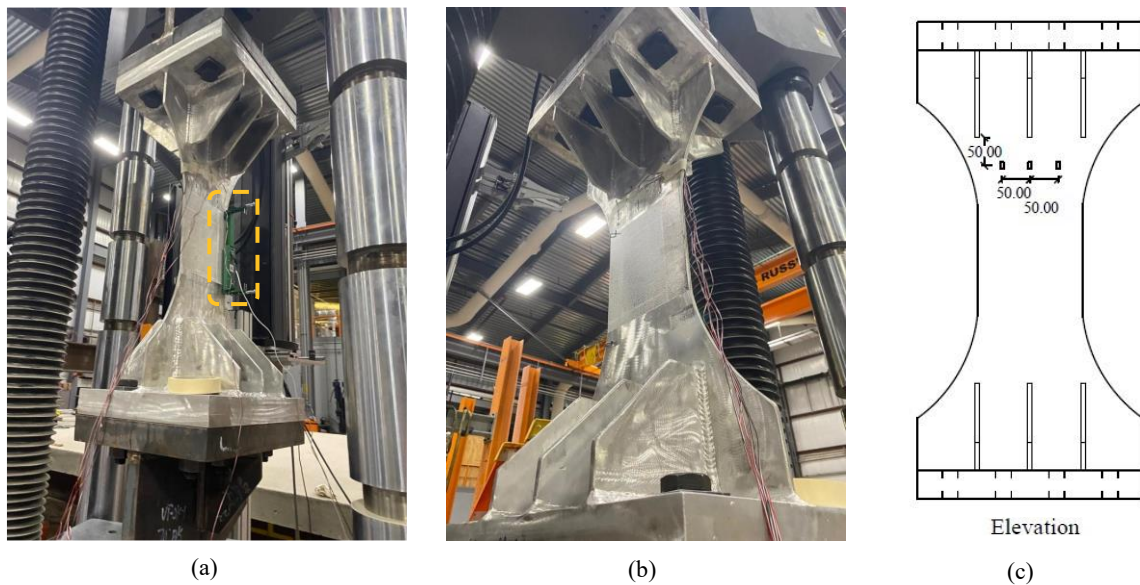


Figure 3.39: The initial aluminum specimen during testing (a) location of the extensometer, (b) general view, and (c) location of the strain gauges.

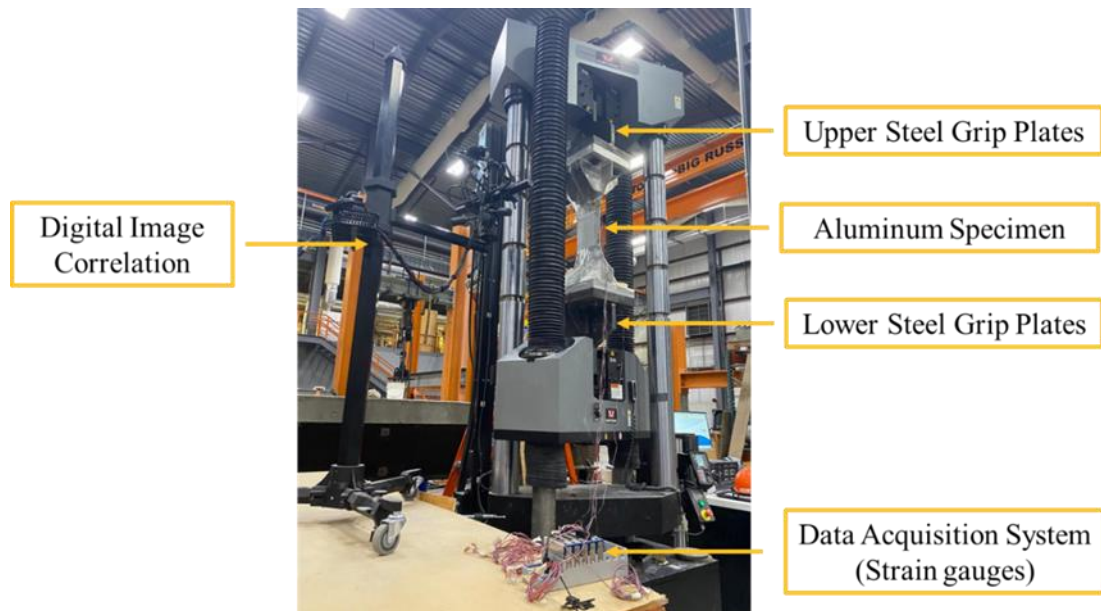


Figure 3.40: Original test setup for the initial aluminum specimen.

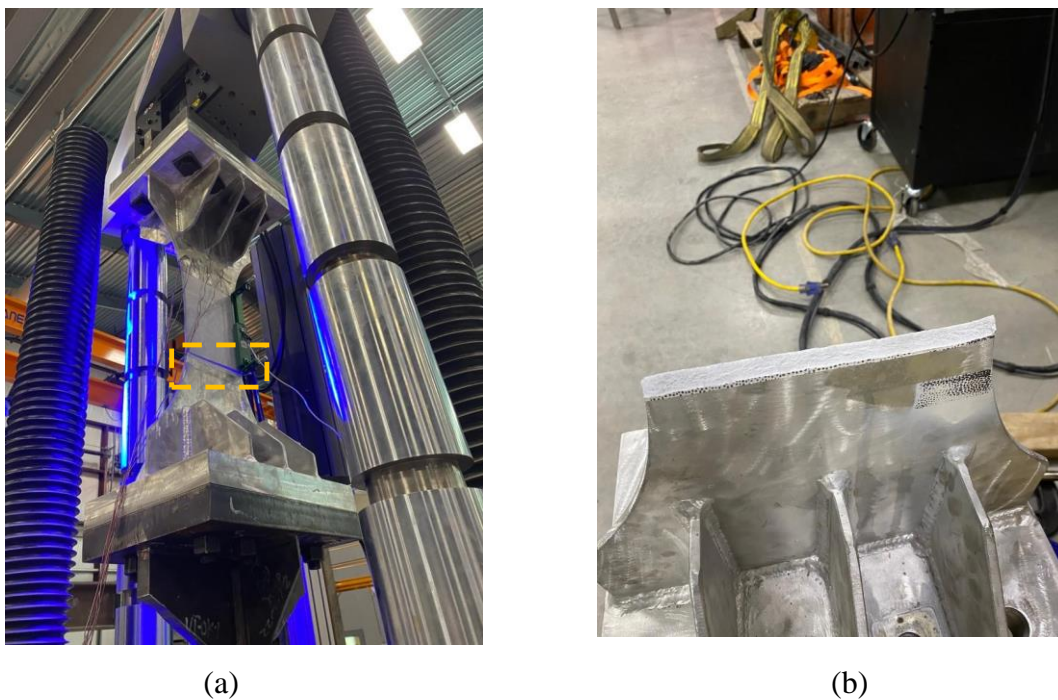


Figure 3.41: Initial test specimen after failure: (a) general view and (b) close up view of the fracture surface.

4 EXPERIMENTAL RESULTS

4.1 ANCILLARY TESTING

While the 12 large-scale specimens were being fabricated, testing of the HAZ and BM coupons for both aluminum alloys was conducted. Figure 4.1 shows the welded plate used to extract the HAZ and BM coupons and the actual coupons for each aluminum alloy. Figure 4.2 shows one of the coupons after concluding the test. The stress-strain behavior of the coupons taken from the HAZ for AA5083-H116 and AA6061-T6511 are shown in Figure 4.3 and Figure 4.4, respectively. The x-marker in both figures represents the failure point of the coupon. Additionally, since only one specimen was created for the ancillary testing, the results obtained are from a singular test for each coupon.

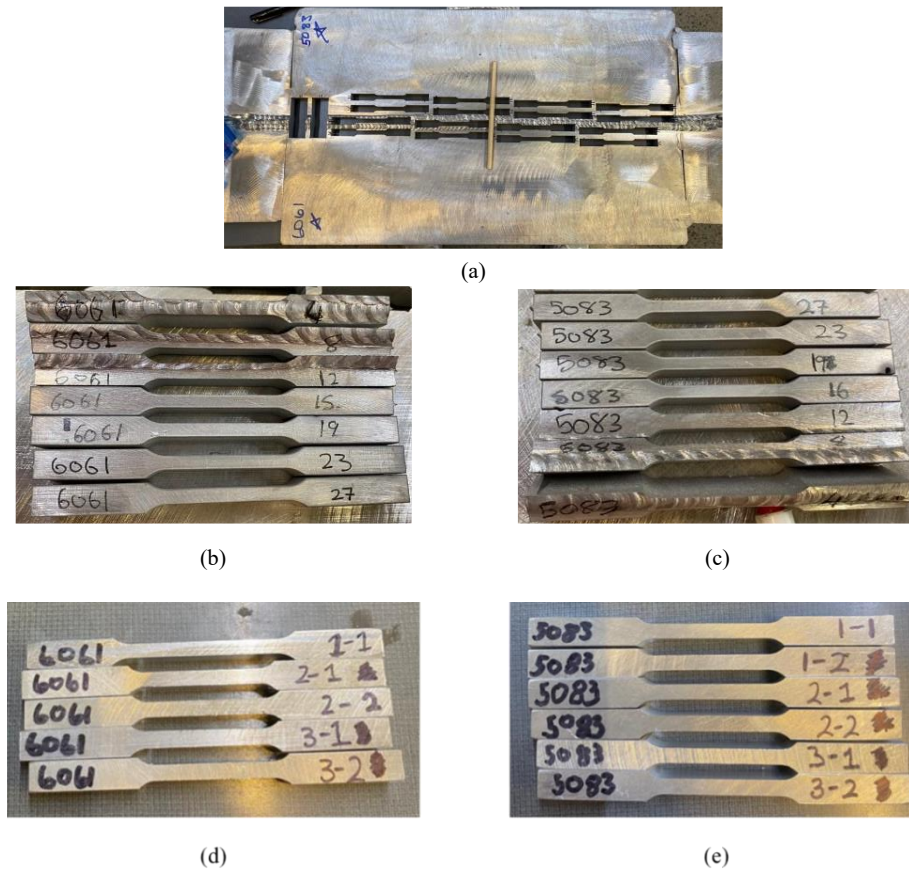


Figure 4.1: Coupons used in ancillary testing (a) location of HAZ coupons after they were extracted from the welded specimen, (b) HAZ coupons for AA5083-H116, (c) HAZ coupons for AA6061-T6 (d) BM coupons for AA6061-T6 (e) BM coupons for AA5083-H116.



Figure 4.2: Close-up view for one of the AA5083-H116 HAZ coupons after the test was completed.

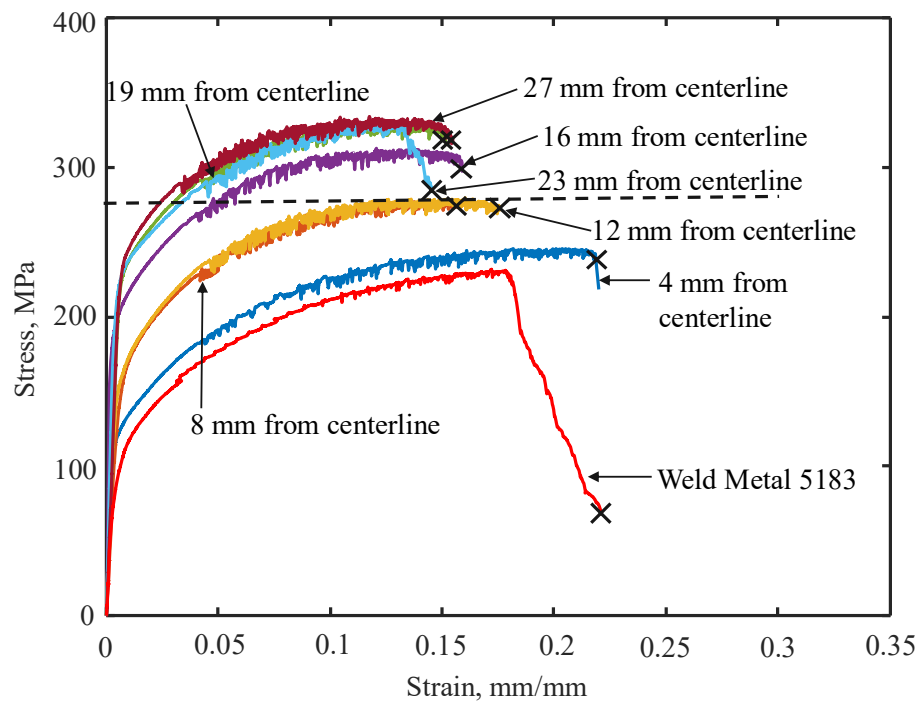


Figure 4.3: Stress-Strain curves across the HAZ for AA5083-H116.

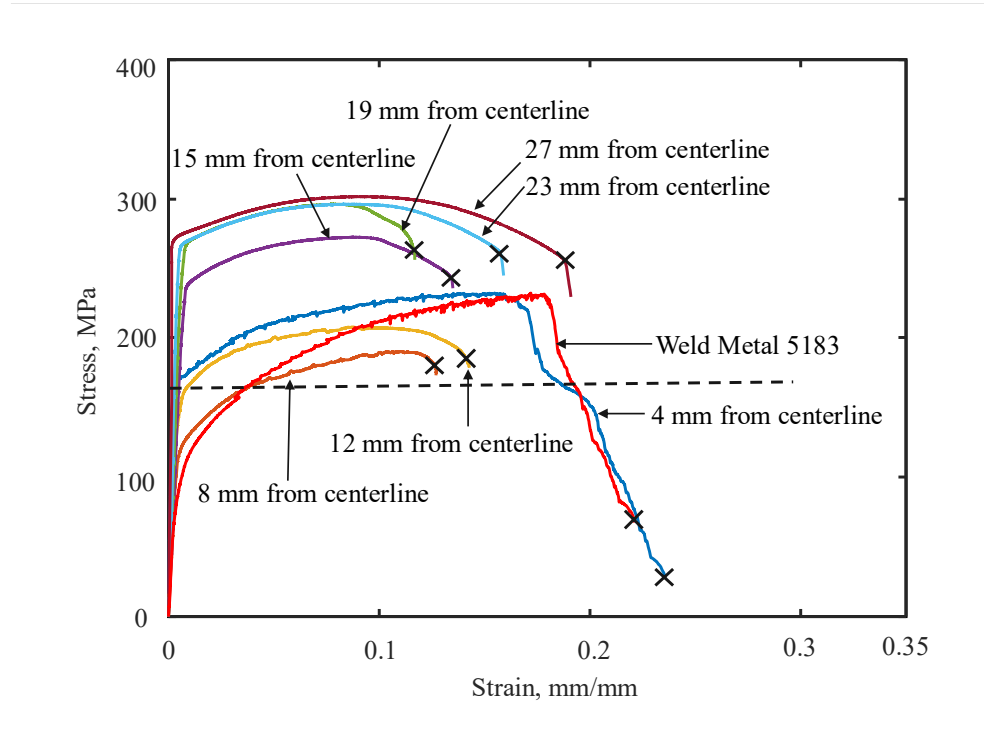


Figure 4.4: Stress-Strain curves across the HAZ for AA6061-T6511.

As seen in Figure 4.3, the mechanical properties change as the distance from the weld line increases. The *Aluminum Design Manual* (AA 2020) utilizes an ultimate tensile strength of welded AA5083-H116 aluminum alloy (i.e., for the HAZ) of 270 MPa (40 ksi). This can be seen as the horizontal line in Figure 4.3. The ultimate tensile strengths of several coupons exceeded this value with an average ultimate tensile strength of 299 MPa (43.3 ksi) across the HAZ. The elongation at the ultimate strength also varies across the HAZ as reported in the figure. The results also show that the 5183 filler metal had lower ultimate strength compared to all tested coupons across the HAZ. Its ultimate strength is also lower than that of the base metal. The *Aluminum Design Manual* (AA 2020) utilizes 270 MPa (40 ksi) as the ultimate strength of 5183; however, for the welded conditions investigated in this report, the experimentally obtained ultimate strength, reported in Figure 4.3, of this filler metal is 232 MPa (33.56 ksi). It should be noted, however, that the filler metal has higher ductility than the HAZ coupons. In addition, the zone closest to the weld metal exhibited higher elongation (i.e., similar to the filler metal) since the fusion weld affected the mechanical properties in that region.

The results from the AA6061-T6511 testing, shown in Figure 4.4, depict the different behavior compared to that of AA5083-H116 coupons. While the AA6061-T6511 coupons

displayed a ductile necking behavior, the AA5083-H116 coupons fractured suddenly at ultimate loads. The *Aluminum Design Manual* (AA 2020) reports an ultimate HAZ tensile strength for AA6061-T6511 of 165 MPa (24 ksi). As seen in the figure, this value is very conservative compared to the actual strength obtained from this testing. The average ultimate strength of the tested HAZ coupons is 257 MPa (37.2 ksi). The coefficient of variation (COV) of the fracture strain across the HAZ of AA6061-T6511 is approximately 18% showing that the welding process can cause high variability in the ductility within the HAZ. Again, the HAZ coupons closer to the weld displayed a stress-strain behavior that is similar to that of the weld coupons. Tables 4.1, 4.2, and 4.3, summarize the HAZ coupon testing results for the AA5083, AA6061, and the 5183 filler metal, respectively.

Table 4.1: Stress-strain characteristics of AA5083-H116 HAZ coupons

Specimen Type	Tensile Yield Strength, F_{ty} MPa	Yield Strain, ϵ_y mm/mm	Ultimate Tensile Strength, F_{tu} MPa	Strain at Ultimate, ϵ_u mm/mm
4 mm	115.7	0.0040	243.2	0.217
8 mm	159.0	0.0077	276.0	0.158
12 mm	161.3	0.0072	274.3	0.175
15 mm	185.7	0.0029	307.1	0.158
19 mm	235.6	0.0092	328.6	0.146
23 mm	215.5	0.005	330.3	0.136
27 mm	234.2	0.007	331.6	0.141

Table 4.2: Stress-strain characteristics of AA6061-T6511 HAZ coupons

Specimen Type	Tensile Yield Strength, F_{ty} MPa	Yield Strain, ϵ_y mm/mm	Tensile Ultimate Strength, F_{tu} MPa	Strain at Ultimate, ϵ_u mm/mm	Fracture Strength, MPa	Strain at Fracture, mm/mm
4 mm	169.7	0.0045	232.1	0.15	218.9	0.17
8 mm	120.8	0.0058	190.6	0.1113	178.4	0.127
12 mm	158.6	0.0067	207.5	0.0862	178.0	0.143
15 mm	236.3	0.0083	272.2	0.0885	242.7	0.1342
19 mm	266.5	0.0080	296.3	0.0794	262.1	0.1165
23 mm	264.6	0.0054	296.1	0.086	245.0	0.1587
27 mm	273.7	0.0051	301.6	0.0908	229.6	0.1911

Table 4.3: Stress-strain characteristics of 5183 weld metal coupons

Specimen Type	Tensile Yield Strength, F_{ty} MPa	Yield Strain, ϵ_y mm/mm	Ultimate Tensile Strength, F_{tu} MPa	Strain at Ultimate, ϵ_u mm/mm	Fracture Strength, MPa	Strain at Fracture, mm/mm
Weld Metal	105.9	0.007	231.4	0.178	72	0.224

Comparing the behavior of the two alloys shows that while the AA5083-H116 specimens shows a ‘jerky’ stress-strain behavior, the AA6061-T6511 specimens did not display this behavior except for the coupon closest to the weld line. This ‘jerky’ flow seen on the stress-strain curve corresponds to the serration yielding due to the Portevin-Le Chatelier (PLC) bands (Portevin & Le Chatelier, 1923). Some aluminum alloys are characterized by narrow intense plastic shear bands that initiate after yielding and propagate in a homogeneously deforming specimen (Zhang et al., 2012) causing such serrations in the behavior. PLC bands form due to the dynamic strain aging (DSA) mechanism that describes the dynamic relationship between the mobile dislocations and the solute atoms. In aluminum alloys, magnesium is the primary solute element responsible for the existence of the DSA mechanism (Dahdouch et al., 2022). The solute atoms diffuse and disperse around the movable dislocation line, restraining the dislocation and immobilizing their movement. This resistance is overpowered by applying more stress resulting in the separation of the movable dislocations from the solute-atom atmosphere. This process will continue to occur if the movable dislocations continue to break free and continue their motion. This results in the ‘jerky’ or ‘serrated flow’ that is manifested by the fluctuations of the stress-strain curve (Zhang et al., 2020).

In addition to the HAZ coupons that were extracted from the provided plates, base metal coupons were also extracted from the plates by machining. These base metal coupons were extracted at least 38 mm (1.5-in) away from the weld center line. Figure 4.5 and Figure 4.6 show stress-strain curves resulting from the coupon testing of the AA5083-H116 and AA6061-T6511, respectively. Based on the testing results, the ultimate tensile strength of AA5083-H116 coupons had a COV of 7% while the fracture strain had a COV of 12%. The *Aluminum Design Manual* (AA 2020) reports an ultimate tensile strength for this alloy of 305 MPa (44 ksi). This design value is based on the acceptable bounds adopted by ASTM B928-15 (ASTM, 2015). This design value

is 17% conservative when compared to the average ultimate strength of 366 MPa (53 ksi) resulting from the conducted coupon testing.

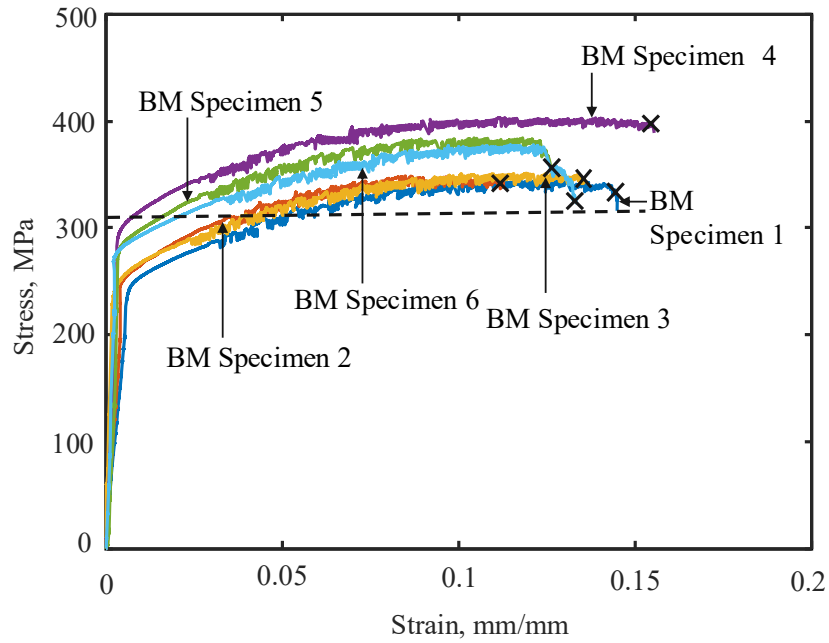


Figure 4.5: Stress-Strain curves of the base metal coupons of AA5083-H116.

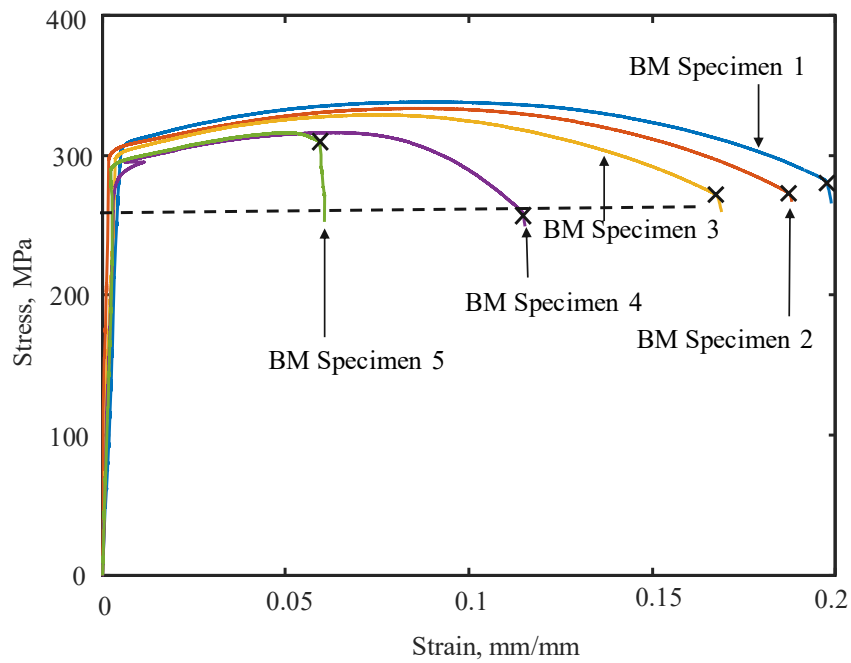


Figure 4.6: Stress-Strain curves of the base metal coupons of AA6061-T6511.

The ultimate tensile strengths of AA6061-T6511 coupons did not exhibit such high level of variability in the ultimate strength (COV = 3%). However, the COV of the strain at ultimate load is 22% showing the high variability in the ductility of this alloy. The fracture strain exhibited an even higher variability with COV of 40% with one coupon failing to meet the minimum elongation requirement of 10% for this aluminum alloy required by ASTM B316-10 (ASTM, 2010). The design value of the ultimate tensile strength of AA6061-T6511 is considered 260 MPa (38 ksi) (*Aluminum Design Manual* (AA 2020) which is 20% conservative when compared to the average ultimate tensile strengths of 327 MPa (47.4 ksi) for the coupons tested in this program. Tables 4.4, and 4.5 summarize the results of the BM testing for both alloys.

Table 4.4: Strength characteristics of AA5083-H116 BM Coupons

Specimen Number	Tensile Yield Strength, F_{ty} MPa	Yield Strain, ϵ_y mm/mm	Ultimate Tensile Strength, F_{tu} MPa	Strain at ultimate, ϵ_u mm/mm
BM Specimen 1	253.0	0.0095	343.4	0.13
BM Specimen 2	260.5	0.0077	346.2	0.11
BM Specimen 3	253.0	0.0044	348.9	0.134
BM Specimen 4	306.3	0.0061	398.5	0.1548
BM Specimen 5	290.0	0.0063	381.6	0.123
BM Specimen 6	278.9	0.0036	375.5	0.124

Table 4.5: Strength characteristics of AA6061-T6511 BM Coupons

Specimen Number	Tensile Yield Strength, F_{ty} MPa	Yield Strain, ϵ_y mm/mm	Ultimate Tensile Strength, F_{tu} MPa	Strain at ultimate, ϵ_u mm/mm	Fracture Strength, MPa	Strain at fracture, mm/mm
BM Specimen 1	309.6	0.0073	338.1	0.0901	280.7	0.1976
BM Specimen 2	306.1	0.0047	333.8	0.085	271.6	0.187
BM Specimen 3	304.1	0.0072	329.4	0.0744	271.0	0.168
BM Specimen 4	287.1	0.0053	316.3	0.0629	257.8	0.1147
BM Specimen 5	296.2	0.0053	316.3	0.0504	308.4	0.059

4.2 LARGE-SCALE TESTING

Twelve large-scale specimens were delivered in January 2023 with three specimens from each stiffener configuration. The large-scale testing program started with specimen F1, followed by T1, L1, and LT1. The same cycle was repeated until all specimens were tested. The as-built dimensions closely followed the submitted drawings (see Figures 3.23 – 3.31) except for the thickness of the AA6061 stiffeners, which were fabricated with 10 mm (13/32-in) thick plates instead of 8 mm (5/16-in) due to plate availability at the time of fabrication.

4.2.1 Testing Results

4.2.1.1 Flat Plate Specimen Results

The flat plate specimens using AA5083-H116 are considered as the control specimens in the adopted test matrix. The results can also be compared to those of the small-scale coupons to quantify the scale effects. Strain gauges were applied to both sides of the specimens to quantify the out-of-plane eccentricity while LVDTs were installed to measure the elongation of the gauge length. As indicated in Section 3.4, DIC was also utilized to measure the strain fields during testing. The load-deformation results of the three flat plate specimens are shown in Figure 4.7. The three flat plates specimens failed in a sudden manner. The x-marker in Figure 4.7, as well as the remaining ones represents the failure point of the specimen. Note that Specimen F1 was loaded and unloaded twice as part of the final refinements of the testing protocol and failed in the third load cycle. The results shown in Figure 4.7 for F1 represent the envelope of the three load cycles. Table 4.6 shows the ultimate capacity and elongation at ultimate for the three flat plate specimens.

Table 4.6: Results of flat plate specimens

Specimen number	Ultimate force, KN (kip)	Ultimate elongation, mm (in)
F1	539 (121)	53 (2.09)
F2	543 (122)	33 (1.30)
F3	533 (120)	23 (0.91)

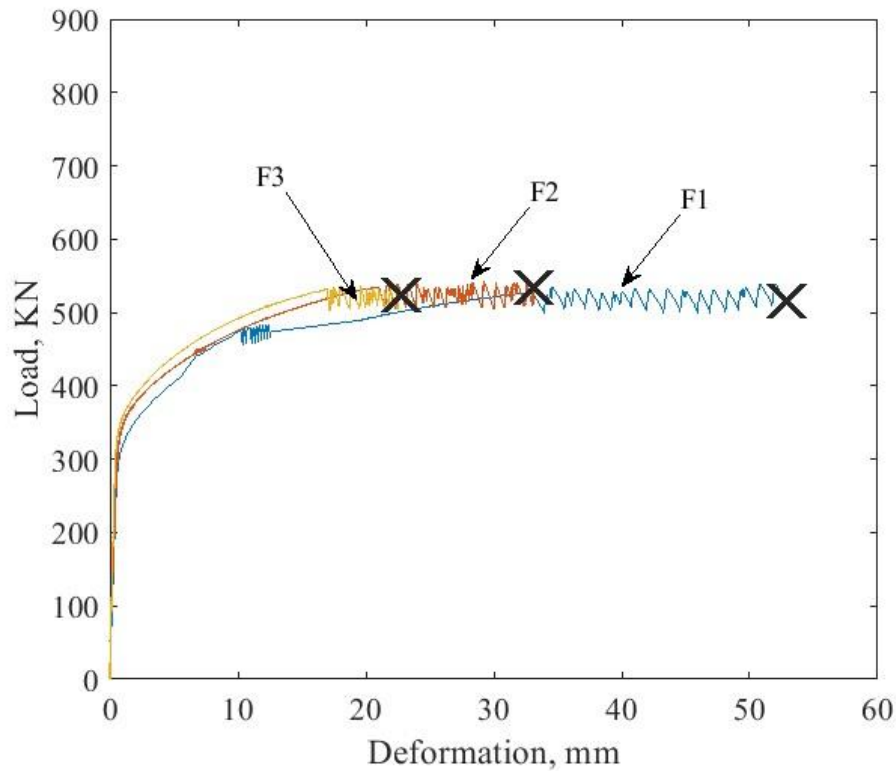


Figure 4.7: Load-deformation curves of flat plate specimens.

Based on the results seen in the figure, the specimens exhibited high variability in the fracture strain with COV of 42% considering the three specimens and 26% if only F2 and F3 are considered. This is significantly higher variability compared to the results of the coupons tested as part of the ancillary testing program which exhibited only 12% COV for the fracture strain. This is due to the highly variable serration behavior in these large specimens evident by the sawtooth pattern of the load deformation profile in the plastic region. The ultimate strength showed a consistent behavior, and the yield tensile strength displayed a low variability with COV of only 3%. Figure 4.8 shows the three flat plate specimens after the tests were concluded while Figure 4.9 shows a close up view of the fracture surfaces of Specimen F3.



(a)



(b)



(c)

Figure 4.8: Flat plat specimen post failure (a) F1, (b) F2, and (c) F3.

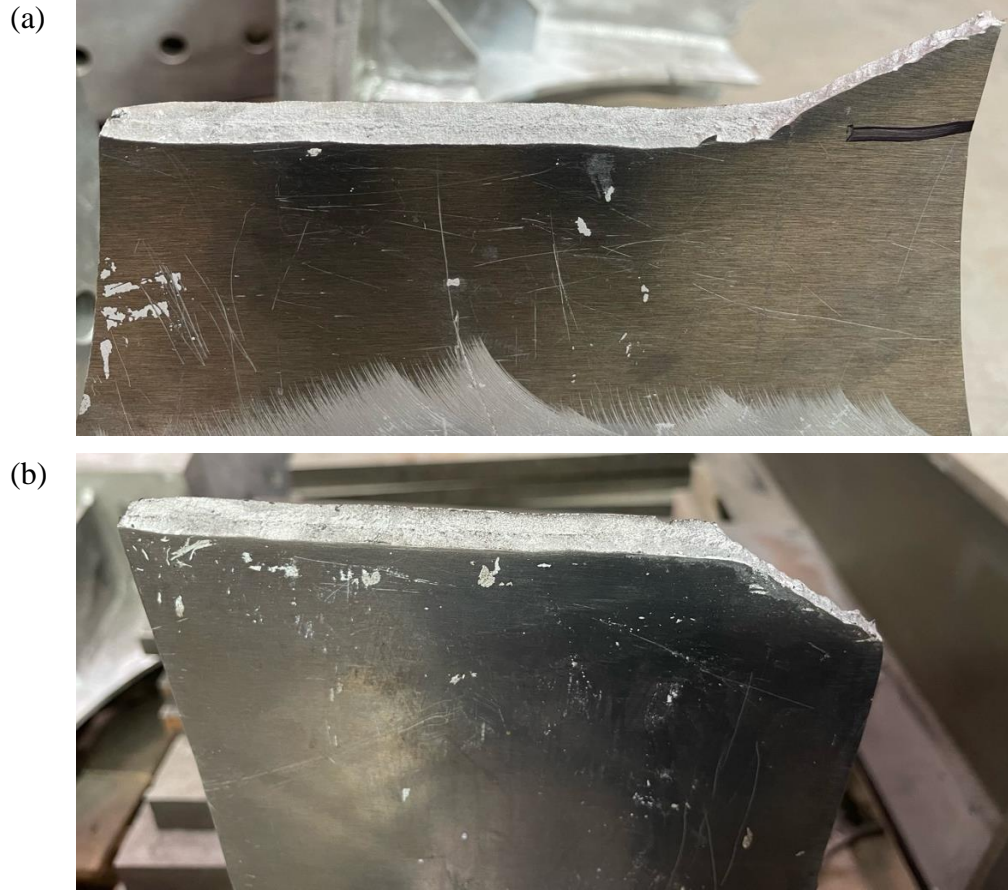


Figure 4.9 Fracture surfaces of Specimen F3: (a) upper fracture surface and (b) lower fracture surface (other specimens showed similar behavior)

The DIC results, showing the strain fields in the loading direction, are provided for each flat plate specimen in Figure 4.10 - 4.12. Each figure shows a view before the onset of serrations, a second at the onset of the first serration, and the strain fields for the last frame captured before specimen failure. These figures clearly show the serration behavior occurring through the test. These serrations represent the main mechanism for accommodating the plastic deformation within the specimen. The DIC was able to capture the strain localization or PLC bands that occur at 45 degrees and continue up to failure. Although the serrations themselves may not be the reason behind specimen failure, they can drive the failure if the serration band occurs at a high strain concentration point (Zhang et al., 2020a). Flat plate Specimen F3 showed that the PLC bands can also reverse in direction during the test (see Figure 4.12(c)). As shown in Figure 4.10(b), the strain values can jump by up to 50% within the serration band. The strain values at failure were consistent for the three specimens.

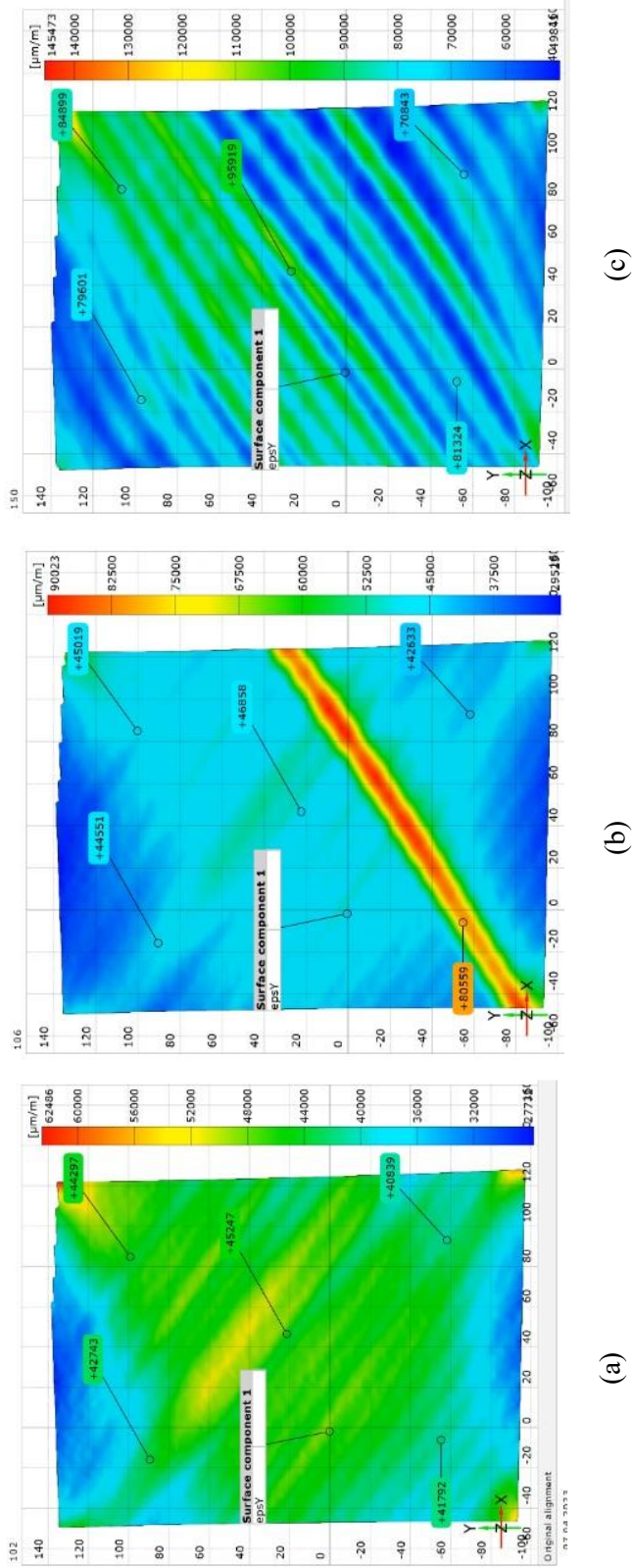


Figure 4.10: DIC results for specimen F1 (a) strain before the onset of serration, (b) strain at the onset of the first serration, and (c) strain towards the end of the test.

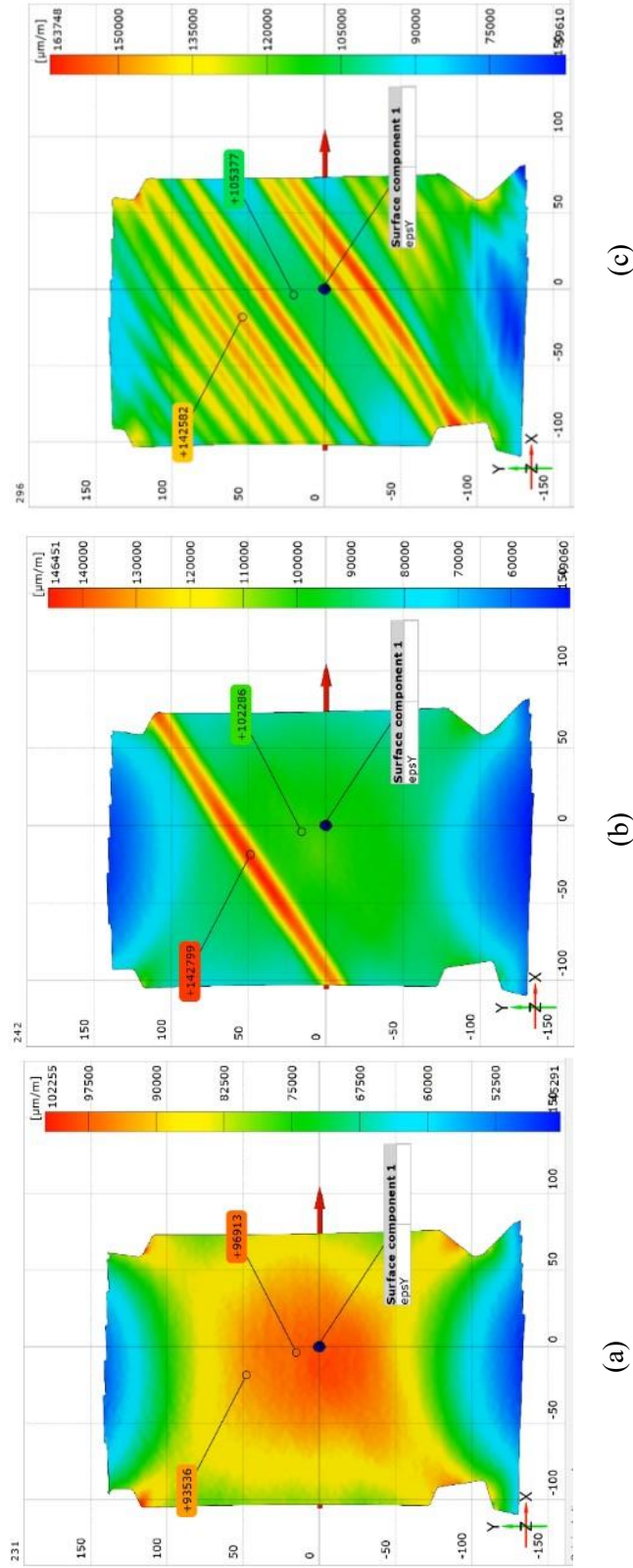


Figure 4.11: DIC results for specimen F2 (a) strain before the onset of serration, (b) strain at the onset of the first serration, and (c) strain towards the end of the test.

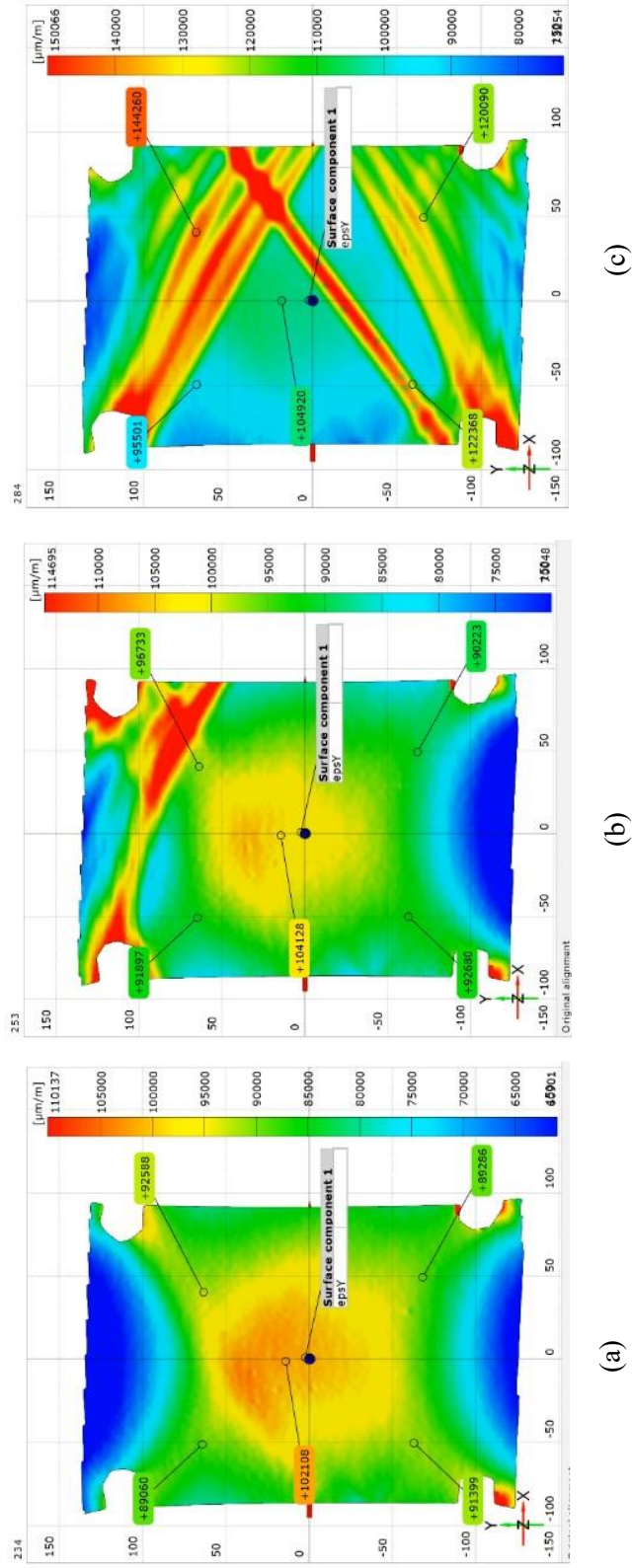


Figure 4.12: DIC results for specimen F1 (a) strain at the beginning of the test, (b) strain at the onset of the first serration, and (c) strain towards the end of the test.

Figure 4.13 shows the load and strain versus time for Specimen F1. As seen in the figure, the strain gauges may be able to capture the jump in strains occurring with the PLC band; especially if the band occurs in the vicinity of the strain gauge. However, as also seen in Figure 4.13(b) most strain gauges (e.g., Strain 4) would get detached (i.e., epoxy failure) at the beginning of the plastic deformation region due to the high strain values reached. Accordingly, the DIC was proven to be an invaluable tool for these tests.

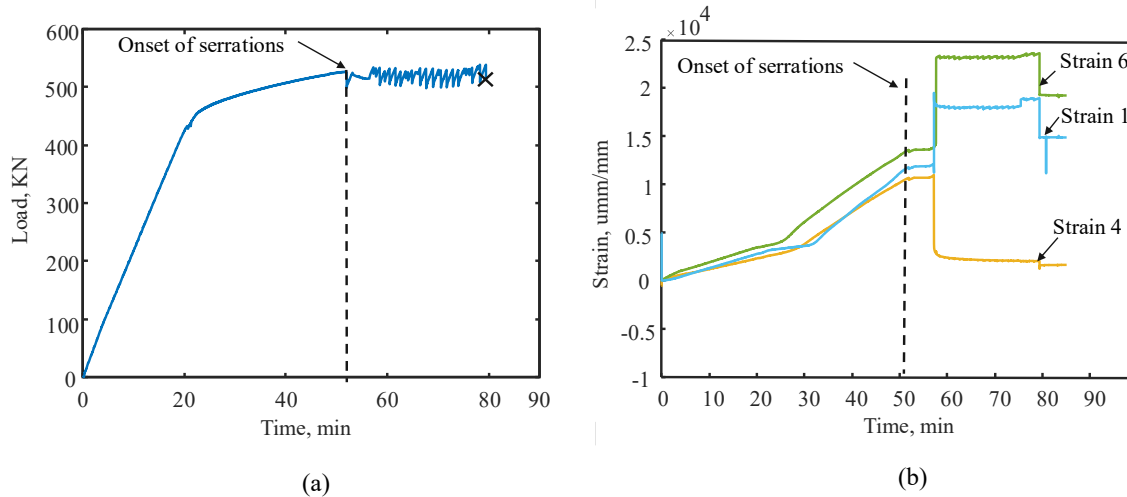


Figure 4.13: Specimen F1 results: (a) load vs time showing the onset of serrations, and (b) strain vs time showing strain readings and how they react to the onset of serrations.

4.2.1.2 Transverse Stiffener Specimen Results

Transverse stiffener specimens are composed of a flat plate specimen with two transverse stiffeners welded on both sides using four lines of non-load carrying fillet welds. The main test plate is AA5083-H116 while the stiffener is AA6061-T6511 with 5183 filler metal. The elongation of the gauge length of the specimen was measured using one spring loaded LVDT that was carefully placed on the specimen using clamps. The load-deformation curves of the three transverse stiffener specimens are shown in Figure 4.14. Note that Specimen T1 experienced LVDT malfunction during the test that registered higher elongation; however, the recorded strength is accurate. All transverse stiffener specimens failed within the 25 mm (1-in) region representing the HAZ for the main plate as seen in Figure 4.15. The figure also shows a close-up view of the failure surface of one of the specimens while Figure 4.16 shows the three specimens after the tests were conducted.

The DIC results for the three specimens are shown in Figures 4.17-4.19. Serrations were also observed in the three transverse stiffener specimens. Similar to the flat plate specimens, serrations were the main mechanism for accommodating plastic deformation. The DIC showed the high strain concentrations occurring at the HAZ near the weld during most of the tests. This is expected since the welding process alters the mechanical properties of this region significantly. Furthermore, the PLC bands existed in two perpendicular 45 degrees orientations. The DIC results also showed that the strains along the weld line are not uniformly distributed which can be exacerbated with the formation of serrations. Table 4.7 shows the ultimate capacity and ultimate elongation for the three transverse stiffener specimens.

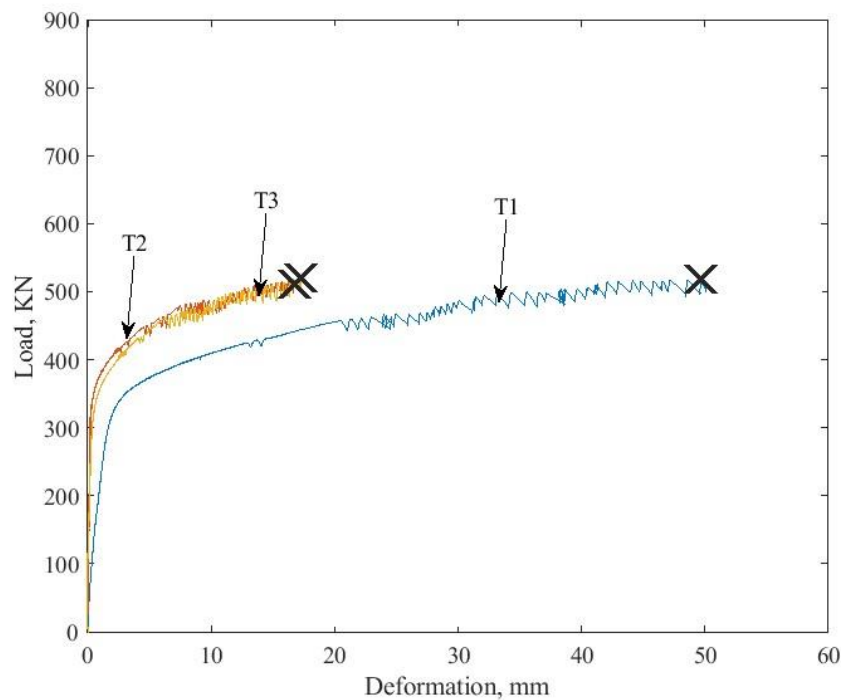
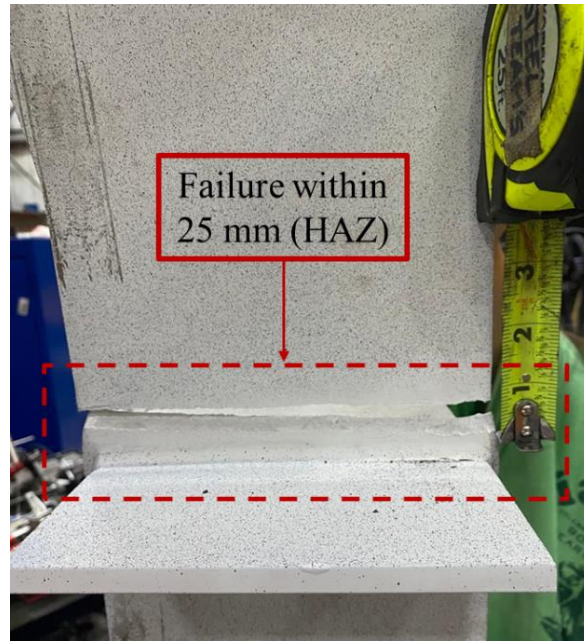


Figure 4.14: Load-deformation curves for all transverse stiffener specimens.

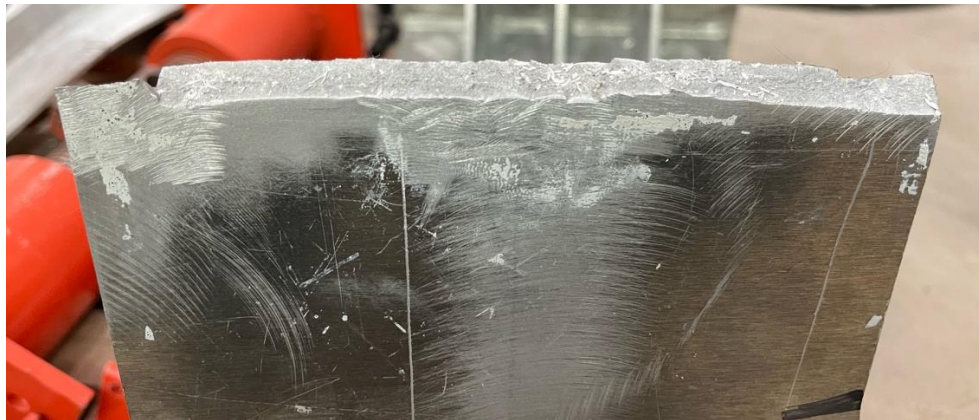
Table 4.7: Results of Transverse Stiffener Specimens

Specimen number	Ultimate force, KN (kip)	Ultimate elongation, mm (in)
T1	521 (117)	51 (2.0)
T2	521 (117)	18 (0.71)
T3	521 (117)	17 (0.67)

(a)



(b)



(c)



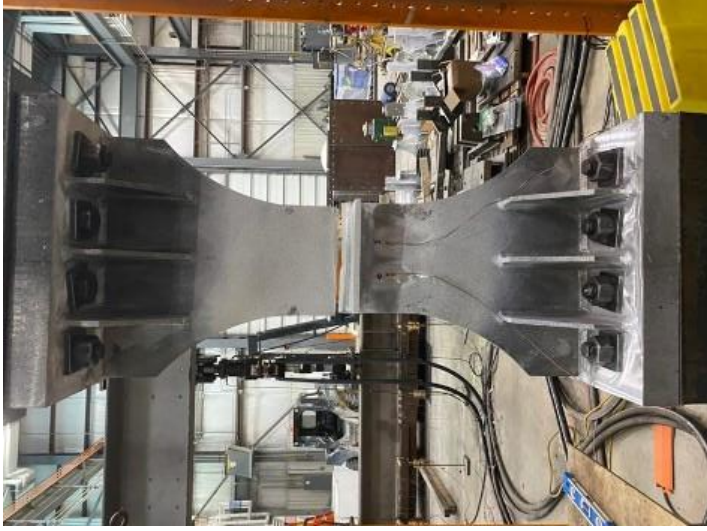
Figure 4.15: Failure of the T specimens: (a) general location of failure, (b) upper fracture surface of Specimen T2, and (c) lower fracture surface of T2.



(a)



(b)



(c)

Figure 4.16: Transverse stiffener specimen post failure (a) T1 (b) T2 (c) T3

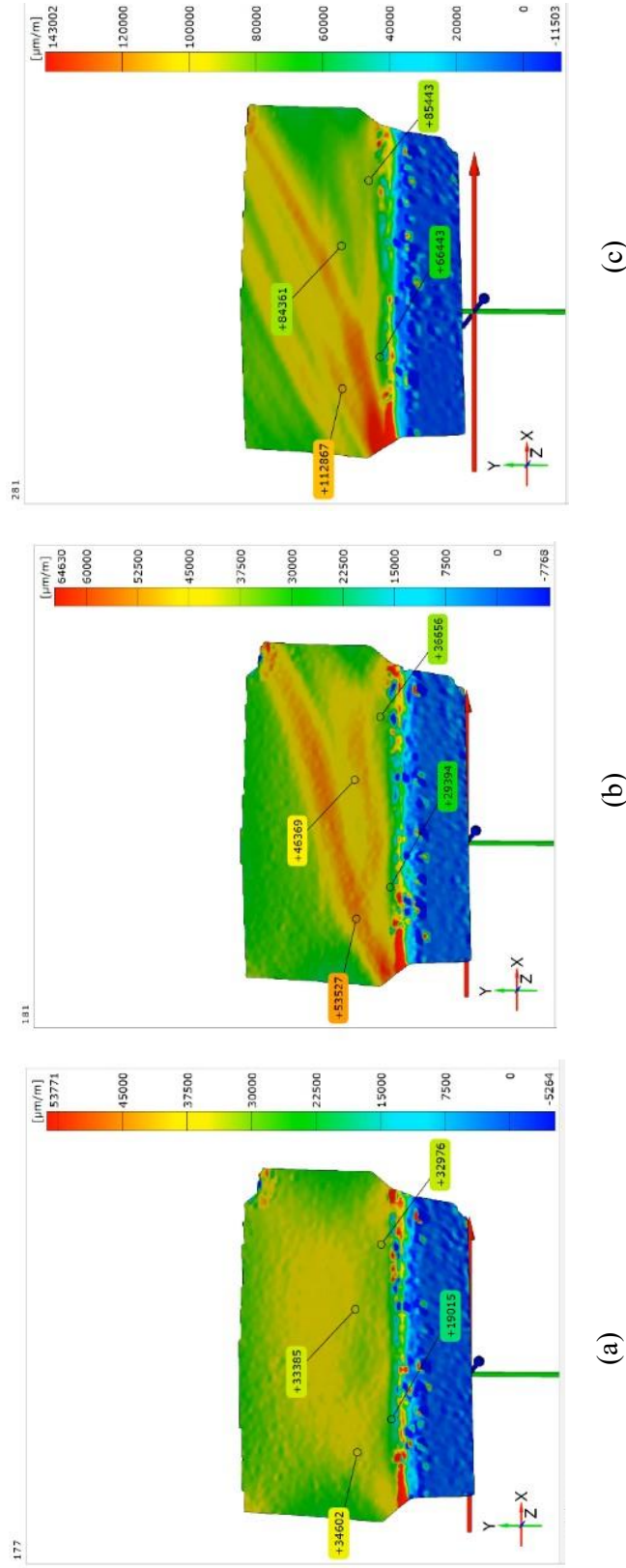


Figure 4.17: DIC results for specimen T1 (a) strain before the onset of serrations, (b) strain at the onset of the first serration, and (c) strain towards the end of the test.

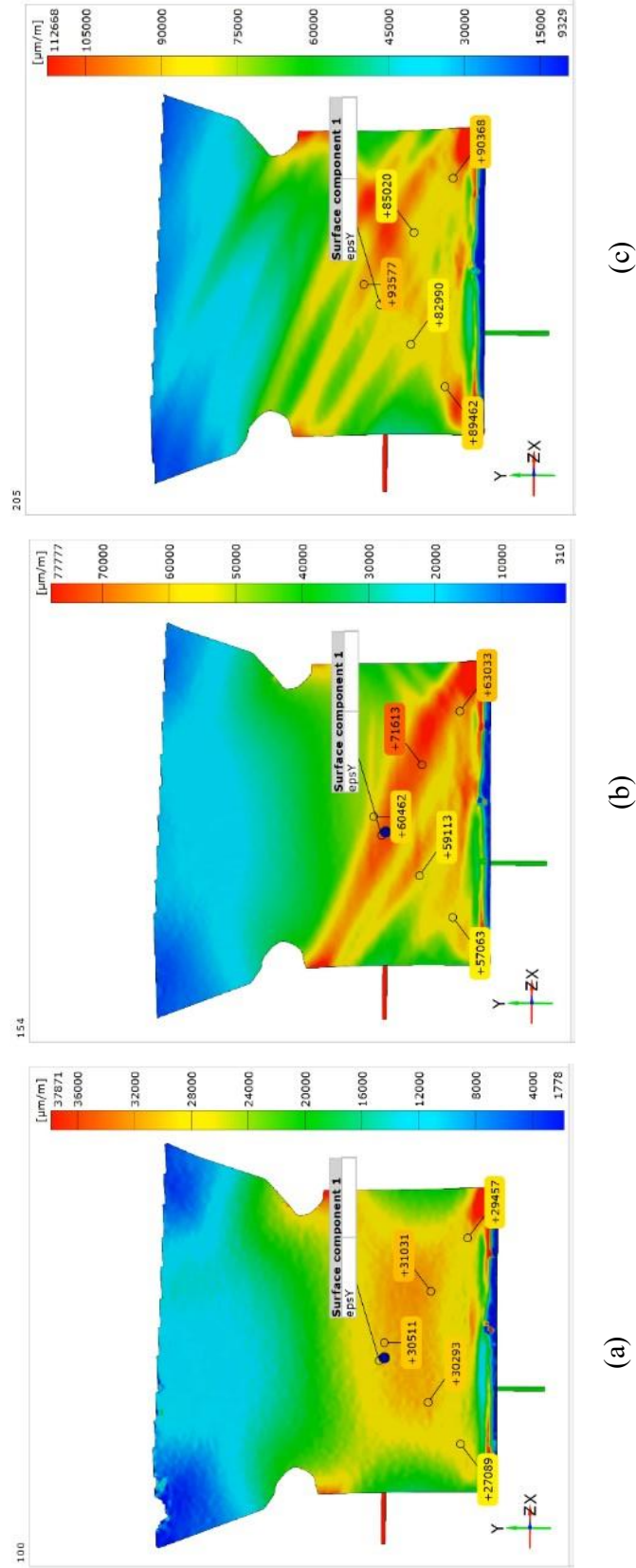


Figure 4.18: DIC results for specimen T2 (a) strain before the onset of serrations, (b) strain at the onset of the first serration, and (c) strain towards the end of the test.

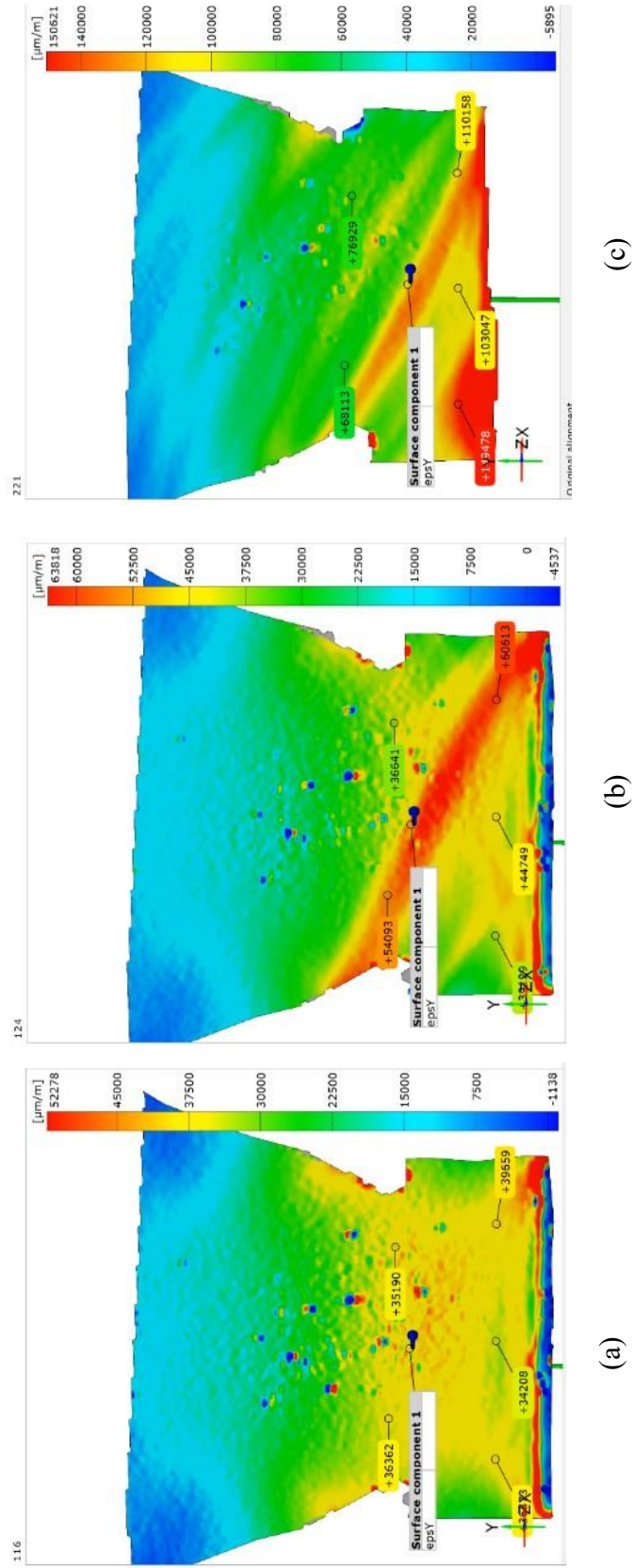


Figure 4.19: DIC results for specimen T3 (a) strain before the onset of serrations, (b) strain at the onset of the first serration, and (c) strain towards the end of the test.

4.2.1.3 Longitudinal Stiffener Specimen Results

Longitudinal Stiffener Specimens are composed of flat plate specimens with load bearing longitudinal stiffeners welded using continuous fillet welds. The main test plate is AA5083-H116 while the longitudinal stiffener is AA6061-T6511. The same 5183 weld filler was used. The elongation of the gauge length of the specimen was measured using two spring loaded LVDTs. One LVDT was mounted on the main plate while the other measured the elongation of the stiffener. In general, both LVDTs registered almost identical elongations during the tests. Their readings were averaged and used to represent the elongation of the specimens. The load-deformation curves of the three longitudinal stiffener specimens are shown in Figure 4.20. Figure 4.21 shows a close-up view of the failure surfaces of Specimen L2. Moreover, the post failure images for all three L specimens are seen in Figure 4.22. Table 4.8 shows the ultimate capacity and elongation at ultimate for the three longitudinal stiffener specimens.

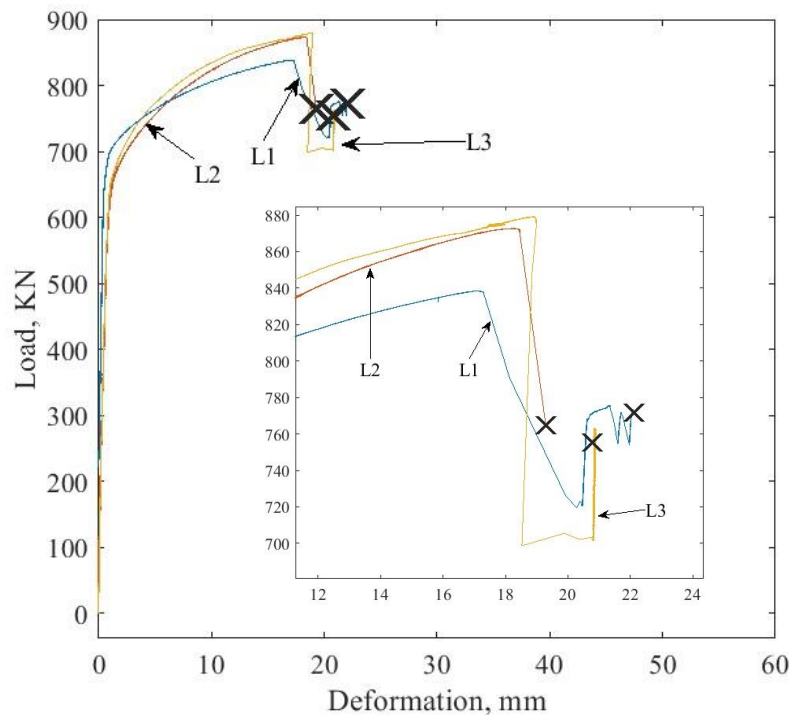


Figure 4.20: Load-deformation curves for all longitudinal stiffener specimens.

The three L specimens showed consistent behavior during these tests; however, this behavior was different than that of the F and T specimens. These L specimens gained forced up to the ultimate tensile strength, then a large drop in the force was observed. This sudden drop reached

200 KN (45 kips) in some cases. The specimen would fail shortly after this large drop without significant serration behavior. Low variability was observed in the ultimate tensile strength between the specimens with a COV of 2.8%. A notable observation is that these L specimens did not exhibit the high ductility observed in the flat plate specimens. The deformation capacity was approximately 40% of that accommodated by the flat plate specimen.

Table 4.8: Results of Longitudinal Stiffener Specimens

Specimen number	Ultimate force, KN (kip)	Ultimate elongation, mm (in)
L1	837 (188)	17.5 (0.69)
L2	877 (197)	19 (0.75)
L3	881 (198)	18 (0.71)

The DIC results for the three specimens are shown in Figure 4.23-4.25. The 3D field captured by the DIC system covered an entire quadrant showing the main test plate and longitudinal stiffener for Specimens L2 and L3; however, it only shows the main plate for Specimen L1. These results showed the formation of a single PLC band responsible for the large drop in force followed by the failure of the specimen. Although the AA6061-T6511 did not display a serration behavior in the ancillary testing, the DIC results depicted below showed that this PLC band propagated through the AA5083 main test plate, the AA6061 stiffener, and the weld line.

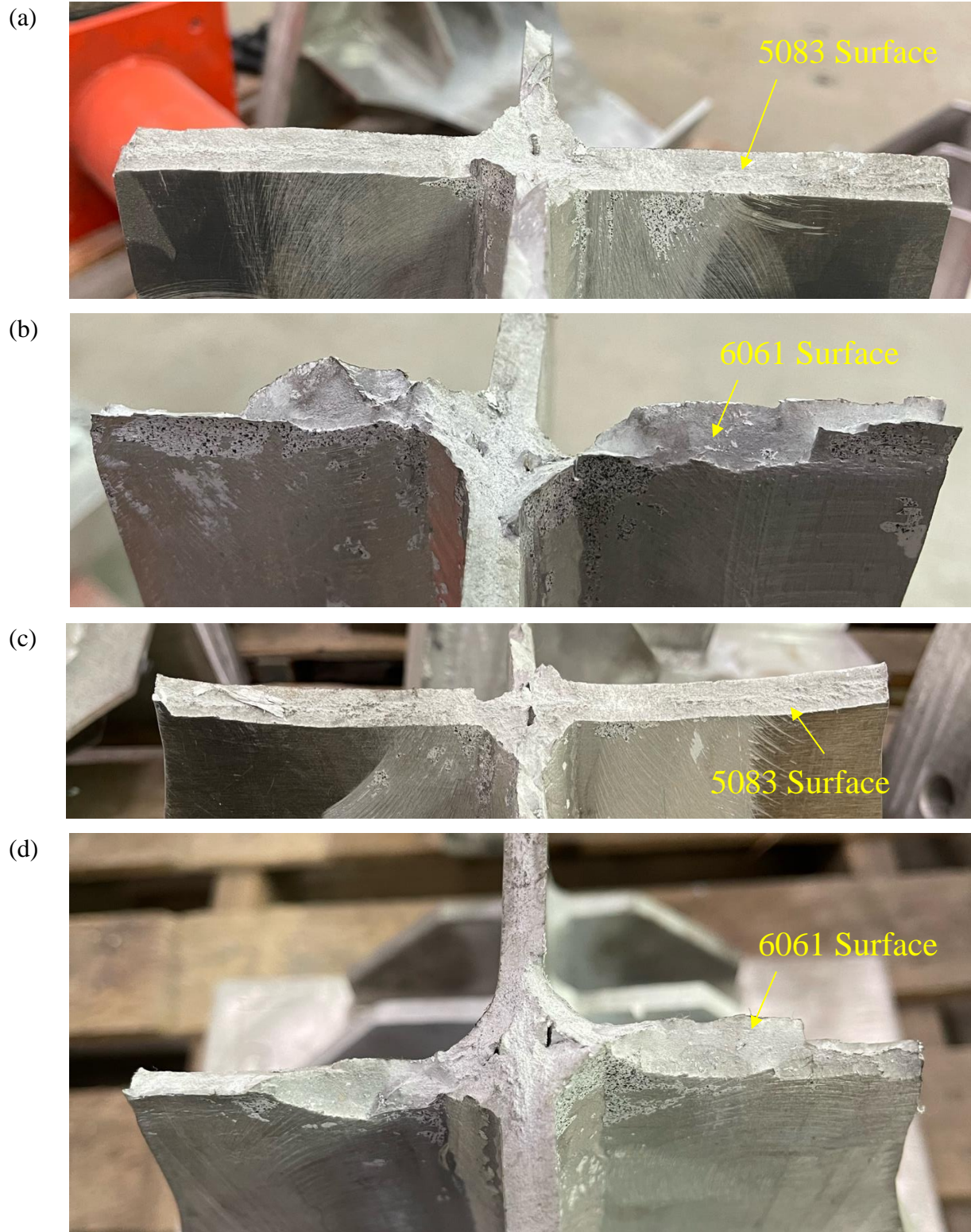


Figure 4.21 Failure surfaces of Specimen L2 (a) lower 5083 surface, (b) lower 6061 surface, (c) upper 5083 surface, and (d) upper 6061 surface.



(a)



(b)



(c)

Figure 4.22: Longitudinal stiffener specimen post failure (a) L1 (b) L2 (c) L3.

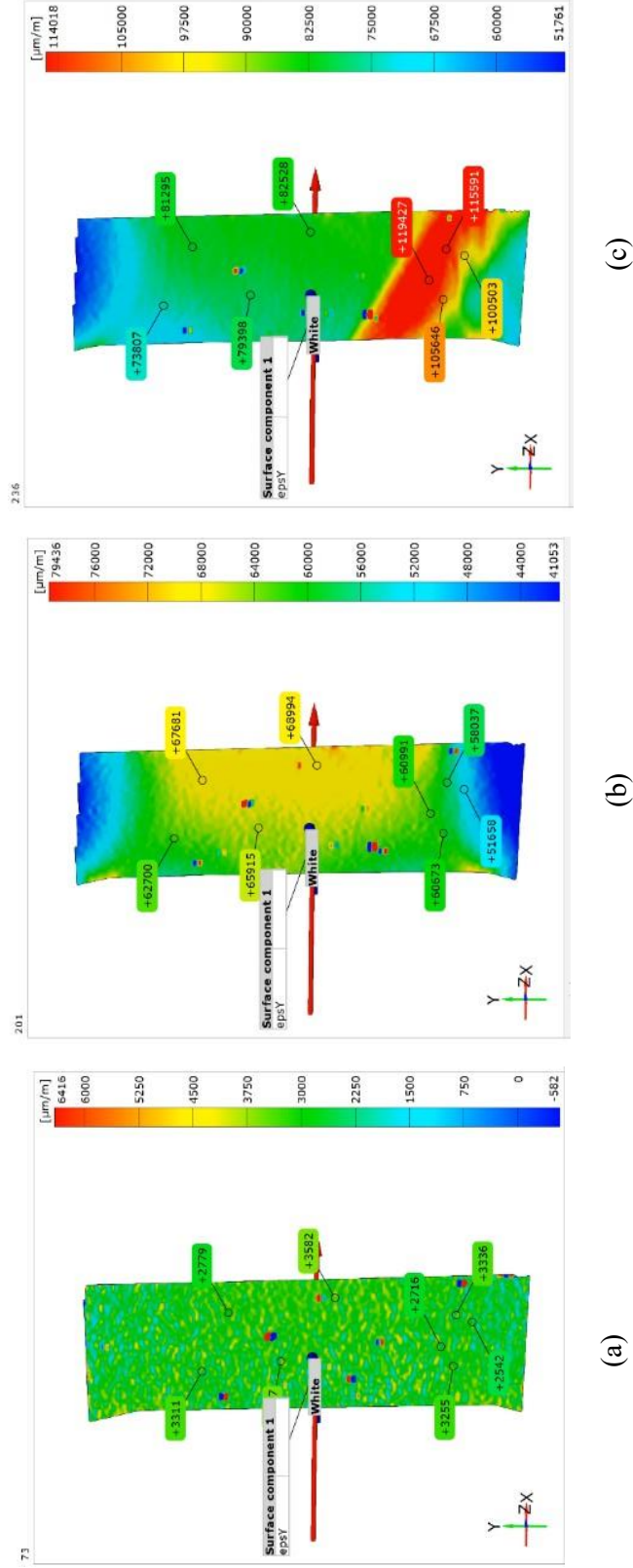


Figure 4.23: DIC results for specimen L1 (a) strain in the beginning of the test, (b) strain just before the onset of the first serration, and (c) strain after the single serration where the specimen failed shortly after. (The shown segment is the main test plate)

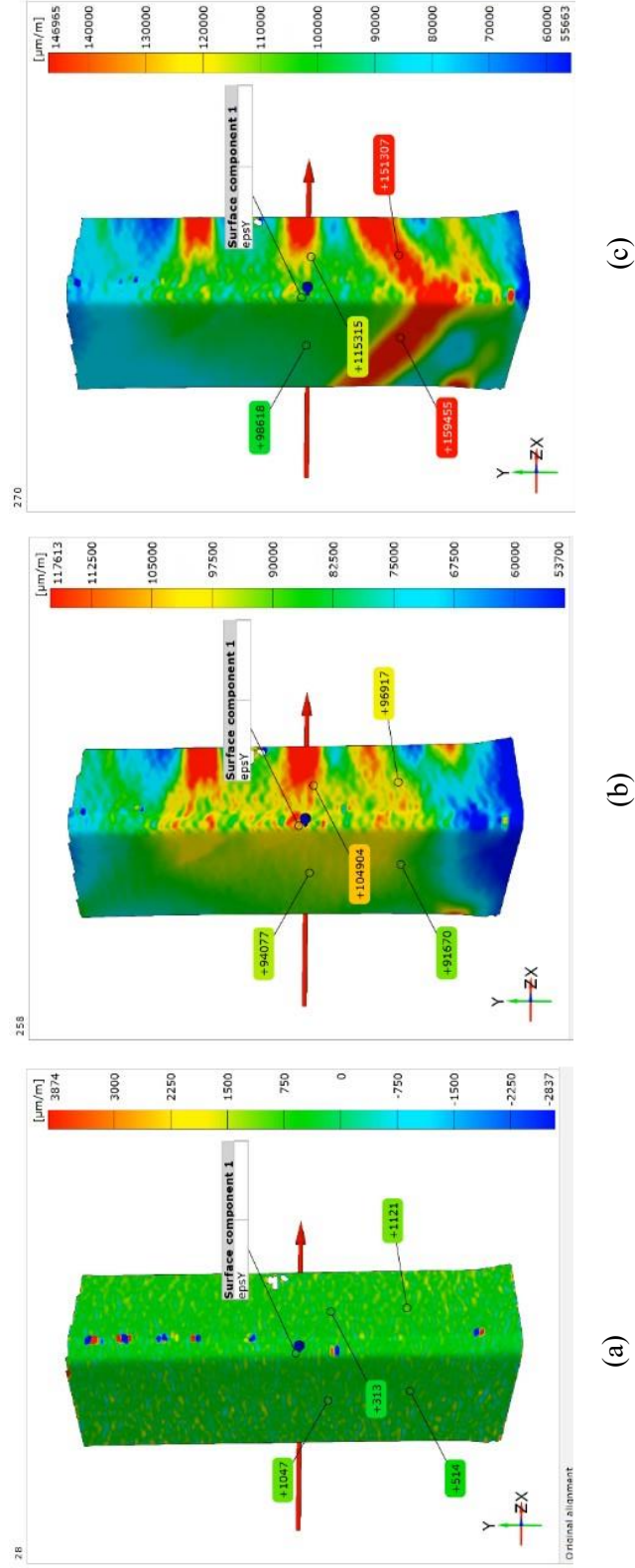


Figure 4.24: DIC results for specimen L2 (a) strain in the beginning of the test, (b) strain just before the onset of the first serration, and (c) strain after the single serration where the specimen failed shortly after. (Left segment is the main test plate and the right segment is the stiffener)

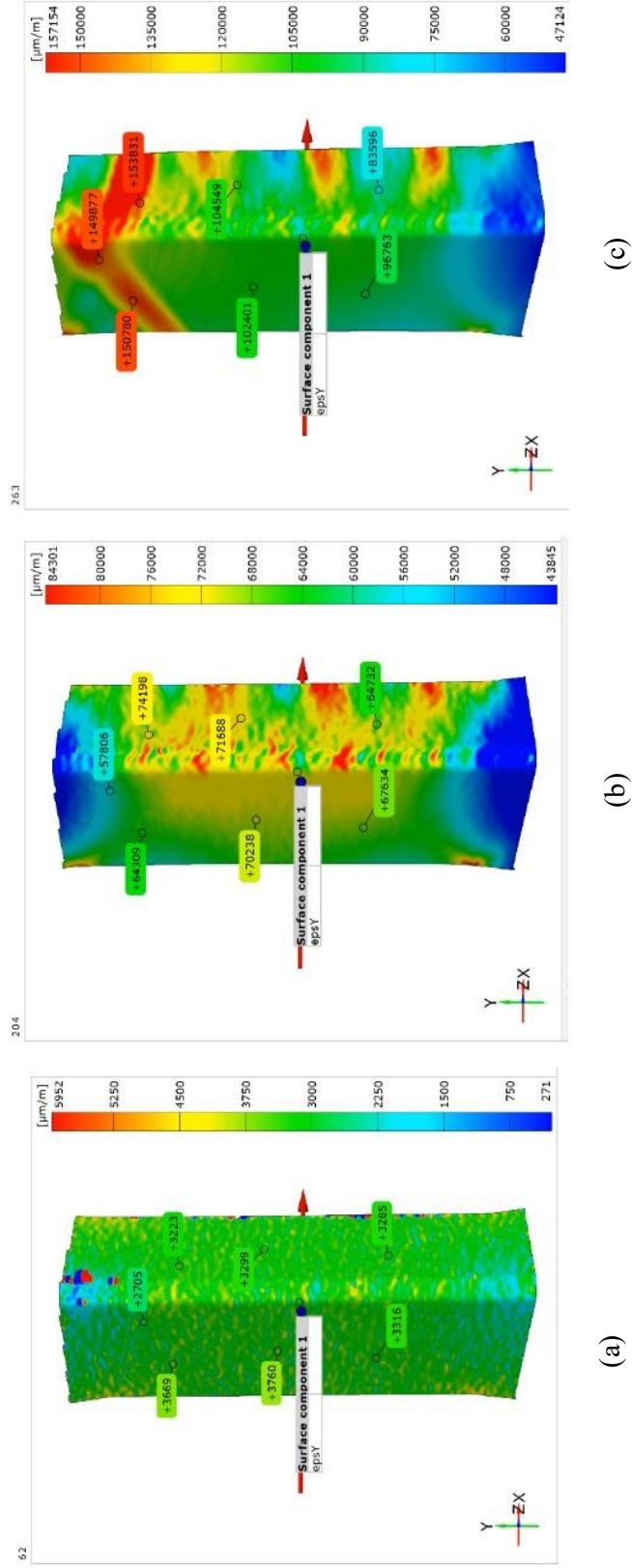


Figure 4.25: DIC results for specimen L3 (a) strain just before the onset of the first serration, and (c) strain after the single serration where the specimen failed shortly after. (Left segment is the main test plate and the right segment is the stiffener)

4.2.1.4 Longitudinal and Transverse Stiffener Specimen Results

The final set of specimens has two AA6061 longitudinal stiffeners and four AA6061 transverse stiffeners connected to the AA5083 main test plate using fillet welds. The elongation of the gauge length was measured using two spring loaded LVDTs. One LVDT was connected to the gauge length of the main test plate and the other was connected across the gauge length of the longitudinal stiffener. Again, both LVDTs registered almost identical readings; accordingly, their readings were averaged and used for data analysis. The load-deformation curves of the three LT specimens are shown in Figure 4.26, a close-up view of the fracture surface of Specimen LT2 is shown in Figure 4.27, and images of the fractured specimens are shown in Figure 4.28.

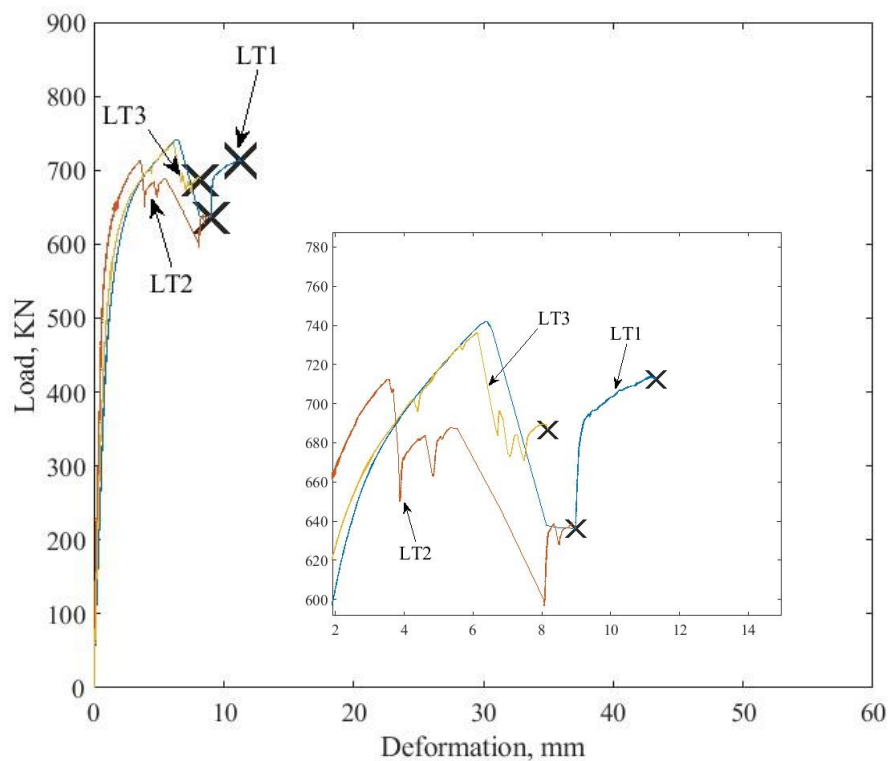
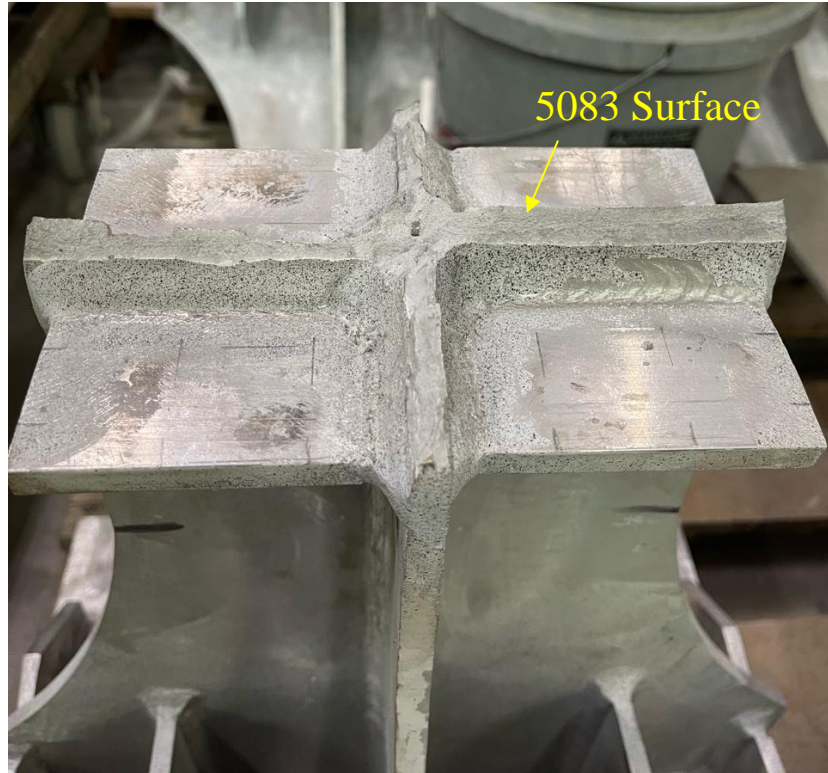


Figure 4.26: Load-deformation curves for all LT specimens.

(a)



(b)



Figure 4.27 Lower failure surface of Specimen LT2 with focus are covering: (a) the AA5083 failure surface and (b) the AA8061 surface



(a)



(b)



(c)

Figure 4.28: Longitudinal and transverse stiffener specimen post failure (a) LT1, (b) LT2, and (c) LT3.

The results from the three specimens showed consistency in terms of the ultimate tensile strength and the failure mechanism. However, the elongation at fracture from these specimens was the lowest of all the other specimen configurations. The average elongation at fracture was 9.5 mm (0.37-in) which represents only 4.6% elongation of the gauge length. In addition, the average elongation at ultimate load was only 5.36 mm (0.21-in). Another notable difference is related to the behavior of the welded AA6061-T6511 longitudinal stiffeners. In these tests, it was observed that the AA6061 longitudinal stiffeners exhibited a ductile necking in their HAZ prior to the global fracture of the specimen. In some cases, these stiffeners would fracture completely before the failure of the AA5083 main plate. This necking behavior can be seen in Figure 4.29. As also shown in Figure 4.28, Specimen LT3 failed in the upper side of the transverse stiffener, while the bottom side showed fracture and/or necking, indicating that the failure is governed by the behavior of the main test plate in this specimen. This is due to the high strength of the HAZ of the AA5083 compared to that of welded AA6061.

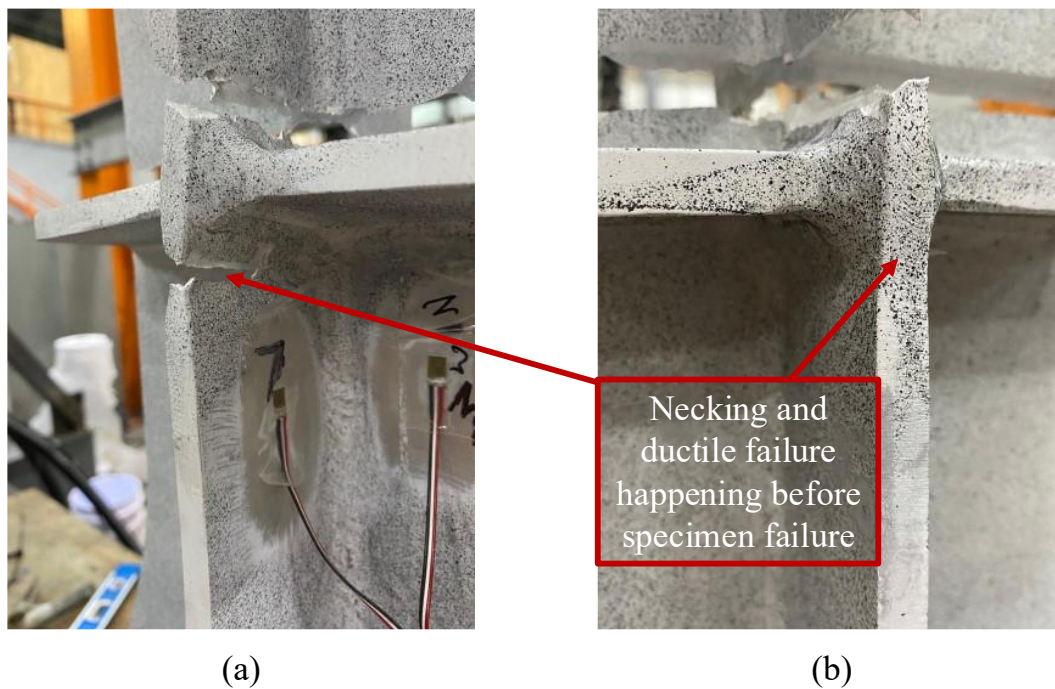


Figure 4.29: Failure of the LT specimen (a) fracture of the longitudinal stiffener and (b) necking of the stiffener on the other side of the fracture location.

In addition, the DIC results for the three specimens are also shown in Figure 4.30-4.32. Figures 4.30 and 4.31 show the upper left quadrant of the specimen and cover both the main plate and longitudinal stiffener. In Figure 4.32, attempts were made to capture the strain above and

below the transverse stiffener. However, the DIC results were dominated by the necking in the AA6061 longitudinal stiffener below the transverse stiffener. The white regions in Figure 4.32 represent the location of the transverse stiffener. As seen from the DIC results, these specimens did not show the PLC-driven behavior experienced by the L or T specimens. However, high strain localizations occurred within the HAZ in both segments. The DIC results of Specimen LT3 show the ductile necking of the longitudinal stiffener. Table 4.9 shows the ultimate capacity and ultimate elongation for the three longitudinal and transverse stiffener specimens.

Table 4.9: Results of Longitudinal and Transverse Stiffener Specimens

Specimen number	Ultimate force, KN (kip)	Ultimate elongation, mm (in)
LT1	743 (167)	6.4 (0.25)
LT2	717 (161)	6.2 (0.24)
LT3	739 (166)	3.5 (0.14)

The experimental testing was concluded on the 16th of June 2023 after testing the twelve large-scale aluminum specimens. Detailed finite element analysis is presented next to aid in understanding the behavior of these specimens.

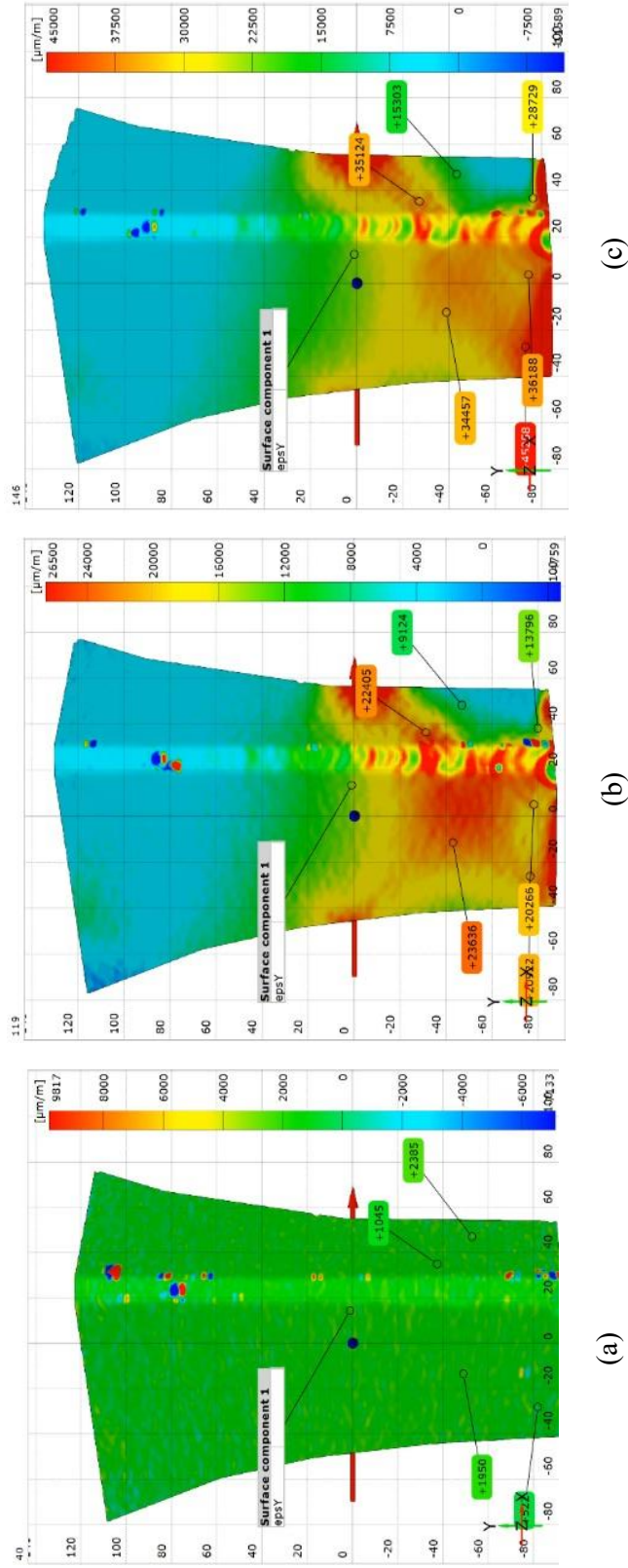


Figure 4.30: DIC results of specimen LT 1 (a) strain before the end of the test, (b) strain in the beginning of the test, and (c) strain in the middle of the test, and the right segment is the stiffener.

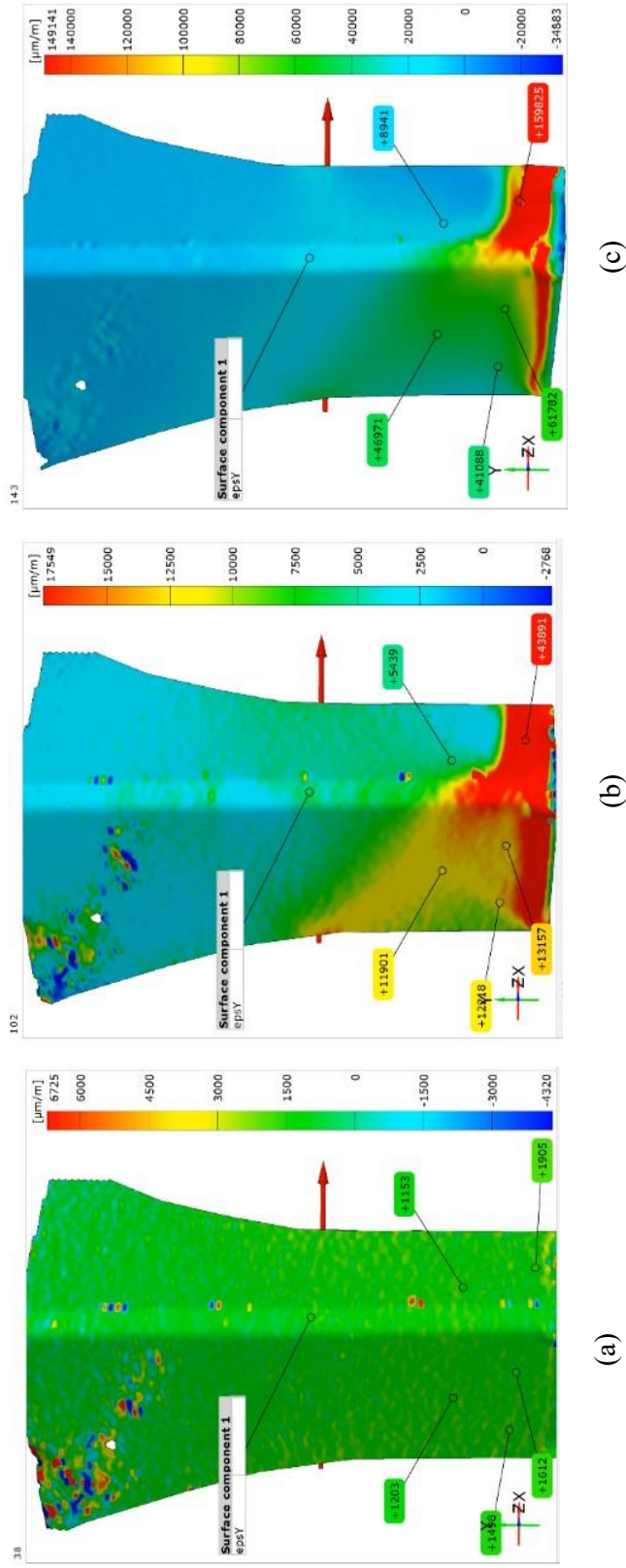


Figure 4.31: DIC results of specimen LT 2 (a) strain before the end of the test, (b) strain in the beginning of the test, and (c) strain in the middle of the test. (Left segment is the main test plate and the right segment is the stiffener)

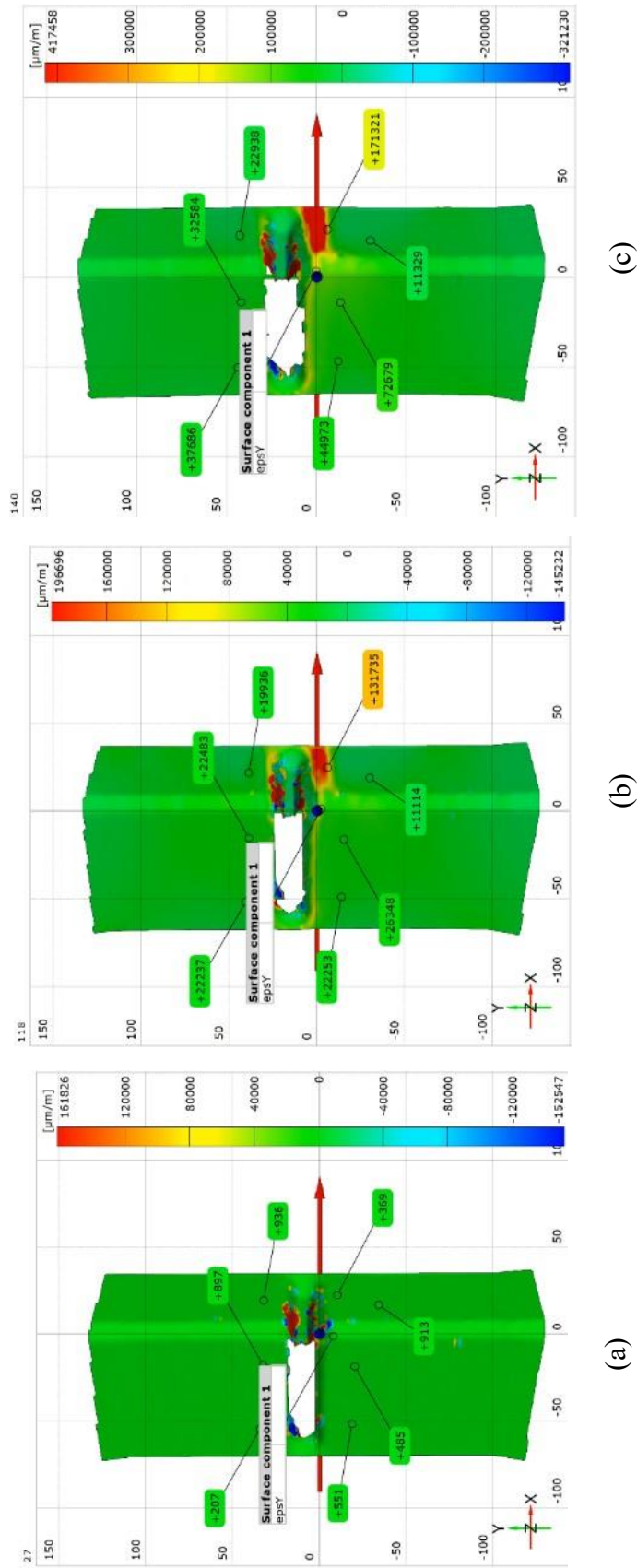


Figure 4.32: DIC results of specimen LT 3 (a) strain in the middle of the test, and (c) strain before the end of the test. (Left segment is the main test plate and the right segment is the stiffener)

5 FINITE ELEMENT MODELLING

Detailed finite element analysis was conducted in ABAQUS environment using version 2020 of the software to simulate the large-scale samples and develop a deeper understanding of the behavior.

5.1 MODEL GEOMETRY

Four finite element models were created to represent the different specimen types covered in the large-scale testing. The entire specimen was modeled in the FE software including the aluminum end plates, main test plate, connection stiffeners, longitudinal stiffeners (if applicable), weld lines (if applicable), and transverse stiffeners (if applicable). Figures 5.1-5.4 show the FE models corresponding to each of the four specimens.

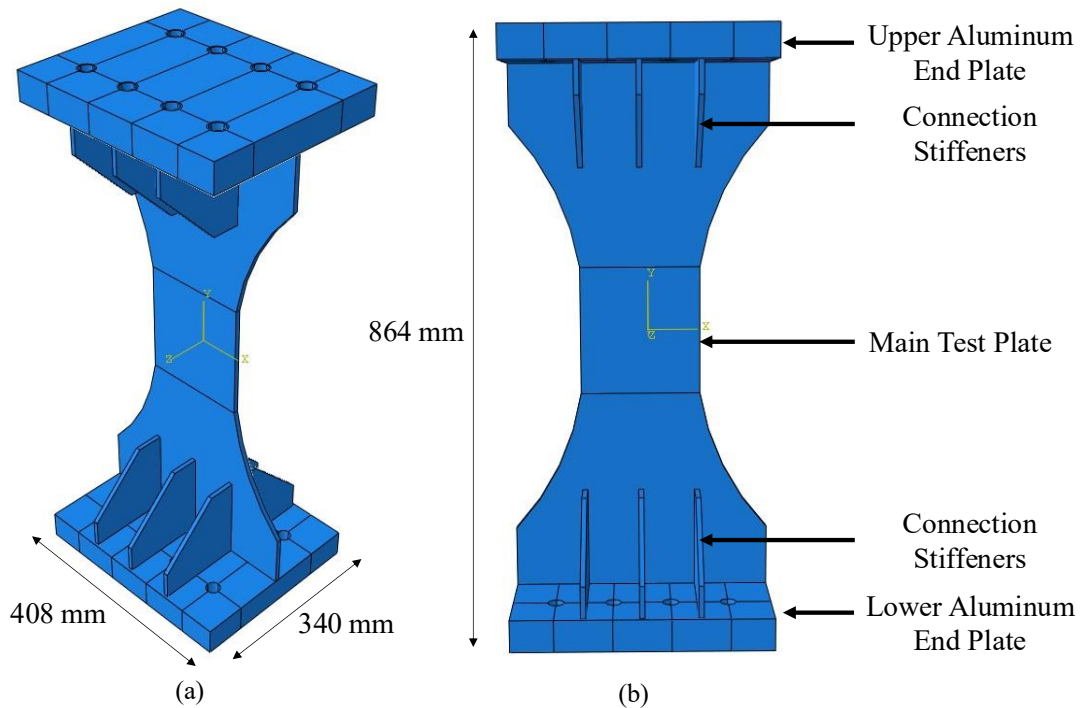


Figure 5.1: Model geometry of the F specimen (a) 3D view of the FE model, (b) different components in the FE model.

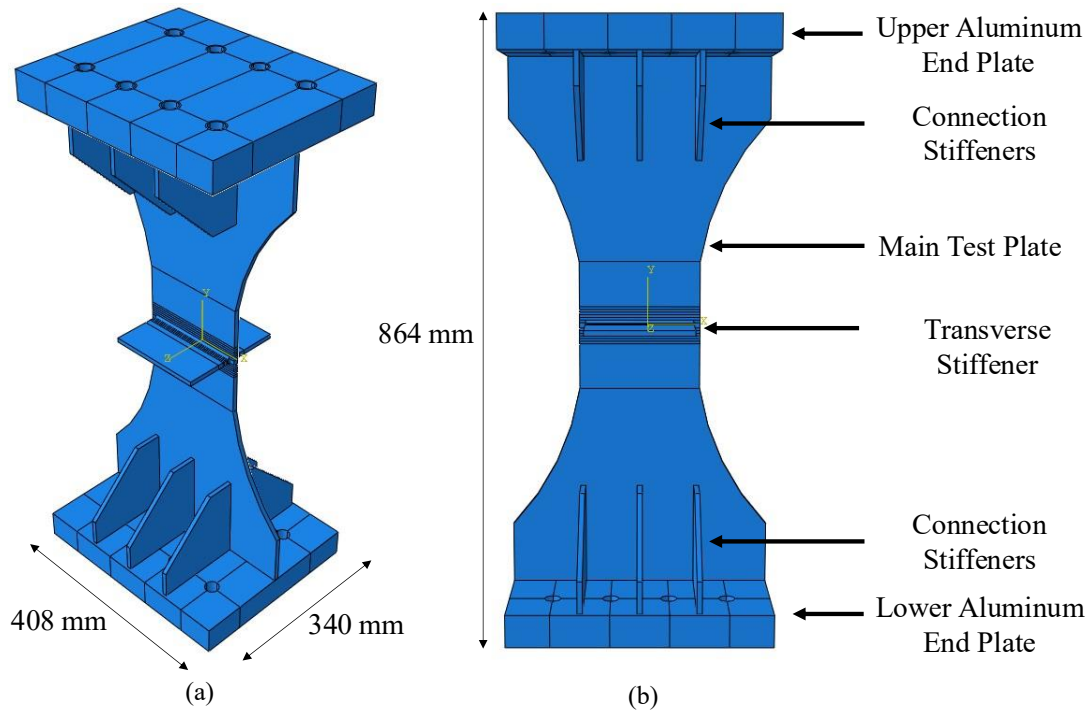


Figure 5.2: Model geometry of the T specimen (a) 3D view of the FE model, (b) different components in the FE model.

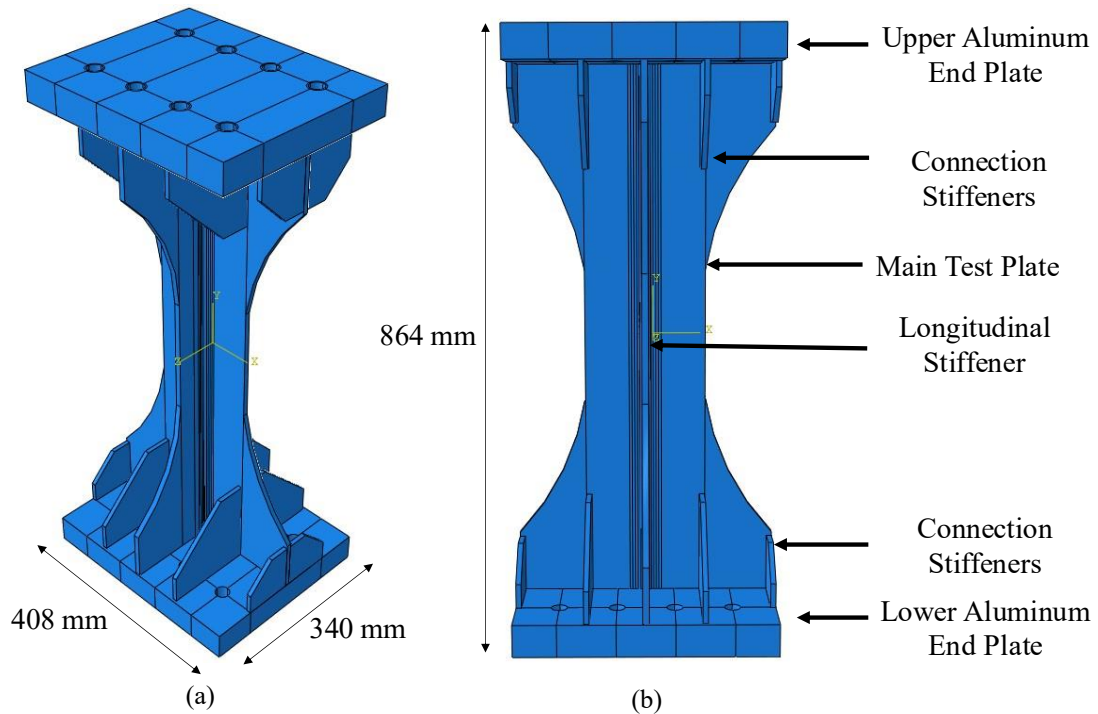


Figure 5.3: Model geometry of the L specimen (a) 3D view of the FE model, (b) different components in the FE model.

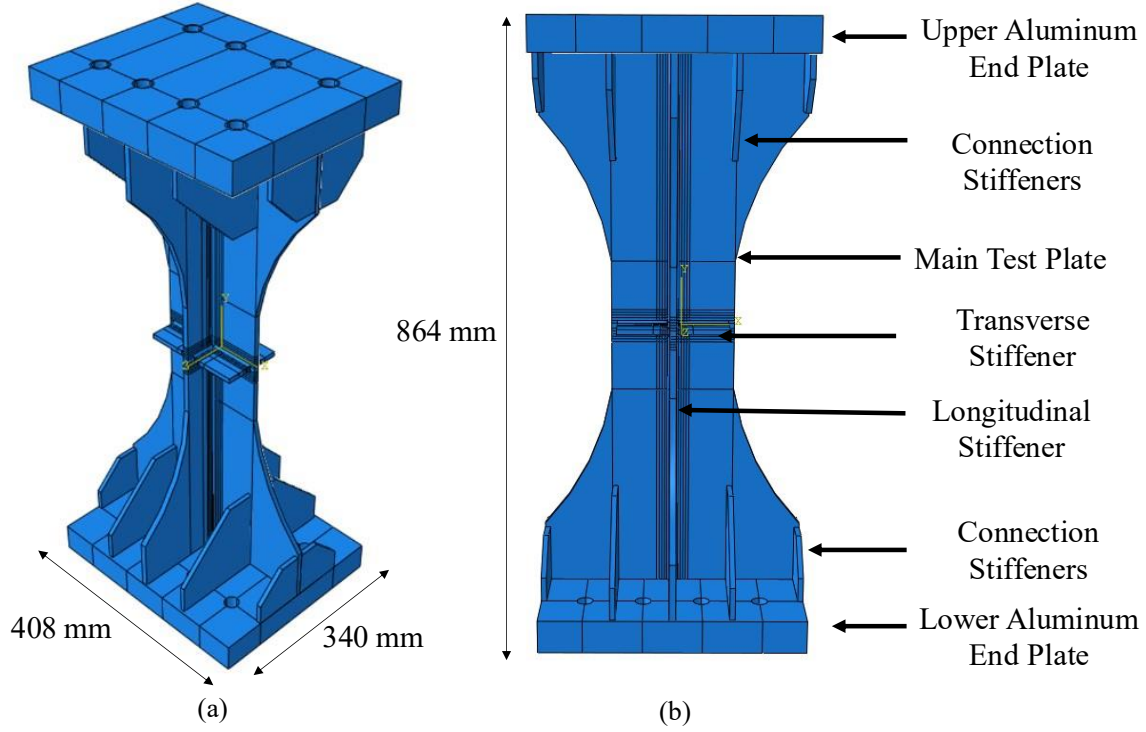


Figure 5.4: Model geometry of the LT specimen (a) 3D view of the FE model, (b) different components in the FE model.

5.2 MATERIAL MODELING

5.2.1 Aluminum Stress-Strain Behavior

The Ramberg-Osgood material model was used to model the stress-strain behavior of the HAZ and BM of different aluminum alloys. The original Ramberg-Osgood model (Ramberg & Osgood, 1943) defines the stress-strain behavior only up to the yield point of the material. Yun et al. (2021) proposed a two-stage Ramberg-Osgood model with the first stage representing the behavior up to the yield while the second stage from the yield up to the ultimate strength. In this model, the strain is expressed as:

$$\varepsilon = \left(\frac{\sigma}{E}\right) + \left(0.002 * \left(\frac{\sigma}{\sigma_{0.2}}\right)^n\right), \text{ for } 0 < \sigma \leq \sigma_y \quad (4)$$

$$\varepsilon = \left(\frac{\sigma - \sigma_y}{E_{0.2}}\right) + \left(\left(\varepsilon_u - \varepsilon_{0.2} - \frac{\sigma_u - \sigma_y}{E_{0.2}}\right) * \left(\frac{\sigma - \sigma_y}{\sigma_u - \sigma_y}\right)^m\right), \text{ for } \sigma_y < \sigma \leq \sigma_u \quad (5)$$

$$E_{0.2} = \frac{E}{1 + \left(0.002 * n * \frac{E}{\sigma_y}\right)}$$

where ε is the strain, σ is the stress, and E is the Elastic Modulus. The $\sigma_{0.2}$ is the 0.2% offset proof stress and n is the Ramberg-Osgood exponent. The ε_u is the ultimate strain, $\varepsilon_{0.2}$ is the 0.2% offset proof strain, and m is the strain hardening exponent. The σ_u is the ultimate stress, σ_y is the yield stress, and $E_{0.2}$ is the 0.2% offset elastic modulus. Figure 5.5 shows the modified Ramberg-Osgood model compared to experimental stress-strain curves reported in Yun et al. (2021).

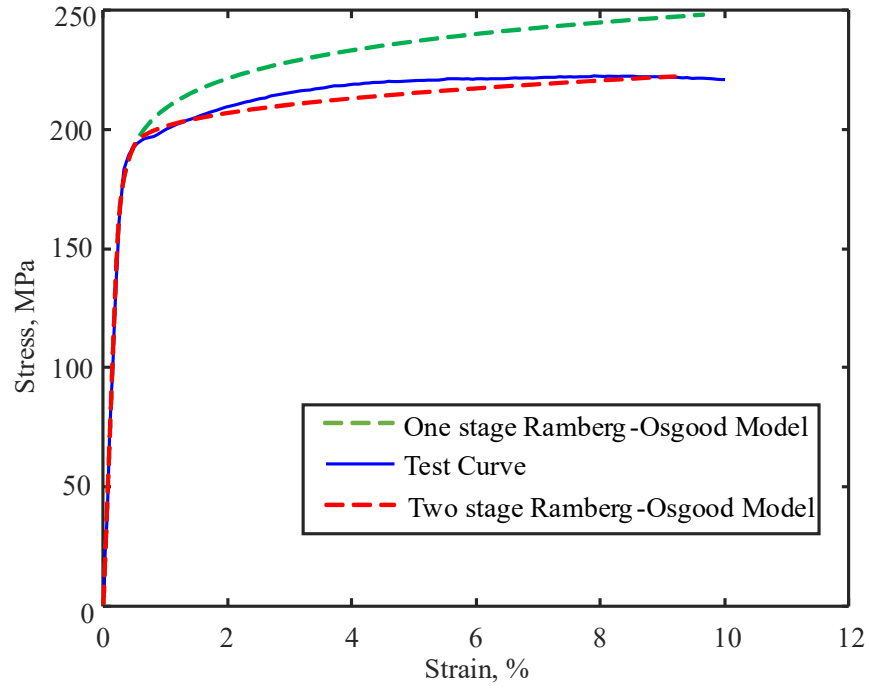


Figure 5.5: Comparison between the original and modified Ramberg-Osgood model vs the experimental profile reported in Yun et al. (2021).

To properly capture the behavior of the weld lines, BM, and the different regions within the HAZ of both materials, fifteen separate material models were created to be used in the finite element models. A Microsoft Excel script was used to obtain the Ramberg-Osgood exponent, n , and the strain hardening exponent, m , of the different materials based on the ancillary testing results reported in Section 4.1. An optimization problem utilizing the Generalized Reduced Gradient algorithm (Lasdon et al., 1978) was formulated to establish the optimum value of these parameters that minimizes the error between the experimental stress-strain curve and that resulting from the modified Ramberg-Osgood (MRO) model. These fifteen material models included the

BM of AA5083-H116, BM of AA6061-T6511, six regions of HAZ of AA5083-H116, six regions of HAZ of AA6061-T6611, and the weld metal 5183. Table 5.1 shows the obtained Ramberg-Osgood model parameters for each material model. The table also shows the yield stress and modulus of elasticity for each material.

Table 5.1: Modified Ramberg-Osgood model parameters.

Material	Specimen Type	Ramberg-Osgood Exponent, n	Strain Hardening Exponent, m	Yield Stress $\sigma_{0.2}$, MPa (ksi)	Young's Modulus E , MPa (ksi)
AA5083-H116	Base Metal	60.42	13.26	235 (34.1)	66481 (9643)
	HAZ - 4 mm	39.5	16.27	116 (16.8)	54651 (7927)
	HAZ - 8 mm	43.65	18.76	159 (23.1)	31461 (4564)
	HAZ - 12 mm	44.85	22.95	162 (23.5)	28873 (4187)
	HAZ - 16 mm	43.37	18.27	186 (27)	138100 (20030)
	HAZ - 19 mm	77.82	21.12	236 (34.3)	44280 (6423)
	HAZ - 23 mm	55.74	10.96	216 (31.3)	65352 (9479)
AA6061-T6	Base Metal	266	17.43	276 (40)	81989 (11892)
	HAZ - 4 mm	86.67	8.35	170 (25)	74139 (10753)
	HAZ - 8 mm	33.83	5.01	121 (17.5)	34475 (5000)
	HAZ - 12 mm	54.46	8.3	159 (23.1)	19296 (2799)
	HAZ - 15 mm	124.25	10.25	237 (34.5)	32470 (4710)
	HAZ - 19 mm	179.4	10.5	267 (38.7)	41296 (5990)
	HAZ - 23 mm	182	12.3	265 (38.4)	67641 (9810)
AA5183	Weld Metal	27.58	5.88	106 (15.4)	20412 (2961)

5.2.2 Ductile Damage Model

A ductile damage model was used to simulate the ductile failure of the specimens. It was utilized in many studies including Askariani and Garivani (2020) and (Askariani et al., 2020) to predict damage initiation and evolution in numerical models. Damage initiation and damage evolution are the two main aspects included in the model. The damage initiation criterion is defined based on the equivalent plastic strain at fracture which is a function of stress triaxiality. Rice and Tracey (1969) calculated the equivalent plastic strain at fracture as

$$\varepsilon_{eq_o} = \alpha \times \exp(-1.5\eta) \quad (6)$$

where α is a material parameter; η is stress triaxiality, defined as σ_m/σ_{eq} ; σ_m , σ_{eq} are the mean normal (hydrostatic) and equivalent stresses, respectively. Once the condition represented in Equation 7 is satisfied the damage initiation criterion is activated.

$$DI = \int_0^{\varepsilon_{eq_o}} \frac{d\varepsilon_{eq}}{\varepsilon_{eq_o}(\eta)} = 1 \quad (7)$$

where DI is the damage indicator ranging from 0 to 1; ε_{eq} is the equivalent plastic strain.

The element starts to degrade and accumulate damage once the damage initiation criterion is reached. The damage evolution resembles the rate of degradation for the elements during the damage accumulation process. With the evolution of damage, the stiffness of the element starts to decrease resembling the damage level of the element. Figure 5.6 shows, conceptually, the damage initiation and evolution.

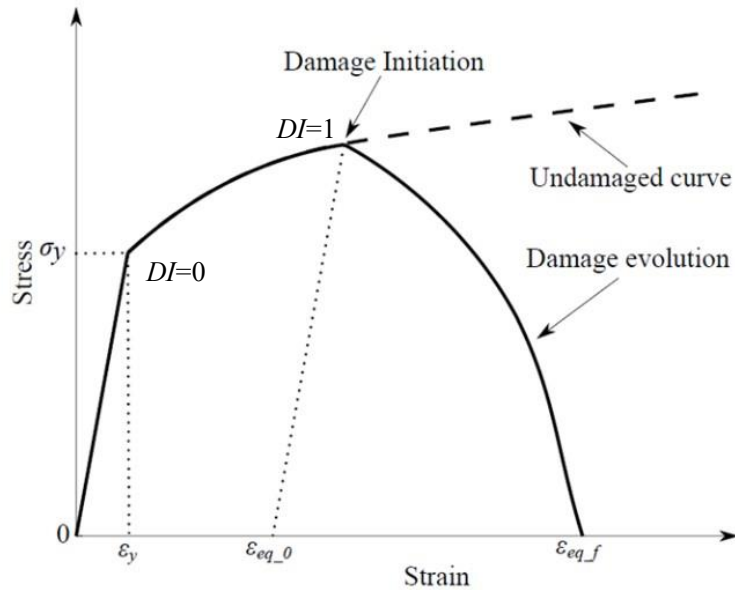


Figure 5.6: Illustrative figure for the Ductile Damage Model.

5.3 OTHER MODEL ATTRIBUTES

The eight noded (C3D8R) solid element was used to mesh all components of the model. Solid elements were used for their ability to model fillet welds which may not be possible if shell elements were to be used. Figure 5.7 shows the mesh orientation for different parts of the model. Tie constraints were used to connect the stiffening brackets to the end plate and the main test plate in all finite element models. They were utilized, in lieu of modeling the weld lines at the

connection, to help reduce the computational time. Figure 5.8 provides an illustration of the tie constraints in one of the finite element models. Variation in the mechanical properties across the HAZ has been incorporated by modeling each region of the HAZ separately within the model. The different plates were partitioned as seen in Figure 5.9, each partition having its own stress-strain behavior as defined in Table 5.1. The HAZ was considered to extend to 25 mm from both sides of a weld line. This technique has been presented in Sensharma et al. (2011) and later adopted in Collette (2022).

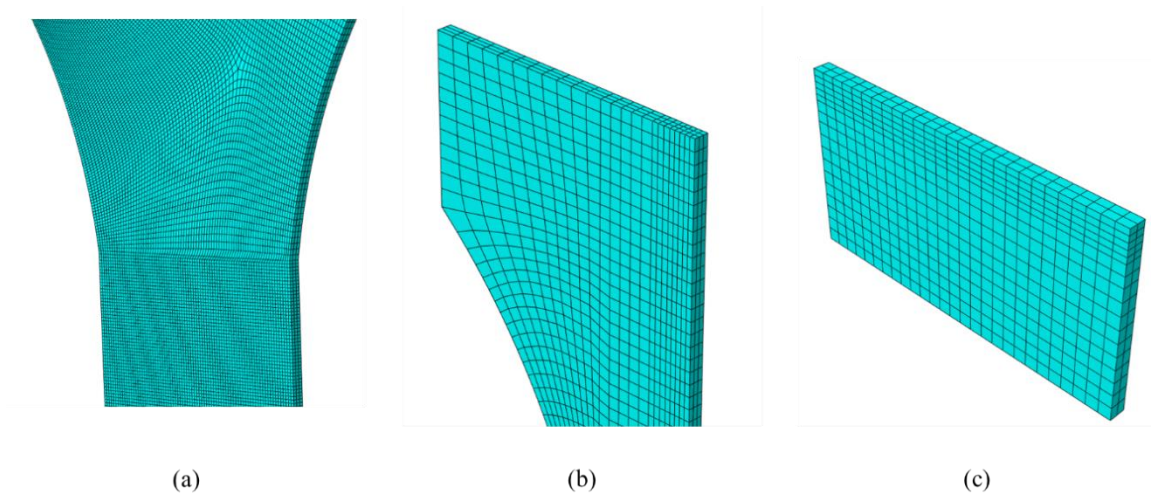


Figure 5.7: Meshing of different model components: (a) mesh orientation of the main test plate, (b) mesh orientation of the longitudinal stiffener, and (c) mesh orientation of the transverse stiffener found in T specimens.

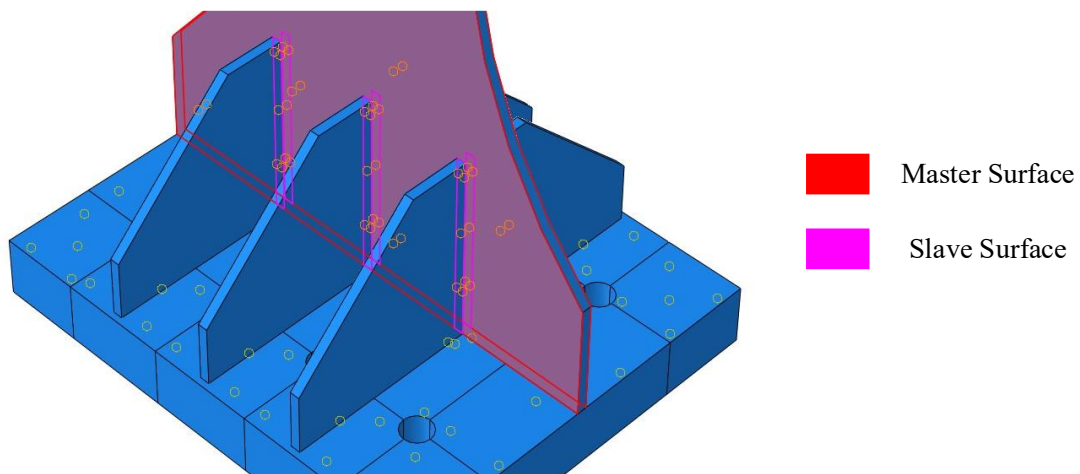


Figure 5.8: Tie constraint between connection stiffeners and main test plate.

The master and slave surfaces represent surfaces engaged in a contact interaction in ABAQUS. They represent the tie constraints where the master and slave surface will act as one unit in terms of displacement and will allow force transfer without the need for weld lines.

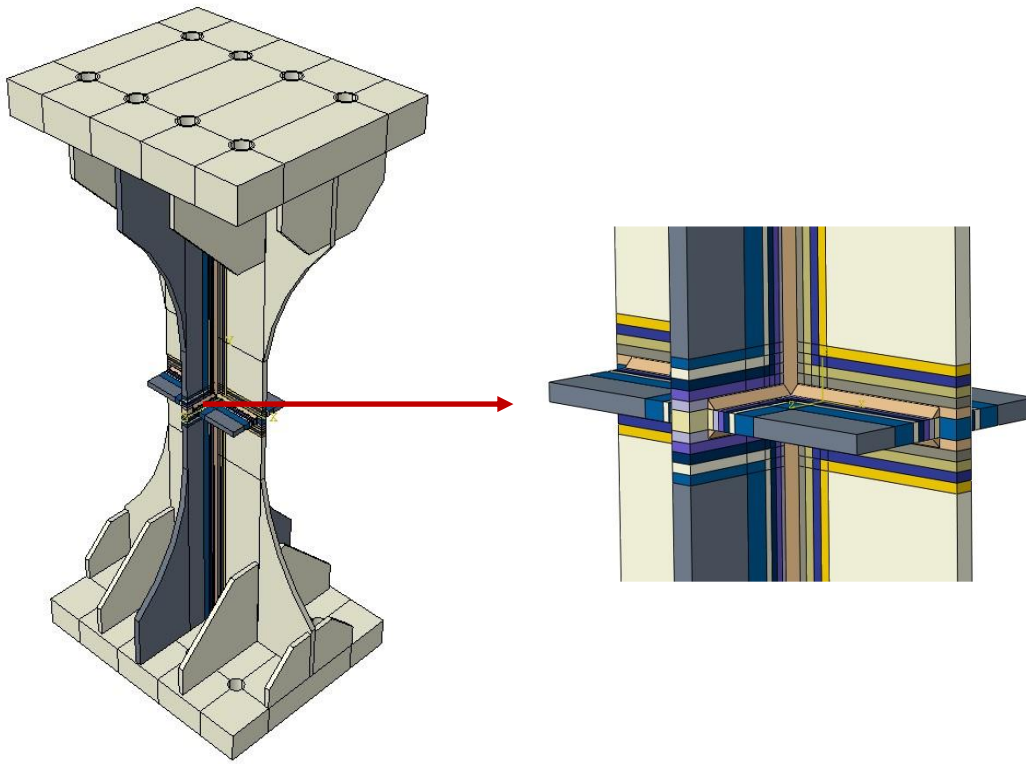


Figure 5.9: Close-up view on the HAZ sectioning in the LT specimen FE model.

The weld lines between the longitudinal and/or transverse stiffener and main plate were included in the finite element models to represent the actual load path that exists in the welded connection. The weld lines utilized a tie constrained between the weld leg and plate surfaces. Figure 5.10 shows the close-up view of the weld lines within the FE model of the specimen with the longitudinal and transverse stiffener. To apply the load, the bottom surface of the lower aluminum end plate was defined as a fixed support, while an upward displacement was applied at the top of the upper aluminum end plate. To further simulate the loading technique from the experimental testing, the

displacement on the specimen was applied at the end plate bolt holes. Figure 5.11 shows the specimen with the load (i.e., displacement) and boundary conditions applied.

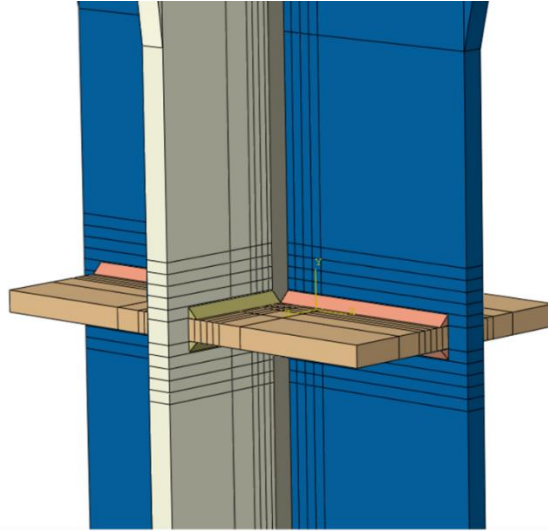


Figure 5.10: Close-up view on the weld lines used to connect the different parts in the LT specimen FE model.

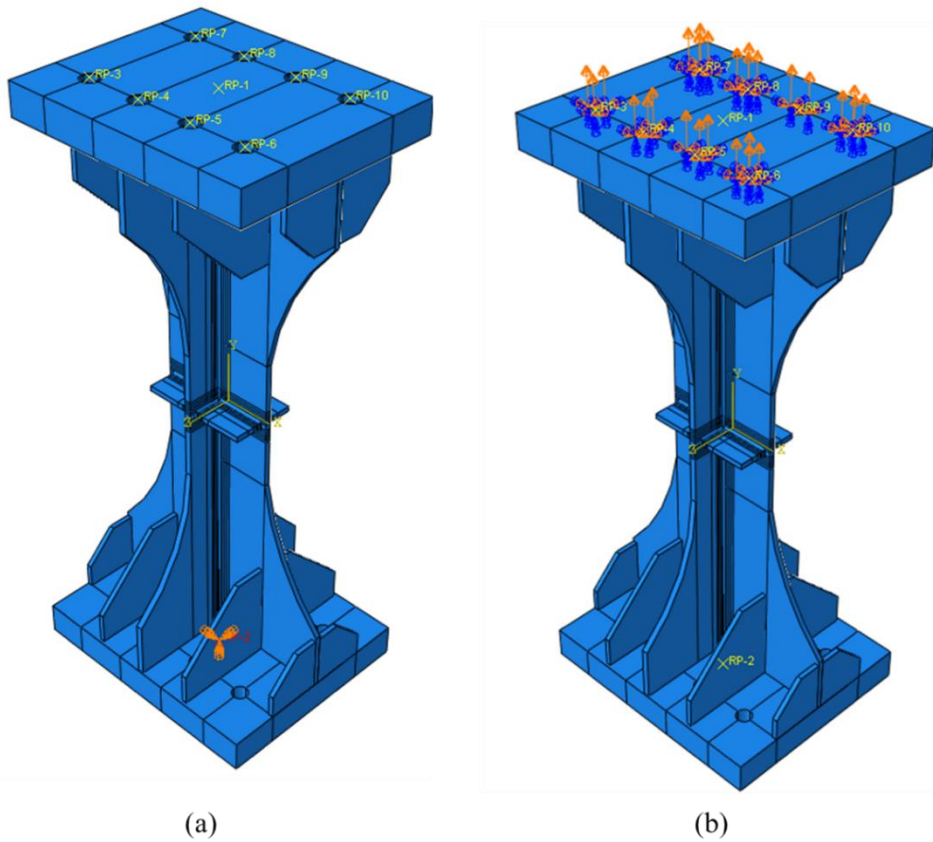


Figure 5.11: Boundary conditions across all FE models (a) bottom fixed support at the lower aluminum end plate, and (b) displacement applied from the upper aluminum end plate.

Residual stresses that arise from the welding process were included in the FE model of the T and L specimens. Based on (Li et al., 2018), tensile residual stresses reaching the yield stress of the alloy were applied to the HAZ of the welded connection in the Y-direction, while compressive residual stresses were applied at the remaining parts of the specimen to ensure force equilibrium. Residual Stresses were applied as predefined fields of uniform stresses in the FEM whether they were tensile or compressive residual stresses. Figure 5.12 shows the applied residual stresses in Specimen L.

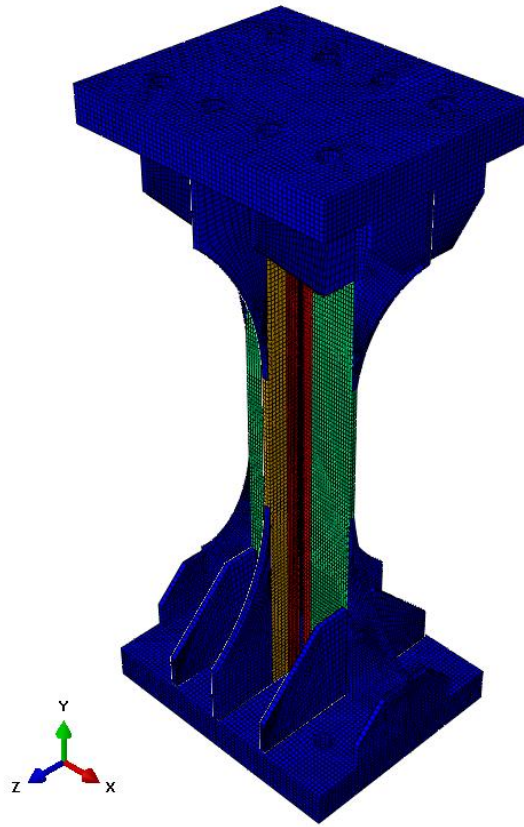


Figure 5.12: Predefined fields of residual stresses in L Specimen FE model.

The dynamic explicit solver offered by ABAQUS version 2020 was used to analyze the models. To ensure that the simulation represents a quasi-static condition, the kinematic energy of the system was controlled by choosing the rate of loading that induces the lowest value of kinematic energy compared to the internal energy in the system. Multiple iterations were conducted to optimize the loading rate that would minimize the kinematic energy and maintain a feasible computation time. Figure 5.13 shows the internal energy compared to the kinematic energy in one of the finite element models.

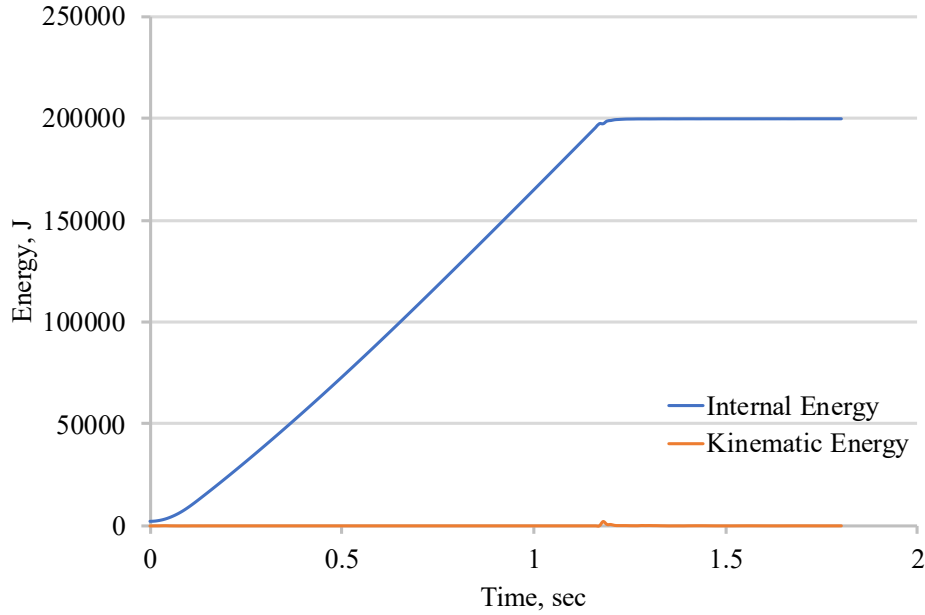


Figure 5.13: Internal and kinematic energy on one of the finite element models.

5.4 FINITE ELEMENT MODELLING RESULTS

The results from the four finite element models are presented below. In general, the FE results are in good agreement with the experimental results in terms of the ultimate force and deformation. Figure 5.14 shows the FE-generated load-deformation curve of the flat plate specimen when compared to the respective experimental results while Figure 5.15 shows the specimen after failure in the FE model. As seen in Figure 5.14, the ultimate strength and elastic stiffness agreed well with the experimental counterparts, while the fracture strain seems to align with the lower bound of the test results. This is mainly because the material model utilized in the FE analysis was derived based on the ancillary test coupons, which displayed a different serration behavior compared to the large-scale samples. Accordingly, the utilized material model may not properly simulate the plastic behavior at large elongations since this regime is largely influenced by the formation of the PLC bands. This was also evident in the 45 degrees failure mode that was seen in Figure 5.15. Since the serrations do not exist in the model, the stress concentrations and the brittle fracture were not properly captured in the FE models. Nevertheless, the FE prediction error of the ultimate strength is 0.8% while for the fracture deformation it is 11%.

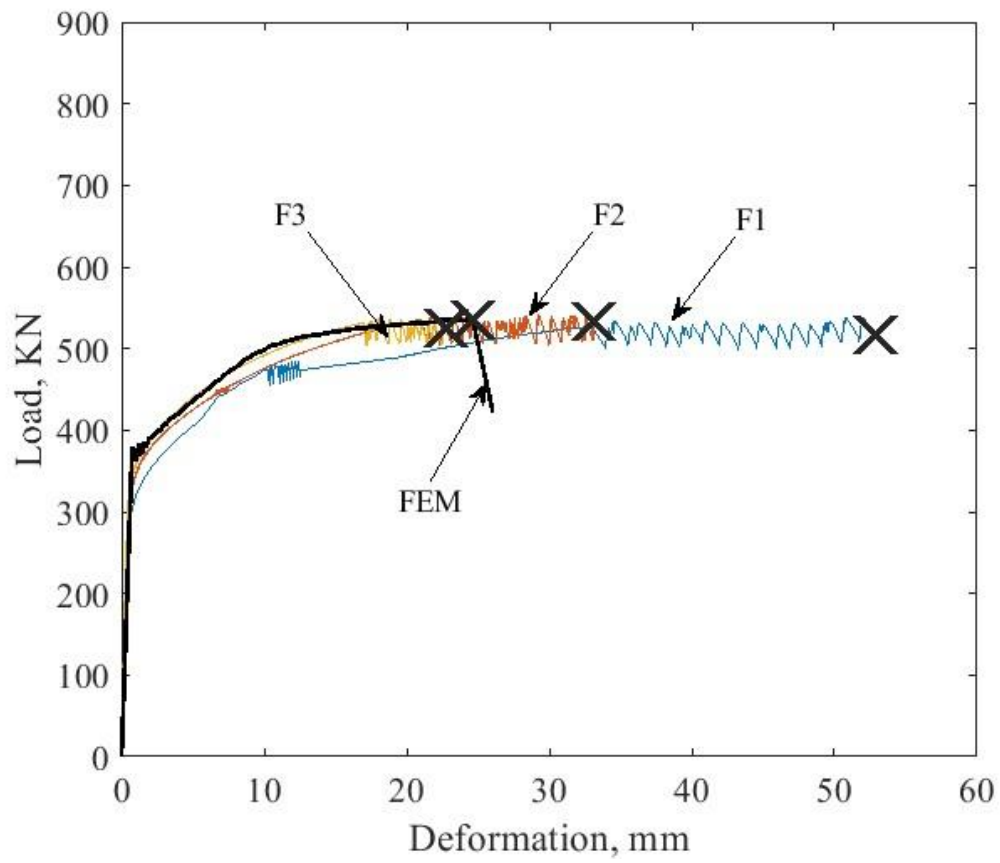


Figure 5.14: Finite element model results for flat plate specimens.

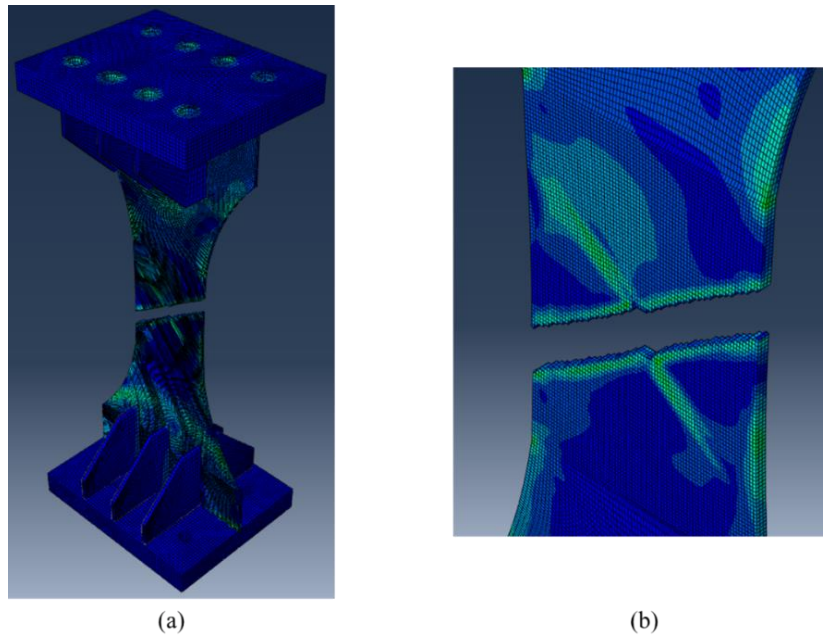


Figure 5.15: Behavior of flat plate specimen FE model (a) overall failure and (b) close-up view on the failure.

Figure 5.16 and Figure 5.17 show the load deformation curves and failure of the transverse stiffener specimen finite element model, respectively. The load-deformation results for the transverse stiffener specimen properly reflected the behavior of the experimentally tested specimen; however, the FE prediction error in the ultimate strength is 6% while for the fracture deformation is 35%, which are higher than those seen in the model of the F specimens. The FE predicted lower elongation at fracture compared to the experimental counterpart. Note that the model does not account for the occurrence of the PLC bands in the large-scale specimens which are the main mechanism to accommodate the plastic deformation in specimens F and T. The model was able to capture the location of the failure within the experimental specimens. As seen in Figure 5.17, the failure in the actual specimens occurred at the fillet weld toe within the HAZ, which was also the location of failure in the FE model.

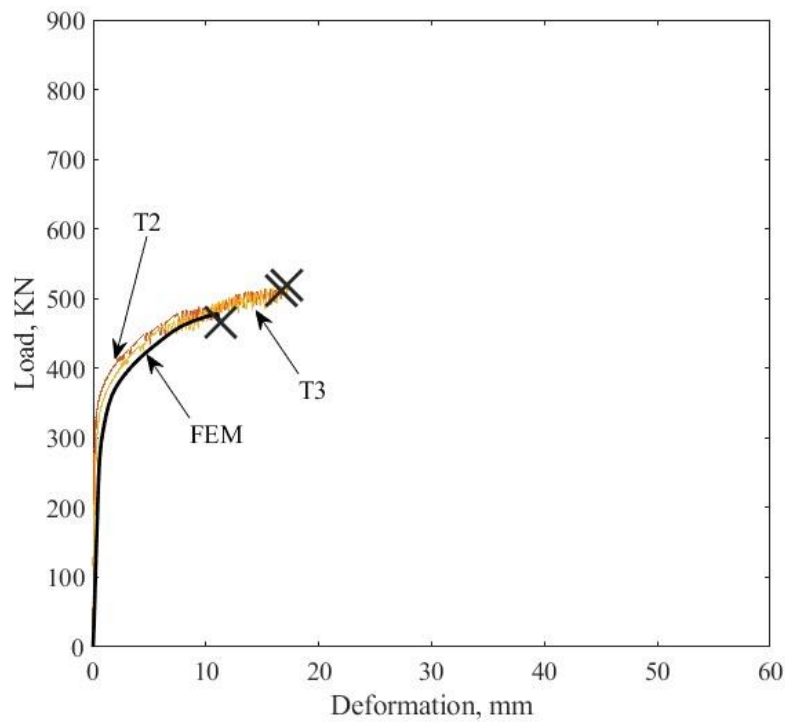
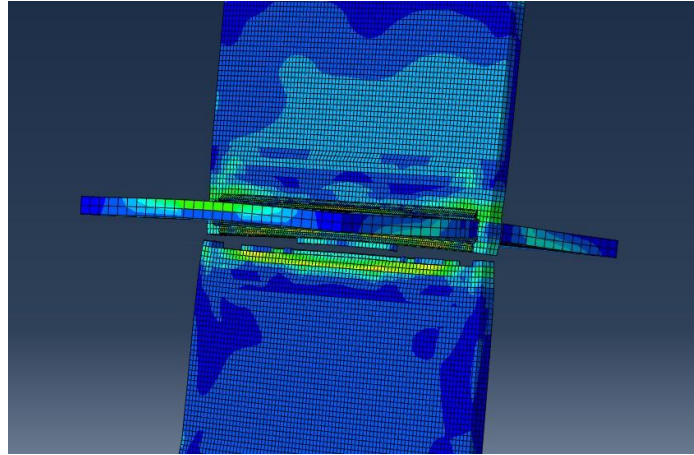


Figure 5.16: Finite element model results for transverse stiffener specimens.



(a)



(b)

Figure 5.17: Comparison between the failure location of the experimental test and FE model in T specimens (a) failure of specimen T3 and (b) close-up view on the failure in the FE model.

Figure 5.18 shows the load-deformation curves obtained from the FE model of the L specimens and compares them to the experimental ones. Again, the FE model properly captured the behavior with 1.5% prediction error for the ultimate strength and low error of 9% in predicting the elongation at ultimate load. Figures 5.19 and 5.20 show the FE model at different stage of failure. As seen from Figure 5.20, the model shows that the failure occurs in the AA5083 plate followed by the stiffener plates. This is due to the higher ductility of the AA6061 compared to AA5083 (see Section 4.1 for the results of the ancillary testing).

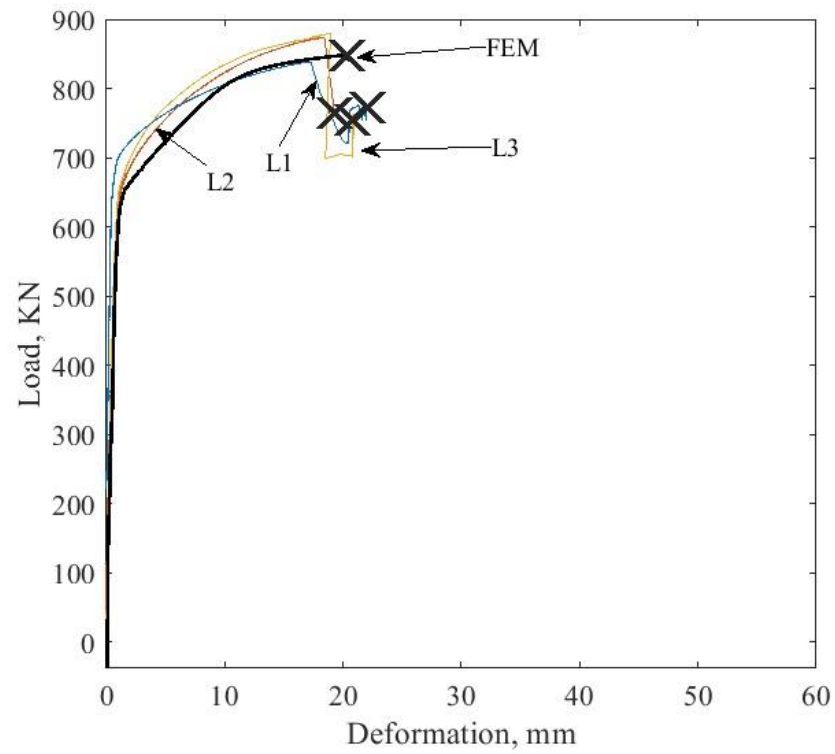


Figure 5.18: Finite element model results for longitudinal stiffener specimens.

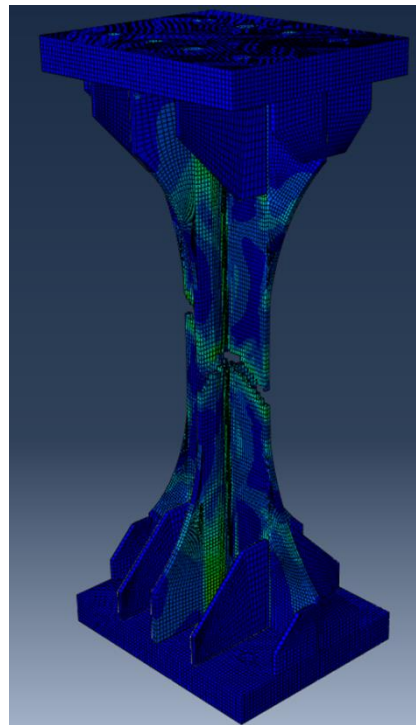


Figure 5.19: Overall failure of longitudinal stiffener specimen FE model.

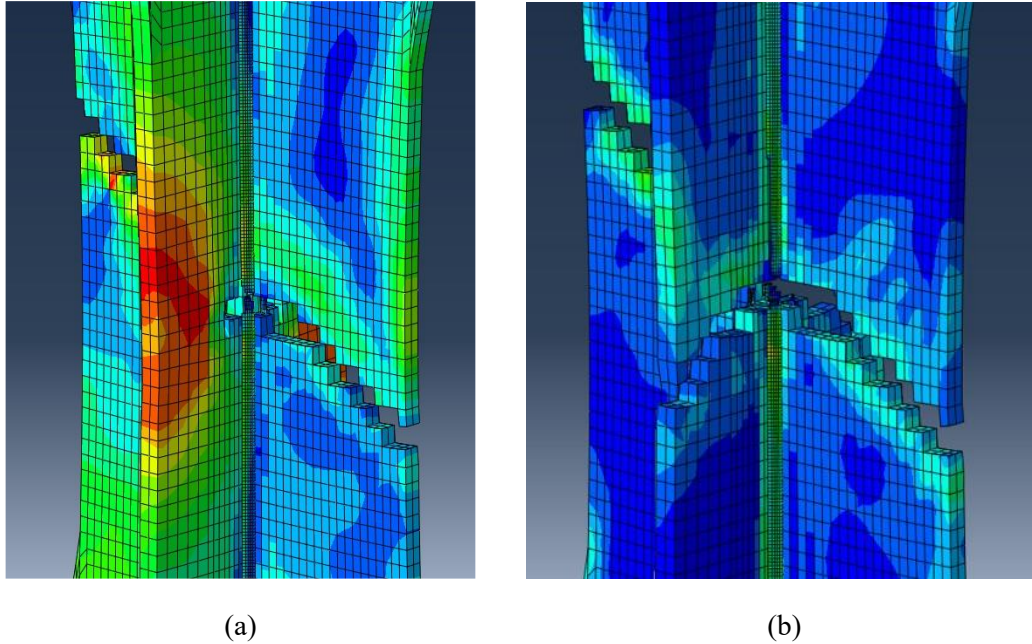


Figure 5.20: Behavior of longitudinal stiffener specimen FE model (a) failure of the main test plate and (b) overall failure.

Finally, Figure 5.21 shows the FE-obtained load-deformation profile of the LT specimen and compares them to the experimental results. The load-deformation behavior of the longitudinal and transverse stiffener specimen FE model was properly captured by the FE model. The FE model shows the gain of strength experienced by the specimens up to the ultimate strength. The drop in the load in the FE model, which indicates the failure of the stiffener, was higher than that observed in the tested specimens. This is attributed to the symmetry present in the FE model which causes all AA6061 stiffener components to fail at the same time instant, whereas in the experimental specimens the stiffeners will not all fail at the same time leading to a gradual drop in the specimen load. The FE prediction error in the ultimate strength prediction is 3.6% while for the fracture deformation is 2.4%. Figures 5.22 shows an overall view of the specimen after failure while Figure 5.23 shows the specimen at the initial failure point (i.e., failure of the stiffener) and after complete fracture. In summary, it seems that the utilized FE modeling approach can capture the significant characteristics of the behavior of the welded specimen.

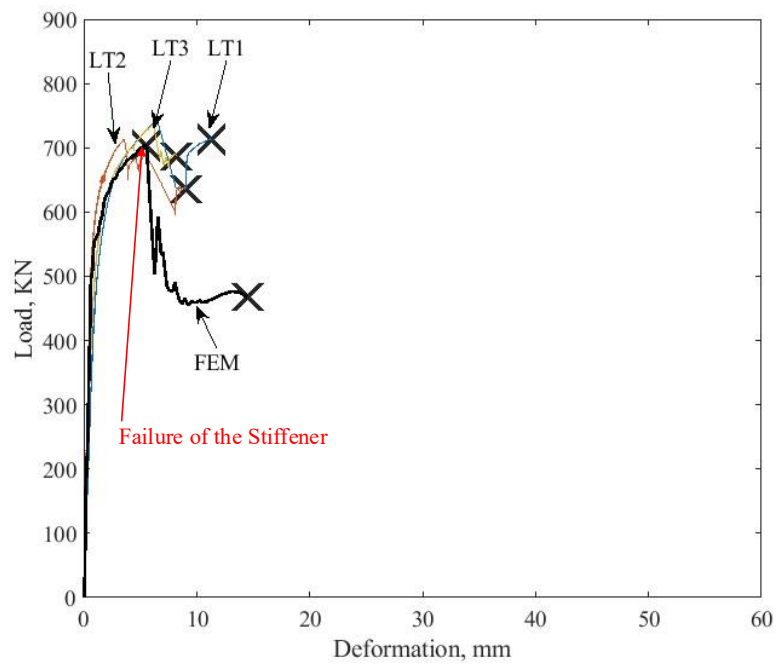


Figure 5.21: Finite element model results for the LT specimens.

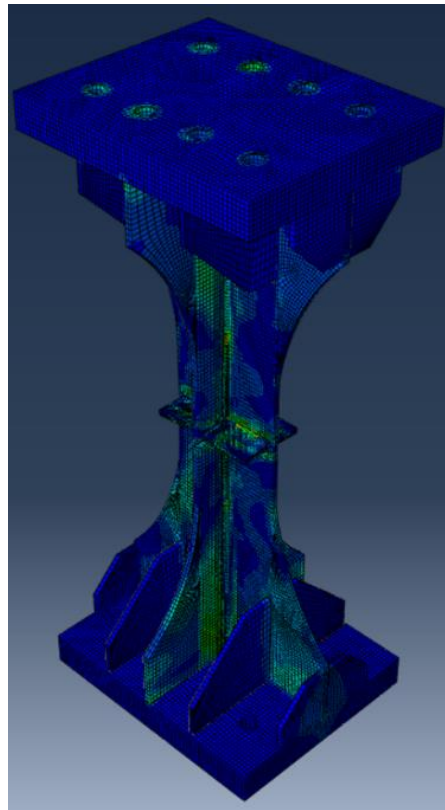


Figure 5.22: Overall failure of longitudinal and transverse stiffener specimen FE model.

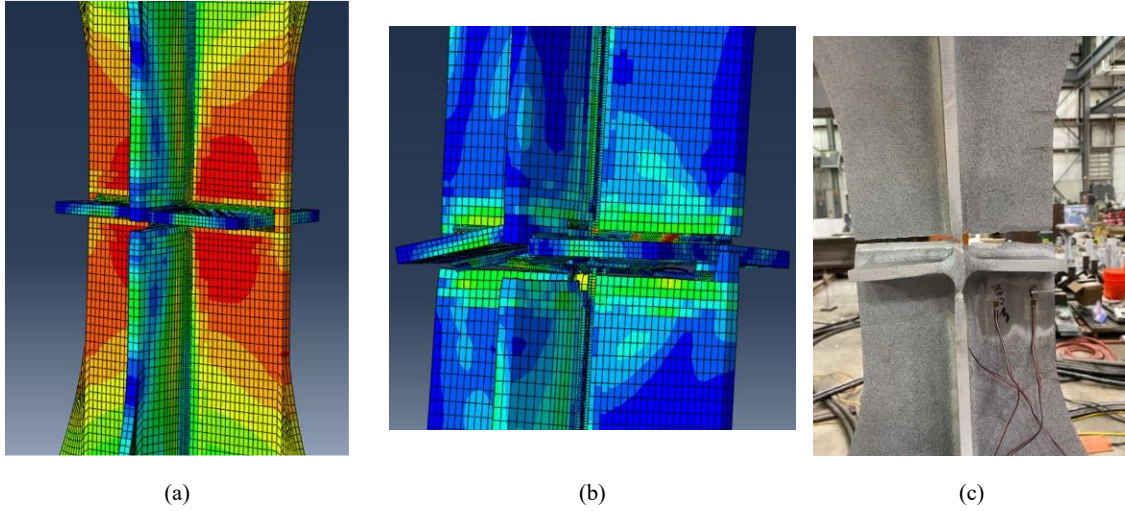


Figure 5.23: Behavior of the FE model of LT specimens (a) failure of the stiffener prior to the overall failure, (b) overall failure, and (c) failure of specimen T3 in the same manner (note the post failure orientation of the transverse stiffener that was captured by the FE model).

6 DISCUSSION

6.1 EFFECT OF SPECIMEN SIZE ON STRENGTH AND DUCTILITY

The ancillary testing alongside the large-scale testing created a rich database that can help quantify the effect of specimen size on the behavior. Figure 6.1 shows a comparison between the stress-strain curves obtained from the F Specimens and small-scale BM coupons of AA5083-H116. The results indicate that the size of the specimen plays an important role in the obtained mechanical properties of this aluminum alloy. Based on these results, the average yield strength obtained from the small-scale coupons is 20% higher than that obtained from the large-scale specimens. The average ultimate strength is only 7% higher than that of the large-scale specimens. However, the elongation at fracture in the large-scale specimens was on average (considering only Specimens F2 and F3) 5% higher than that experienced by the small-scale coupons.

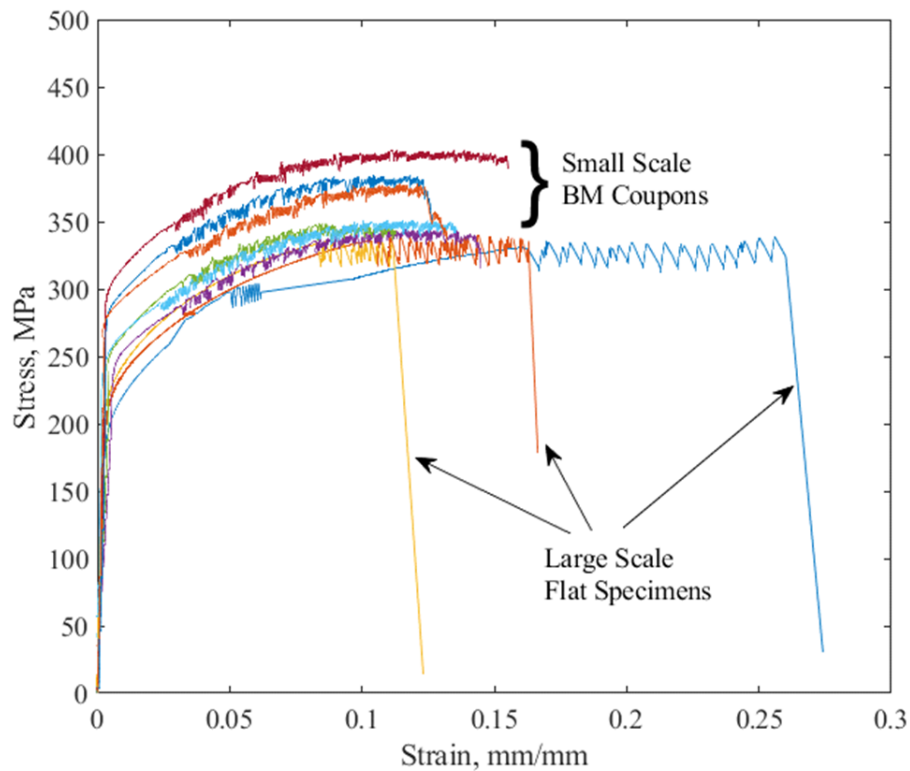


Figure 6.1: Stress-Strain curves of large scale and small-scale base metal tests of AA5083.

The findings discussed above in Figure 6.1 are different than those reported in Clausen et al. (2001) where it was observed that increasing the gauge length led to an increase in the yield strength of AA6082 and AA7108 aluminum alloys. It should be noted, however, that Clausen et

al. (2001) increased the gauge length from 30 mm to 70 mm, whereas in this report the size varied significantly between the small- and large-scale tested specimens. The small-scale coupon tested in this report had a gauge length of 32 mm while the large-scale specimen had a 205 mm gauge length. A more recent study by Mishra et al. (2023) conducted 360 coupon tests on AA6061 to examine the effect of specimen geometry on the obtained mechanical properties of this alloy. They investigated the aspect ratio, gauge length, thickness, and cross-sectional area. Their results agreed with the findings obtained in this report in that the yield and ultimate tensile strengths increase with the drop in the gauge length. However, in their results, the fracture strain also increased with the drop in the gauge length contrary to the observations reported herein. It should be noted that the largest specimen tested in Mishra et al. (2023) had a cross-sectional dimension of 12.7×7 mm ($0.5 \times 1/4$ -in) with a gauge length of 50.8 mm (2-in). Based on the experimental and numerical investigation results, it is apparent that the lower bound obtained from the ancillary coupon testing can properly represent the BM behavior in the large-scale specimens. This low bound was utilized herein to obtain the MRO fit parameters to be utilized in the FE models.

Another notable difference between the two sets of tests lies in the formation of the PLC serrations. Figure 6.2 compares the stress-strain curves of both sets of specimens at a certain strain window. As seen, the large-scale specimens experience well-pronounced and consistent sawtooth serrations that started at a higher strain compared to the ancillary testing coupons. The occurrence of serrations in the large specimens was also accompanied by a clear audible noise when the slip event occurred. Furthermore, the surfaces of the large-scale can clearly show the strain localization bands. The PLC bands were also visible on the surface of the small-scale coupons. Figure 6.3 compares the visible serration bands occurring in both specimens. Sarkar et al., (2007) investigated the microstructural behavior of the serrations. Al-Mg alloys were compared against low carbon steel in terms of the PLC instability. Due to the complex solute atmosphere from the presence of carbon and the low number of dislocations in low carbon steel, the stress drops are small and may not be seen in stress-strain curves. On the other hand, larger stress drops can be observed in aluminum alloys, especially in the large-scale specimens, due to the accumulation of the mobile dislocations as the solute atoms are incapable of saturating the field of dislocations (Sarkar et al., 2007). The characteristics of these serrations vary greatly and depend on the alloy composition, loading rate, temperature, among other factors (Darras et al., 2013; Zhang et al., 2020a).

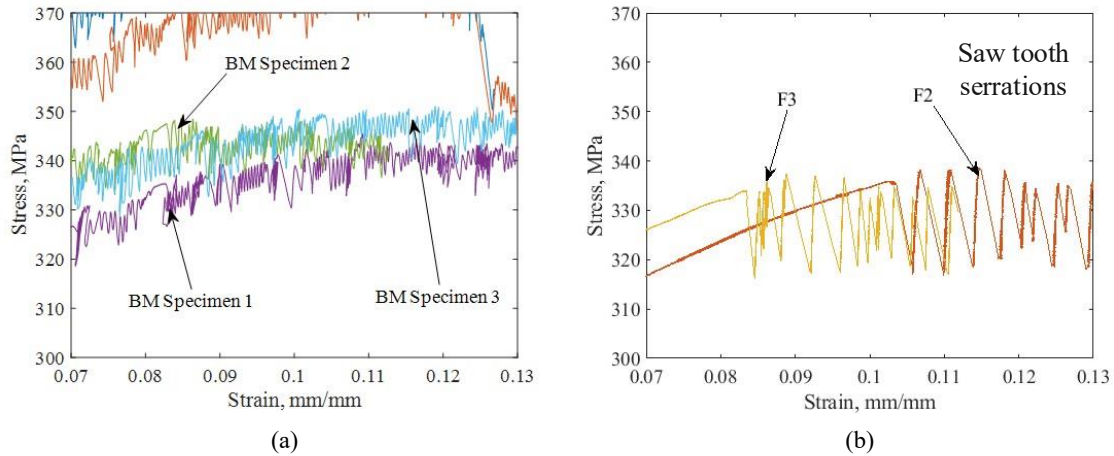


Figure 6.2: Different shapes of serrations of AA5083 (a) close-up view on the shape of the serrations in the small-scale coupons (b) close-up on the shape of serrations in the large-scale flat plate specimen.

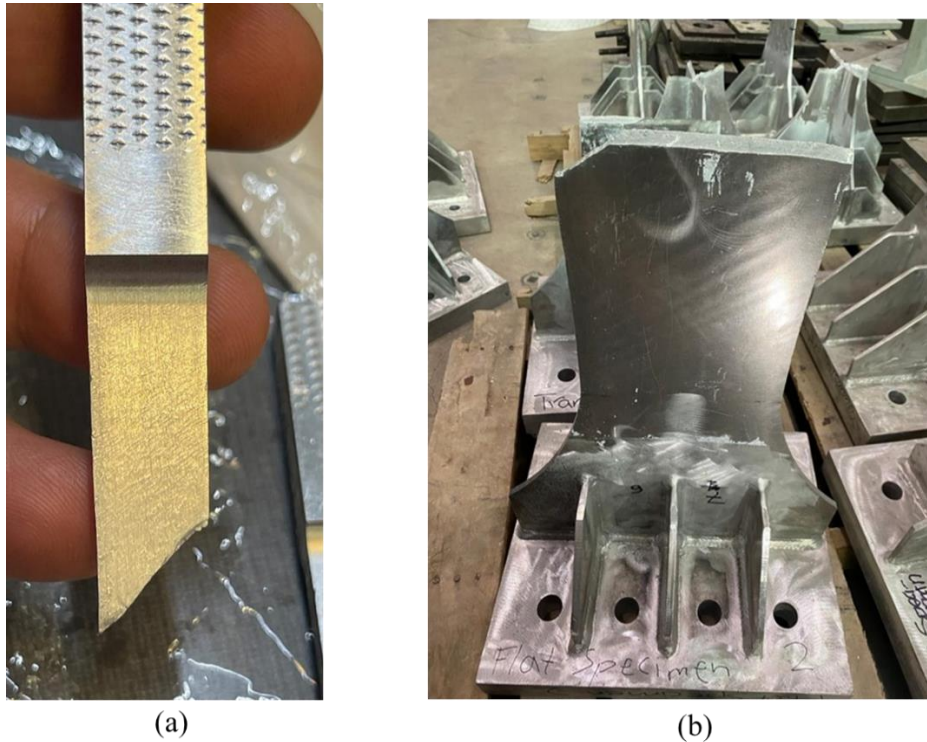


Figure 6.3: Visual appearance of serrations (a) closely spaced serrations in the small-scale coupons, and (b) widely spaced serrations in large-scale specimens.

6.2 EFFECT OF WELDING ON THE BEHAVIOR OF WELDED ALUMINUM COMPONENTS

Comparison of the results of the four specimen types shows the different load-deformation characteristics of each type. Figure 6.4 compares the load-deformation profile of a sample from

each specimen type that represent the average behavior of the three tests. As shown, flat plate specimens showed the highest ductility capacity of all the specimens. They also displayed clear PLC bands in the plastic regime. With the addition of a transverse stiffener, the ultimate strength and ductility started to drop; however, PLC bands also occurred in these specimens. These bands led to an uneven distribution of stresses along the weld line as evident by the DIC results. Surprisingly, the drop in the ultimate capacity of these transversally welded specimens was only 4.2% compared to unwelded flat plate specimens.

The addition of longitudinal stiffeners led to an expected increase in ultimate strength; however, it also led to a decrease in the ductility when compared to the flat specimens even though the stiffener material was shown, from the ancillary testing results, to be more ductile than the main test plate. This could be due to the strain compatibility between the two welded alloys and their different PLC behavior. In these longitudinally welded specimens, a single serration occurred and was accompanied by a large drop in the force followed shortly by the failure of the specimen. The DIC results show that this PLC band was more pronounced and wider compared to the ones occurring in the F or T specimens. Accordingly, subsequent loading had higher effect on the PLC affected region and the failure in the L specimens occurred closer to this band in each of the specimens.

The specimens with longitudinal and transverse stiffeners showed the lowest ductility of all the tested specimens. The capacity of these specimens also dropped compared to the L specimens. The drop in capacity between the L and LT specimens was significantly higher than the drop between the F and T specimens. This is because AA6061 shows more significant deterioration when welded as compared to the AA5083. The LT specimens did not display any clear PLC bands. This reduced ductility of the LT specimens was found to be significant and may cause premature failure of connections in aluminum marine vessels. Accordingly, more research should be dedicated to quantifying the effect of this drop in ductility on the safety and reliability of aluminum vessels.

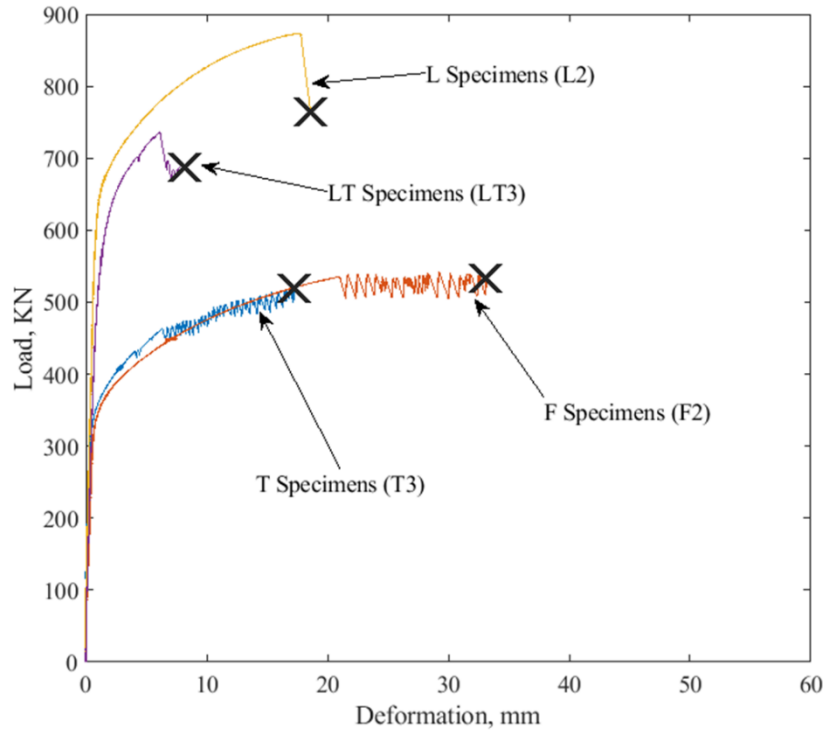


Figure 6.4: Load-deformation curves for the average of each stiffener configuration.

6.3 ULTIMATE STRENGTH PREDICTION

Based on the obtained results, it was of interest to the authors to study the accuracy of available strength prediction equations and their ability to capture the ultimate capacity of different specimens. Table 6.1 shows a comparison between the ultimate strengths obtained from the experimental and FE modeling results, and the nominal tensile strength predicted based on the *Aluminum Design Manual* (AA 2020) model. As seen in Table 6.1, the FE results are in good agreement with their experimental counterparts. The nominal strength prediction based on the *Aluminum Design Manual* (AA 2020) included three methods. The first prediction, i.e., *Aluminum Design Manual*¹, was conducted using the nominal mechanical properties adopted by AA (2020) for the BM and HAZ of both aluminum alloys and the filler metal. The capacity is simply predicted by multiplying the ultimate tensile strength by the appropriate area of the BM, HAZ, and/or fillet weld. As seen in the table, the predicted capacity is generally conservative with a predicted strength lower than the average experimental one by 10%, 16%, 7.25% and 3% for the F, T, L, and LT specimens, respectively. This is because the *Design Manual* (AA 2020) adopts lower bounds of the mechanical properties of different alloys prescribed by the appropriate ASTM specification for

each aluminum alloy. It should be noted, however, that the level of conservatism of LT specimens is significantly lower than that of the other specimen types; this will be discussed further below. The T specimens displayed the highest level of conservatism. This can be attributed to the complex behavior of these specimens characterized by non-uniform stress distribution along the weld line, coupled with the highly variable PLC behavior and a steep gradient of the mechanical properties (i.e., strength and ductility) across the HAZ.

Table 6.1: Comparison of the specimen capacity obtained from the experimental results, FE modeling, and the *Aluminum Design Manual* (AA 2020).

Type of results		Capacity KN (kips)			
		Flat Plate Specimen	Transverse Stiffener Specimen	Longitudinal Stiffener Specimens	Longitudinal & Transverse Stiffener Specimens
Experimental	Specimen 1	539 (121)	521 (117)	837 (188)	743 (167)
	Specimen 2	543 (122)	521 (117)	877 (197)	717 (161)
	Specimen 3	533 (120)	521 (117)	881 (198)	739 (166)
	Average	539 (121)	521 (117)	863 (194)	730 (164)
FEM		533 (120)	476 (107)	850 (191)	703 (158)
<i>Aluminum Design Manual</i> ¹		485 (109)	441 (99)	801 (180)	712 (160)
<i>Aluminum Design Manual</i> ²		530 (119)	467 (105)	899 (202)	823 (185)
<i>Aluminum Design Manual</i> ³		--	--	815 (183)	--

¹ Nominal strength computed using the strengths of the HAZ and BM for AA5083-H116 and AA6061-T6 reported in the *Aluminum Design Manual* (AA 2020).

² Nominal strength computed using the measured strengths of the HAZ (average) and BM (lower bound) from the conducted ancillary testing.

³ Weighted average nominal strength computed using the measured strengths of the HAZ (average) and BM (lower bound) from the conducted ancillary testing.

To attain a fair evaluation of the AA (2020) prediction model, the results from the experimental testing were compared against the design strength computed using the mechanical properties obtained from the ancillary testing conducted in this research program. The experimentally obtained average ultimate strength of the HAZ and filler metal, as well as the lower bound of the ultimate strength for the different aluminum alloys, was utilized in this comparison. The prediction results are reported in Table 6.1 corresponding to “*Aluminum Design Manual*²”. This method resulted in better prediction of the experimental failure loads for F and T specimens. However, they were 5% unconservative for L and 12.8% for LT specimens. This non-consistent

prediction accuracy shows the high complexity of quantifying the strength of welded aluminum components. For the L specimens, it is possible to obtain a rational prediction of the capacity using the weighted average method in AA (2020). The results are presented in “*Aluminum Design Manual*³” row. With this method, the predicted capacity is again on the conservative side of the experimental results.

As discussed above, for the LT specimens, the “*Aluminum Design Manual*²” prediction utilizing the measured properties was found to be unconservative. Based on the test observations, the more ductile and weaker HAZ of AA6061 experienced premature necking followed by specimen failure at low elongation levels. At this low elongation level, the stronger HAZ of the AA5083 has not yet reached its full ultimate capacity, but experienced sudden fracture due to the load re-distribution arising from the AA6061 stiffeners failure. Accordingly, proper strength prediction requires utilizing a design approach that considers strain compatibility. To further investigate this, the location of fracture within the different plates of the LT specimens was carefully observed from both the experimental specimens and the FE results. From the FE results, it was found that the fracture in the AA5083 occurred within Zone 2 of the defined HAZ sections. This corresponds to the material at 8 mm from the weld centerline of the ancillary testing specimen. The AA5083 plates in the experimental specimens generally fractured at a plane that is on average 9.1 mm away from the heel of the fillet welds. Note that although Zone 2 is defined at 8 mm from the weld line, it encompasses the material between 6 mm and 10 mm from the weld centerline. From the FE analysis, the fracture in the AA6061 stiffeners occurred within Zone 3 of the defined HAZ sections. From the test specimens, the fracture planes within the stiffeners were not uniform and on average were at 11.2 mm from the heel of the fillet welds. Again, it should be noted that Zone 3, although defined at 12 mm, covers the material between 10 mm and 14 mm from the weld centerline. Based on these observations, the stress-strain curves from Zone 2 and Zone 3 from the HAZ of AA5083 and AA6061, respectively, were utilized for achieving a better prediction of the capacity. The stress-strain behavior of the filler metal was also considered since it participates in the longitudinal load transfer. The three stress-strain curves are plotted in Figure 6.5.

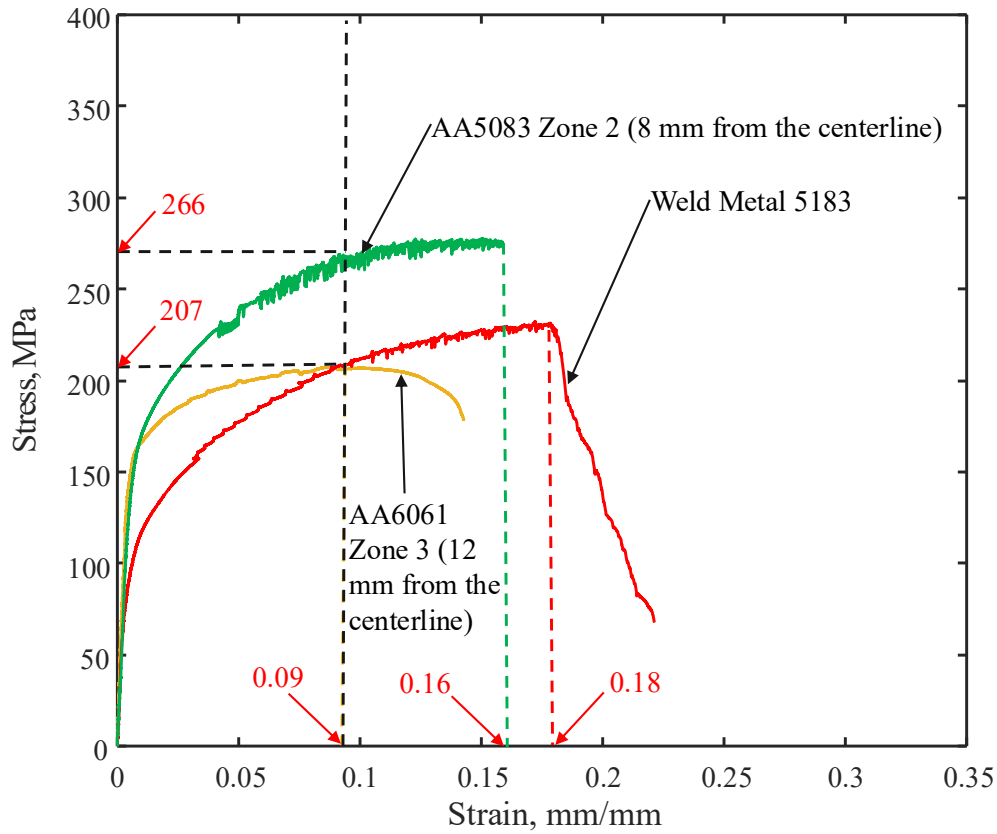


Figure 6.5: Stress-strain profiles of different components governing the strength of the LT specimens.

The traditional design approach in this case would add the ultimate strength of the three components to compute the nominal tensile capacity. However, as seen in Figure 6.5, the ultimate strengths of the three components do not occur at the same strain level. While the AA6061 stiffener reaches its ultimate strength at 0.09 mm/mm, the AA5083 reaches it at approximately 0.16 mm/mm, and the 5183 filler metal reaches it at 0.18 mm/mm. Accordingly, at the elongation in which the stiffener plates start fracturing, the other components of the specimen are carrying force lower than their individual ultimate capacity. As the AA6061 stiffener fractures, the stress redistribution increases the force on the AA5083 plate leading to failure. Thus, to accurately compute the specimen capacity, the force carried by the AA5083 plate and the 5183 filler metal at the ultimate strength of the AA6061 stiffener (i.e., strain of 0.09 mm/mm) should be considered rather than their ultimate strength. The stress obtained from the stress-strain curves of these

materials at strain of 0.09 mm/mm are then multiplied by the appropriate cross-sectional areas of the HAZ and fillet weld to compute the tensile capacity of that specimen. The tensile capacity in this case is equal to 723 KN (162.5 kips) which corresponds to an error of 0.9% when compared to the average strength obtained from the experimental tests (i.e., 730 KN (164 kips)). This highlights the importance of considering strain compatibility when designing components combining different welded alloys.

Table 6.2 shows the ultimate elongation of the tested specimens compared to the FEM results. The values in Table 6.2 show a decline in the ultimate deformations of the specimens that occurs with transversally welded specimens. The lowest deformation capacity is associated with the LT specimens. A similar decrease can be seen in the FEM results which were generally in good agreement with the experimental counterparts. Further research is needed to quantify the effect of this drop in ductility on the reliability of marine vessels.

Table 6.2: Comparison of the ultimate elongation between the experimental results and FEM.

Type of results		Ultimate Elongation mm (inches)			
		Flat Plate Specimen	Transverse Stiffener Specimen	Longitudinal Stiffener Specimens	Longitudinal & Transverse Stiffener Specimens
Experimental	Specimen 1	53* (2.08)	51** (2.00)	17.5 (0.69)	6.4 (0.25)
	Specimen 2	33 (1.30)	18 (0.71)	19 (0.75)	6.2 (0.24)
	Specimen 3	23 (0.91)	17 (0.67)	18 (0.71)	3.5 (0.14)
	Average	28 (1.1)	17.5 (0.69)	18.16 (0.715)	5.36 (0.211)
FEM		25 (0.98)	11.5 (0.45)	20 (0.78)	5.5 (0.216)

*Removed from average calculation due to multiple load cycles

**Removed from average calculation due to LVDT malfunction

6.4 SIMPLIFICATIONS TO THE FINITE ELEMENT MODELING PROCEDURE

The results discussed in Section 5 show that the finite element procedure can predict the load-deformation behavior of the tested specimens with reasonable accuracy. The average error in ultimate strength prediction is 3.6%. This approach can be used to model large aluminum stiffened panel and ultimately, aluminum hull girders; however, the level of details incorporated into the model would significantly increase the computational cost and analysis duration. As a result, the

effect of different simplifications to the modeling approach are investigated next. These included the effect of residual stresses, weld line modeling, and definition of the mechanical properties across the HAZ.

6.4.1 Effect of the residual stresses

To quantify the effect of modeling the residual stresses on the response, models were created without incorporating the residual stresses for the T and L specimens and compared to the results of the original models. The results, shown in Figure 6.6 and 6.7, indicate that removal of the residual stresses does not have a significant impact on the tensile behavior. This is also in line with the results reported in Collette (2022) in which the residual stresses did not lead to significant change in the behavior of the model for plates with transverse, non-load carrying fillet welds.

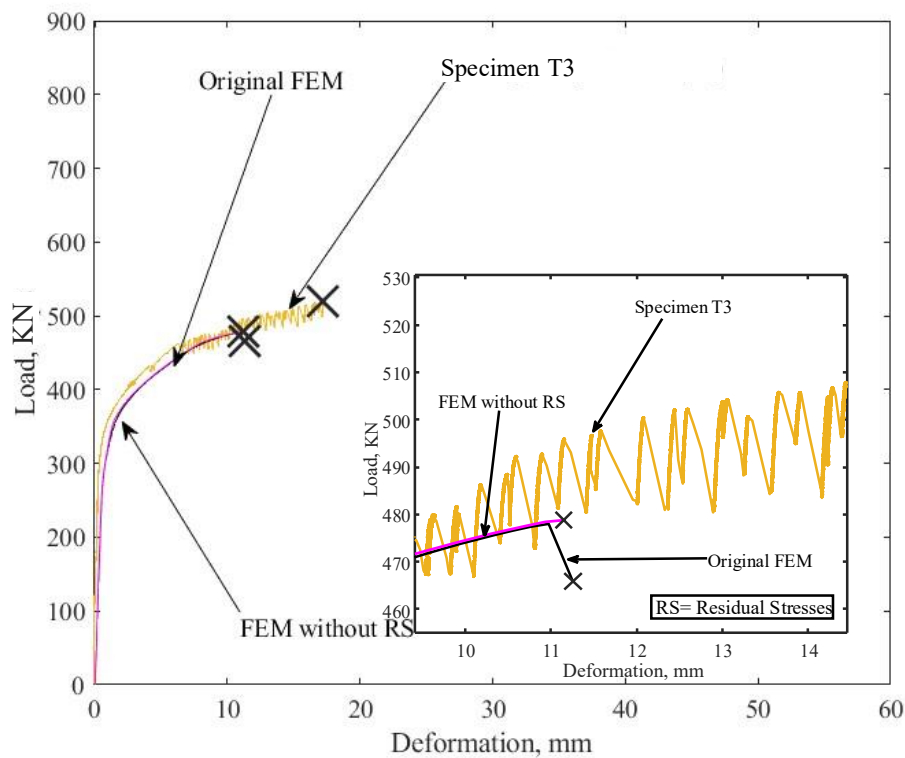


Figure 6.6: Load-deformation curves of Specimen T3 along with the original FE results and the FE results without residual stresses.

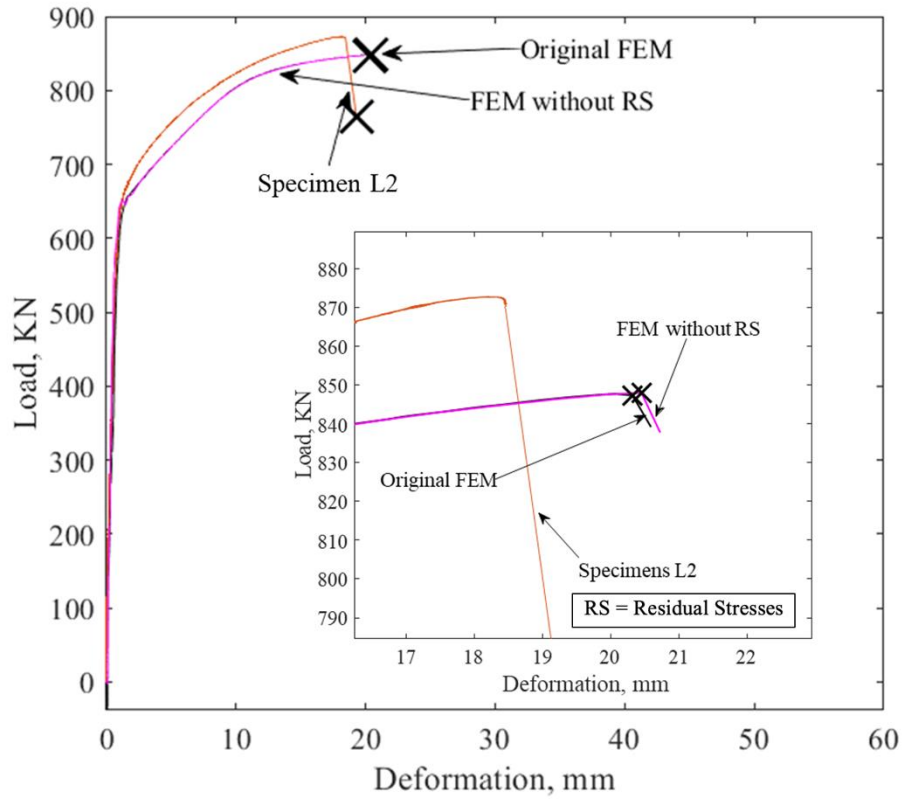


Figure 6.7: Load-deformation curves of Specimen L2 along with the original FE results and the FE results without residual stresses.

6.4.2 Effect of modeling the weld lines

Next, the weld lines between the AA6061 stiffeners and the AA5083 main plate in the T, L, and LT specimens are removed from the FE models and replaced with a tie constraint on the element interface to transfer the force between the two components. The comparative results are shown in Figures 6.8-6.10. As seen in the figures, removing the weld line from the model leads to a minor change in the load-deformation behavior. For the L specimens (see Figure 6.9), a negligible decrease in the ultimate elongation and the predicted fracture load is observed. However, for the LT specimens (Figure 6.10), the model without the weld lines showed a 2% higher ultimate load and 1.5% higher elongation at ultimate load. This can be attributed to the tie constraint that does not account for the fracture in the weld elements leading to higher ultimate force and elongation.

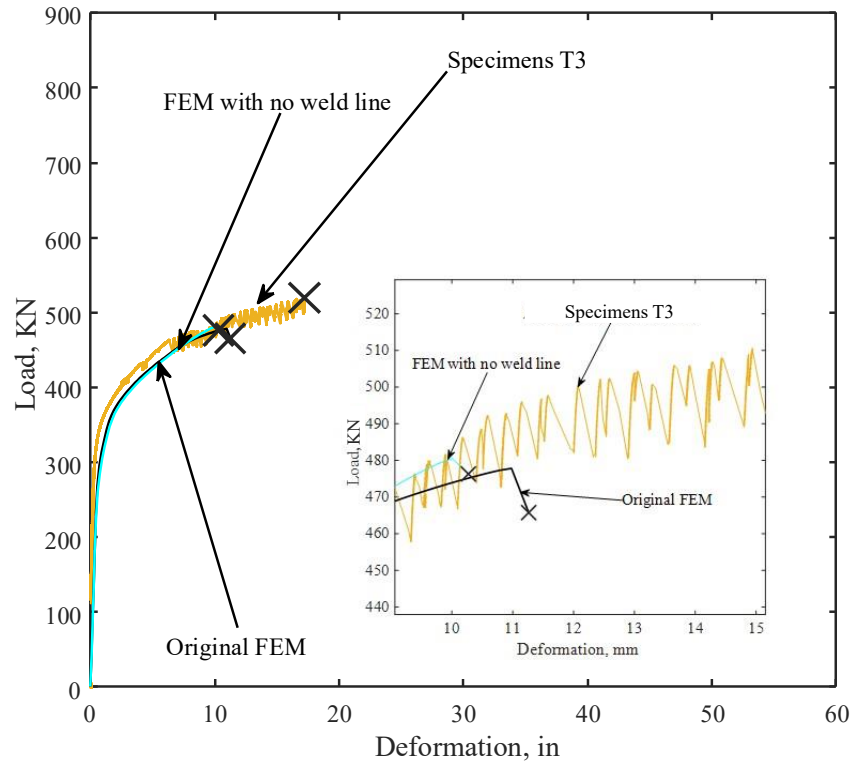


Figure 6.8: Load-deformation curves of Specimen T3 along with the original FE results and the FE results with no weld lines.

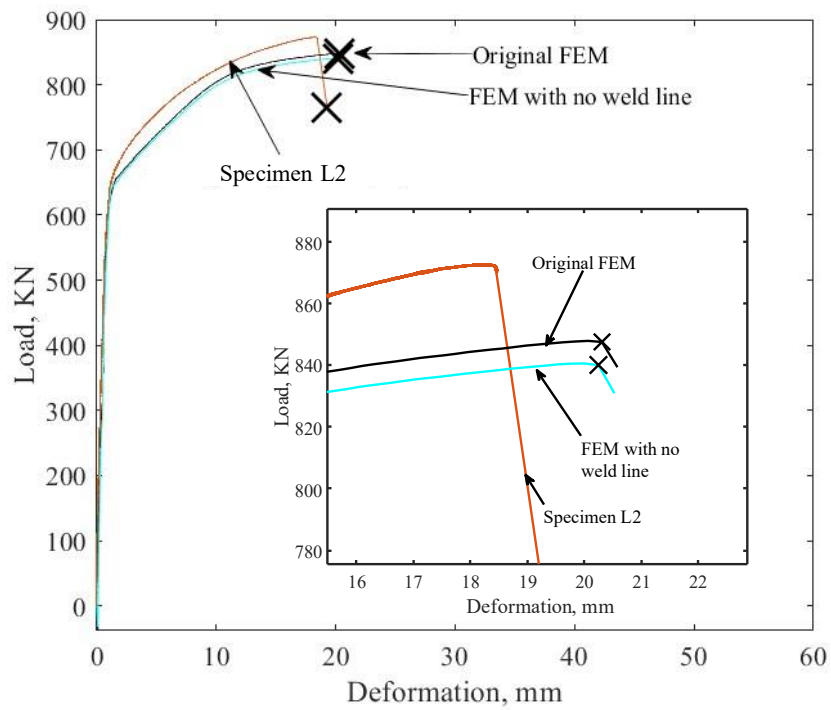


Figure 6.9: Load-deformation curves of Specimen L2 along with the original FE results and the FE results with no weld lines.

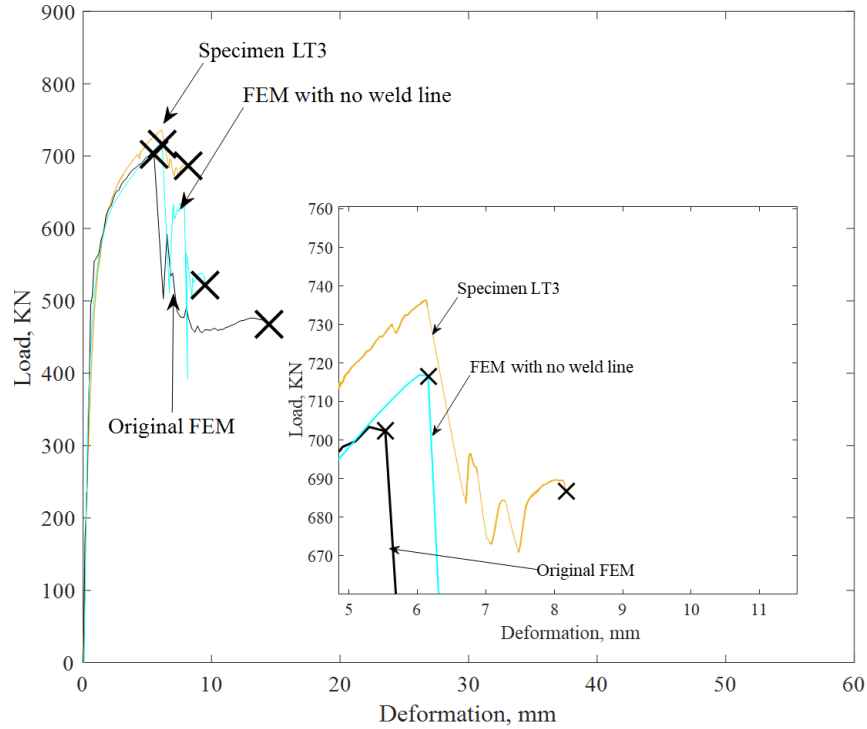


Figure 6.10: Load-deformation curves of Specimen LT3 along with the original FE results and the FE results with no weld lines.

6.4.3 Simplified mechanical properties of the HAZ

Based on inspecting the models and comparing the modeling results to their experimental counterparts, it can be seen that the mechanical properties of the different zones within the HAZ are among the main parameters that govern the behavior of the specimens. After careful visual inspection of the fracture locations in different specimens from the experimental testing program and the finite element model, it was observed that all T specimens failed on average at 5.3 mm from the toe of the fillet weld (or 9.1 mm from the heel of the weld line). This location coincides with HAZ Zone 2 defined for AA5083-H116 in Figure 4.3 (i.e., 8 mm from the centerline of the butt weld in the ancillary testing specimens). Inspecting the FE model of the T specimens also shows that the failure of the specimen occurred within Zone 2 of the HAZ. Therefore, the entire HAZ in the FE models of the specimens was defined to have the mechanical properties of Zone 2. Additional analysis was also conducted by defining the entire HAZ to have mechanical properties of Zone 1 (4 mm from the weld centerline) and Zone 3 (12 mm from the weld centerline). The results of the FE analysis of the T specimen are presented in Figure 6.11. From the results, it seems that utilizing the adopted single definitions of the stress-strain behavior of the entire HAZ leads to lower estimate of the capacity. However, utilizing the mechanical properties of either Zones 2 or

3 leads to very similar prediction of the ultimate strength since they have very similar stress-strain behavior (see Figure 4.3). As a result, it was chosen to utilize the mechanical properties of Zone 2 for AA5083 to represent the properties of the entire HAZ in the analysis discussed below.

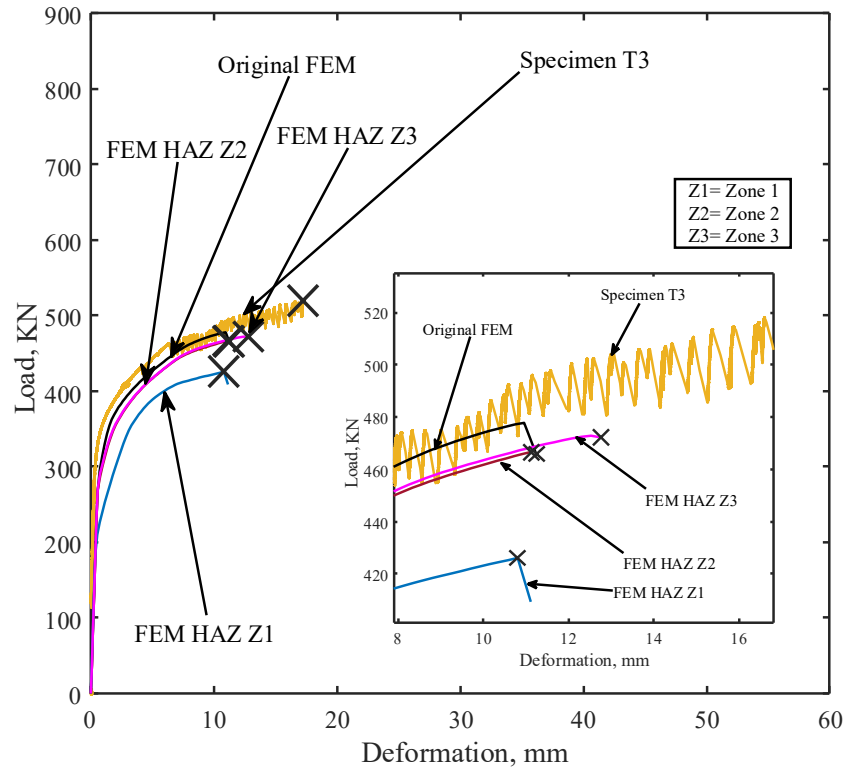


Figure 6.11: Load-deformation curves of Specimen T3, the original FE model, and FE models with different HAZ zones assigned to the full extent of the HAZ.

Next, the same investigation is conducted on the FE model of the LT specimen. Again, Zone 2 properties are assigned to the entire HAZ of the AA5083 main test plate. For the AA6061, the location of failure in the experimental specimens was on average 11.2 mm away from the heel of the weld. However, the variability in this value was high with a 25% COV. Accordingly, for the HAZ of the AA6061 stiffeners, properties of Zones 2 and 3 are considered in two separate models. The results are shown in Figure 6.12. In the figure, FEM HAZ Case A profile refers to the model with AA6061 HAZ Zone 2 (i.e., 8 mm from the centerline) properties assigned to the entire HAZ of the stiffener plate while FEM HAZ Case B utilizes Zone 3 (i.e., 12 mm from the centerline) properties for the entire HAZ of the stiffener plate. As shown for FEM HAZ Case A the ultimate deformation was close to the original FE model; however, the strength of the model was lower due

to the low ultimate strength of Zone 2 in the HAZ of the AA6061. On the other hand, FEM HAZ Case B resulted in a slight increase in the ultimate strength and deformation of the model compared to the original FE model. However, the error in predicting these quantities is within 4.2% when compared to the average experimental results. In summary, it seems that these simplifications can be made to provide rapid assessment of the behavior; however, for detailed analysis, it is essential to model the various zones.

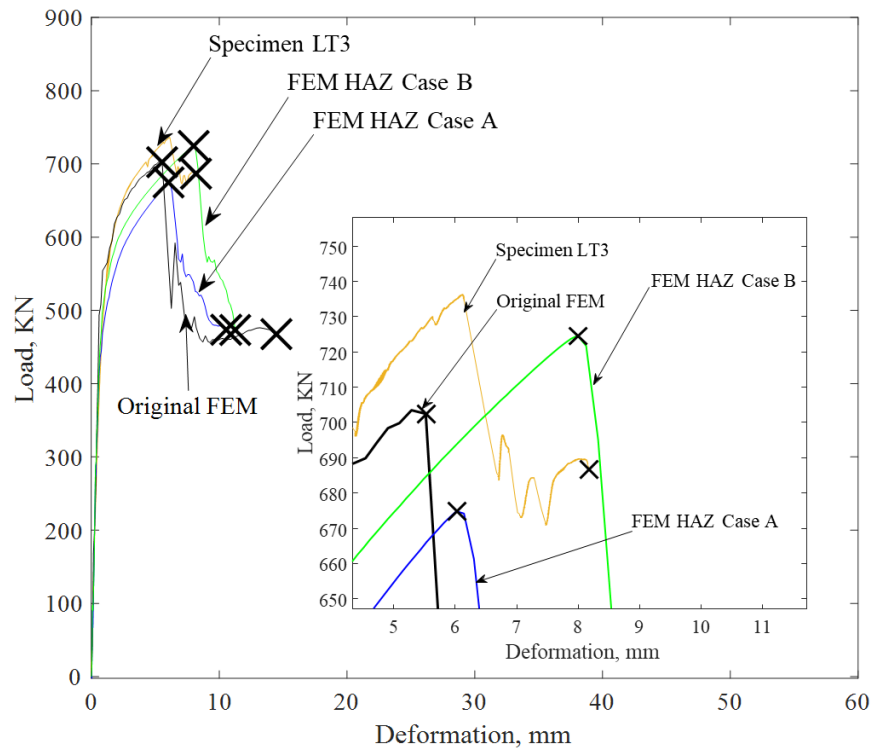


Figure 6.12: Load-deformation curves showing the average LT specimen, the original FEM and FE models with different HAZ zones assigned to the full extent of the HAZ.

7 CONCLUSIONS AND RECOMMENDATIONS FOR FUTURE WORK

7.1 CONCLUSIONS

This report investigated the tensile strength and ductility of welded aluminum components. An experimental investigation was carried out on plates with and without welded stiffeners. The stiffened specimens included ones with welded transverse stiffeners, longitudinal stiffeners, and specimens that combined both longitudinal and transverse stiffeners. Accordingly, load carrying and non-load carrying fillet welds were included in the test matrix to investigate their effect on the behavior. Twelve large-scale specimens, with three specimens from each type, were tested under tensile loading to characterize their load-deformation behavior and ultimate tensile strength. Characterization of the mechanical properties across the HAZ for the two investigated aluminum alloys, AA5083-H116 and AA6061-T6, was performed through small-scale coupon testing. Numerical finite element analysis was conducted to develop a deeper understanding of the behavior and investigate the effect of key underlying parameters on the response. The following conclusions can be drawn:

- The results of the coupon testing highlighted the variability in the mechanical properties of unwelded aluminum, and the variation in the mechanical properties across the HAZ. However, this ancillary testing assisted in providing baseline information that was crucial in understanding the behavior of the large-scale welded specimens.
- For the conducted testing under the adopted test procedures, the AA5083 specimens showed a distinctive “jerky” flow in the plastic domain that was followed by sudden brittle failure. The AA6061 followed a stress relaxation behavior and failed in a ductile necking manner.
- The large-scale samples of each specimen type displayed consistency with respect to the failure mechanism and ultimate strengths. Specimens with transverse welds experienced a reduction in the ultimate elongation that was significant when both longitudinal and transverse stiffeners are included.
- The variability in the ultimate strength and elongation of each specimen type was generally low; except for the flat plate specimens which had a higher COV of the ultimate deformation. This can be attributed to the highly variable PLC behavior that governs the response in the plastic domain.

- The utilized numerical modeling approach was able to capture the behavior exhibited in experimental testing. Although the ultimate strength and elongation were captured with low prediction error, the adopted material constitutive models did not capture the PLC behavior.
- The effect of specimen size on the stress-strain behavior was evaluated by comparing the testing results from the small- and large-scale AA5083 specimens. It was found that the stress-strain curves of the large-scale specimens were closer to the lower bound of the curves obtained from the small-scale coupons.
- The DIC was able to provide invaluable data showing the occurrence of the PLC bands, regions of high strain concentrations, and necking of the material. It provided evidence that the PLC effect was a major factor in governing the behavior of the tested specimens in the plastic domain.
- The available design equations can conservatively predict the strength of a welded specimens; however, the level of conservatism was not consistent with respect to the specimen type. The predicted strength was lower than the average experimental one by 10%, 16%, 7.25% and 3% for the F, T, L, and LT specimens, respectively. This will lead to non-consistent reliability levels for the designed component. While the prediction was highly conservative for some specimen types, it was significantly less conservative for the LT specimens. This is because the available design models do not account for strain compatibility that governs the behavior of specimens combining different alloying materials.
- Although the available design equations were able to predict the capacity of the components, design models should include ductility measures to prevent premature failure and ensure the reliability of aluminum vessels under sea loading.

7.2 RECOMMENDATIONS FOR FUTURE WORK

This conducted work highlighted that the presence of welds with different orientations has a significant impact on the behavior of aluminum structures. Based on the findings of this work, several areas need to be explored to further enhance our understanding of the behavior:

- The scarcity of large-scale testing data for understanding the behavior of aluminum under tensile loading in literature calls for additional testing to cover more complex and large-scale specimen configurations (e.g., stiffened panels or box girders).
- The results reported here apply to AA5083-H116 and AA6061-T6 alloys. More testing is needed to characterize the load deformation behavior of other commonly used alloys such as AA5086, and AA6082.
- The utilized coupons to characterize the HAZ properties were extracted from butt weld specimens. More research should be dedicated to characterizing the HAZ properties in components with fillet welds.
- Further investigations are needed to develop more simplified FE modelling techniques to reduce the computational cost needed for modeling larger and more complex ship frames such as the use of shell elements.

8 REFERENCES

- American Beureau of Shipping (ABS) (2023). *ABS Rules for Building and Classing High-Speed Craft*. American Bureau of Shipping, Spring, TX, USA.
- Aluminum Design Manual*. (2020). The Aluminum Association. Arlington, VA, USA.
- Ambriz, R. R., Froustey, C., and Mesmacque, G. (2013). Determination of the tensile behavior at middle strain rate of AA6061-T6 aluminum alloy welds. *International Journal of Impact Engineering*, 60, 107-119. <https://doi.org/10.1016/j.ijimpeng.2013.04.006>
- ANSI/AISC 360*. (2016). Specification for structural steel buildings. American Institute of Steel Construction, Chicago, IL, USA.
- ANSYS, I. (2015). *ANSYS documentation*.
- Arun, M., and Ramachandran, K. (2015). Effect of welding process on mechanical and metallurgical properties of AA6061 aluminum alloy lap joint. *International Journal of Mechanical Engineering and Research*, 5(1).
- Ashwani Kumar, Gautam, S. S., and Kumar, A. (2014). Heat input & joint efficiency of three welding processes TIG, MIG and FSW using AA6061. *International Journal of Mechanical Engineering and Robotics Research*, 89-94.
- Askariani, S. S., and Garivani, S. (2020). More details about validation of calibrated parameters of ductile damage model for A36 steel plates in Abaqus software. <https://doi.org/https://doi.org/10.13140/RG.2.2.31179.62241/6>
- Askariani, S.S., Garivani, S., and Aghakouchak, A.A. (2020). Application of slit link beam in eccentrically braced frames. *Journal of Constructional Steel Research*, 170, 106094. <https://doi.org/10.1016/j.jcsr.2020.106094>
- ASTM A572. (2021). *Standard Specification for High-Strength Low-Alloy Columbium-Vanadium Structural Steel*. Amerinca Society for Testing and Materials (ASTM), West Conshohocken, PA, USA.
- ASTM B221. (2020). *Standard Specification for Aluminum and Aluminum-Alloy Extruded Bars, Rods, Wires, Profiles, and Tubes*, Amerinca Society for Testing and Materials (ASTM), West Conshohocken, PA, USA.
- ASTM B316. (2010). *Standard Specification for Aluminum and Aluminum-Alloy Revit and Cold-Heading Wire and Rods*, Amerinca Society for Testing and Materials (ASTM), West Conshohocken, PA, USA.
- ASTM B557. (2023). *Standard Test Methods for Tension Testing Wrought and Cast Aluminum and Magnesium Alloy Products*, Amerinca Society for Testing and Materials (ASTM), West Conshohocken, PA, USA.
- ASTM F436/F436M. (2019). *Standard Specification for Hardened Steel Washers Inch and Metric Dimensions*, Amerinca Society for Testing and Materials (ASTM), West Conshohocken, PA, USA.

- ASTM B928-15. (2015). Standard Specification for High Magnesium Aluminum-Alloy Products for Marine Service and Similar Enviroments, Amerinca Society for Testing and Materials (ASTM), West Conshohocken, PA, USA.
- ASTM. (2017). Standard Test Methods for Vickers Hardness and Knoop Hardness of Metallic Materials Amerinca Society for Testing and Materials (ASTM), West Conshohocken, PA, USA.
- AWS. (2014). Structural Welding Code-Aluminum D1.2/D1.2M. American Welding Society (AWS), Miami, FL, USA.
- AWS. (2020). Structural Welding Code-Steel D1.1/D1.1M. American Welding Society (AWS), Miami, FL, USA.
- Bakar, S. R. S., Ahmad, M. Y., Ibrahim, M. F. A., Jalar, A., Djalil, S. J. S., and Othman, N. K. (2012). The effect of double pass GMAW process on microstructure and mechanical properties of AA 6061-T6 joining plates. *Key Engineering Materials*, 510-511, 98-104. <https://doi.org/10.4028/www.scientific.net/KEM.510-511.98>
- Benson, S., Downes, J., and Dow, R. S. (2013). Load shortening characteristics of marine grade aluminium alloy plates in longitudinal compression. *Thin-Walled Structures*, 70, 19-32. <https://doi.org/https://doi.org/10.1016/j.tws.2013.04.006>
- Børvik, T., Forrestal, M. J., Hopperstad, O. S., Warren, T. L., and Langseth, M. (2009). Perforation of AA5083-H116 aluminium plates with conical-nose steel projectiles – Calculations. *International Journal of Impact Engineering*, 36(3), 426-437. <https://doi.org/https://doi.org/10.1016/j.ijimpeng.2008.02.004>
- Clausen, A. H., Børvik, T., Hopperstad, O. S., and Benallal, A. (2004). Flow and fracture characteristics of aluminium alloy AA5083–H116 as function of strain rate, temperature and triaxiality. *Materials Science and Engineering: A*, 364(1), 260-272. <https://doi.org/https://doi.org/10.1016/j.msea.2003.08.027>
- Clausen, A. H., Tryland, T., and Remseth, S. (2001). An investigation of material properties and geometrical dimensions of aluminum extrusions. *Materials & Design*, 22(4), 267-275. [https://doi.org/10.1016/S0261-3069\(00\)00092-3](https://doi.org/10.1016/S0261-3069(00)00092-3)
- Collette, M. (2022). Experimental Quantification of the Tensile Strength and Ductility of Under-Matched Aluminum Welds, SSC-478. *Ship Structure Committee*.
- Collette, M. D. (2007). The impact of fusion welds on the ultimate strength of aluminum structures. *Proceedings of PRADS*,
- Cruz, K. S., Meza, E. S., Fernandes, F. A. P., Quaresma, J. M. V., Casteletti, L. C., and Garcia, A. (2010). Dendritic arm spacing affecting mechanical properties and wear behavior of Al-Sn and Al-Si alloys directionally solidified under unsteady-state conditions. *Metallurgical and Materials Transactions A*, 41(4), 972-984. <https://doi.org/10.1007/s11661-009-0161-2>
- Cueca, F., Patarroyo, A., Rojas, F., Solano, E., Morales, A., and Muñoz, R. (2012). Study of the weld ability of Aluminum Alloy 5083 H116 with Pulsed Arc GMAW (GMAW-P). *Ship science & technology = Ciencia y tecnología de buques*, 6(11), 43.

- Dahdouh, S., Ait-Amokhtar, H., and Sadeddine, A. (2022). On the combined role of strain hardening and strain rate on the degree of heterogeneity of plastic flow in an Al-2.5%Mg alloy. *Mechanics of Solids*, 57(6), 1550-1560.
<https://doi.org/10.3103/s002565442206019x>
- Darras, B. M., Abed, F. H., Pervaiz, S., and Abdu-Latif, A. (2013). Analysis of damage in 5083 aluminum alloy deformed at different strain rates. *Materials science & engineering.*, 568, 143-149. <https://doi.org/10.1016/j.msea.2013.01.039>
- Davis, J. R. (2001). 16. Aluminum and Aluminum Alloys. In *Alloying - Understanding the Basics*. ASM International. <https://app.knovel.com/hotlink/pdf/id:kt00URDMI8/alloying-understanding/aluminum-aluminum-alloys>
- Dørum, C., Lademo, O.-G., Myhr, O. R., Berstad, T., and Hopperstad, O. S. (2010). Finite element analysis of plastic failure in heat-affected zone of welded aluminium connections. *Computers & Structures*, 88(9), 519-528.
<https://doi.org/https://doi.org/10.1016/j.compstruc.2010.01.003>
- Du, Z., Xu, K., Wang, L., Zhang, X., and Zhang, X. (2022). Characterization of the local mechanical properties of 5083-5383 MIG welded joints. *Journal of Physics: Conference Series*, 2390(1), 012013. <https://doi.org/10.1088/1742-6596/2390/1/012013>
- Dutra, J. C., e Silva, R. H. G., Savi, B. M., Marques, C., and Alarcon, O. E. (2015). Metallurgical characterization of the 5083-H116 aluminum alloy welded with the cold metal transfer process and two different wire-electrodes (5183 and 5087). *Welding in the World*, 59(6), 797-807. <https://doi.org/10.1007/s40194-015-0253-0>
- EN 485. (2013). Aluminium and aluminium alloys – Sheet, strip and plate – Part 2: Mechanical properties. European Committee for Standardization (CEN) Brussels, Belgium.
Eurocode 9 Design of Aluminum Structures. (2007) European Committee for Standardization (CEN) Brussels, Belgium.
- Farajkhah, V., and Liu, Y. (2016a). Effect of fabrication methods on the ultimate strength of aluminum hull girders. *Ocean Engineering*, 114, 269-279.
<https://doi.org/https://doi.org/10.1016/j.oceaneng.2016.01.029>
- Farajkhah, V., and Liu, Y. (2016b). Effect of metal inert gas welding on the behaviour and strength of aluminum stiffened plates. *Marine Structures*, 50, 95-110.
<https://doi.org/https://doi.org/10.1016/j.marstruc.2016.07.005>
- Farajkhah, V., Liu, Y., and Gannon, L. (2017). Finite element study of 3D simulated welding effect in aluminium plates. *Ships and Offshore Structures*, 12(2), 196-208.
<https://doi.org/10.1080/17445302.2015.1123865>
- Fricke, W. (2005). Effects of residual stresses on the fatigue behaviour of welded steel structures. *Materialwissenschaft und Werkstofftechnik*, 36(11), 642-649.
<https://doi.org/10.1002/mawe.200500933>
- Germain, P. (1986). Cours de mécanique de l'École Polytechnique. *Ellipses, Paris*.

- Giannotti, J. G., and Stambaugh, K. A. (1984). Determination of strain rates in ship hull structures: a feasibility study, SSC-317. *Ship Structure Committee*.
- Goldak, J., Chakravarti, A., and Bibby, M. (1984). A new finite element model for welding heat sources. *Metallurgical Transactions B*, 15(2), 299-305.
<https://doi.org/10.1007/BF02667333>
- Gurney, T. R. (1979). Fatigue of welded structures. CUP Archive.
- Hakem, M., Lebaili, S., Mathieu, S., Miroud, D., Lebaili, A., and Cheniti, B. (2019). Effect of microstructure and precipitation phenomena on the mechanical behavior of AA6061-T6 aluminum alloy weld. *The International Journal of Advanced Manufacturing Technology*, 102(9), 2907-2918. <https://doi.org/10.1007/s00170-019-03401-1>
- He, J., Ling, Z., and Li, H. (2016). Effect of tool rotational speed on residual stress, microstructure, and tensile properties of friction stir welded 6061-T6 aluminum alloy thick plate. *International Journal of Advanced Manufacturing Technology*, 84(9-12), 1953-1961. <https://doi.org/10.1007/s00170-015-7859-7>
- Hernandez, R. J., Pacheco, J. A., Torres, J. E., and Vargas, J. A. (2013). Analysis of heat input effect on the mechanical properties of Al-6061-T6 alloy weld joints. *Materials in engineering*, 52, 556. <https://doi.org/10.1016/j.matdes.2013.05.081>
- Hosseinabadi, O. F., and Khedmati, M. R. (2021). A review on ultimate strength of aluminium structural elements and systems for marine applications. *Ocean Engineering*, 232, 109153. <https://doi.org/https://doi.org/10.1016/j.oceaneng.2021.109153>
- Huang, L., Hua, X., Wu, D., Jiang, Z., and Ye, Y. (2019). A study on the metallurgical and mechanical properties of a GMAW-welded Al-Mg alloy with different plate thicknesses. *Journal of Manufacturing Processes*, 37, 438-445.
<https://doi.org/https://doi.org/10.1016/j.jmapro.2018.12.017>
- Huang, Y., and Young, B. (2014). The art of coupon tests. *Journal of Constructional Steel Research*, 96, 159-175. <https://doi.org/10.1016/j.jcsr.2014.01.010>
- Ilman, M. N., Sriwijaya, R. A., Muslih, M. R., Triwibowo, N. A., and Sehon. (2020). Strength and fatigue crack growth behaviours of metal inert gas AA5083-H116 welded joints under in-process vibrational treatment. *Journal of Manufacturing Processes*, 59, 727-738.
<https://doi.org/https://doi.org/10.1016/j.jmapro.2020.10.035>
- James, M. N. (2011). Residual stress influences on structural reliability. *Engineering Failure Analysis*, 18(8), 1909-1920.
<https://doi.org/https://doi.org/10.1016/j.engfailanal.2011.06.005>
- Jesus, J. S., Costa, J. M., Loureiro, A., and Ferreira, J. M. (2017). Fatigue strength improvement of GMAW T-welds in AA 5083 by friction-stir processing. *International journal of fatigue*, 97, 124-134. <https://doi.org/10.1016/j.ijfatigue.2016.12.034>
- Khotiyan, S. K., and Kumar, S. (2014). Investigation of microstructure and mechanical properties of TIG and MIG Welding Using Aluminium Alloy. *Internal Journal of Education and Science Research Review*(90-96)

- KumarSingh, S., Mohan Tiwari, R., kumar, A., Kumar, S., QasimMurtaza, and Kumar, S. (2018). Mechanical properties and microstructure of Al-5083 by TIG. *Materials Today: Proceedings*, 5(1, Part 1), 819-822.
<https://doi.org/https://doi.org/10.1016/j.matpr.2017.11.152>
- Lakshminarayanan, A. K., Balasubramanian, V., and Elangovan, K. (2009). Effect of welding processes on tensile properties of AA6061 aluminum alloy joints. *The International Journal of Advanced Manufacturing Technology*, 40(3-4), 286-296.
<https://doi.org/10.1007/s00170-007-1325-0>
- Lasdon, L. S., Waren, A. D., Jain, A., and Ratner, M. (1978). Design and testing of a generalized reduced gradient code for nonlinear programming. *ACM Transactions on Mathematical Software (TOMS)*, 4(1), 34–50.
- Li, C., Ren, H., Zhu, Z., and Soares, C. G. (2018). Numerical investigation on the ultimate strength of aluminium integrally stiffened panels subjected to uniaxial compressive load. *Thin-Walled Structures*, 127, 221–234.
- Liu, Y., Wang, W., Xie, J., Sun, S., Wang, L., Qian, Y., Meng, Y., and Wei, Y. (2012). Microstructure and mechanical properties of aluminum 5083 weldments by gas tungsten arc and gas metal arc welding. *Materials Science and Engineering: A*, 549, 7-13.
<https://doi.org/10.1016/j.msea.2012.03.108>
- Lu, Y., Zhu, S., Zhao, Z., Chen, T., and Zeng, J. (2020). Numerical simulation of residual stresses in aluminum alloy welded joints. *Journal of Manufacturing Processes*, 50, 380-393. <https://doi.org/https://doi.org/10.1016/j.jmapro.2019.12.056>
- Masubuchi, K. (1980). *Analysis of Welded Structures*. Pergamon Press.
- McClung, R. C. (2007). A literature survey on the stability and significance of residual stresses during fatigue. *Fatigue & fracture of engineering materials & structures*, 30(3), 173-205.
<https://doi.org/10.1111/j.1460-2695.2007.01102.x>
- Mishra, V. D., Venkatachalam, S., Rao, B. C., and Murthy, H. (2023). Size effect stemming from specimen geometry on mechanical properties of an aluminum alloy. *Journal of Materials Engineering and Performance*, 32(2), 562–576.
- Mutombo, K., & Du, M. (2011). Corrosion Fatigue Behaviour of Aluminium 5083-H111 Welded Using Gas Metal Arc Welding Method. In InTech. <https://doi.org/10.5772/25991>
- Myhr, O. R., & Grong, Ø. (1991). Process modelling applied to 6082-T6 aluminium weldments—I. Reaction kinetics. *Acta Metallurgica et Materialia*, 39(11), 2693-2702.
[https://doi.org/https://doi.org/10.1016/0956-7151\(91\)90085-F](https://doi.org/https://doi.org/10.1016/0956-7151(91)90085-F)
- Najib, L. M., Alisibramulisi, A., Amin, N. M., Bakar, I. A. A., and Hasim, S. (2015). The Effect of Rolling Direction to the Tensile Properties of AA5083 Specimen. In CIEC 2014, Singapore.
- Nazemi, N. (2015). Identification of the mechanical properties in the heat-affected zone of aluminum welded structures (Publication Number 5485) University of Windsor]. Electronic Theses and Dissertations <https://scholar.uwindsor.ca/etd/5485>

- Nazemi, N., and Ghrib, F. (2019). Strength Characteristics of Heat-Affected Zones in Welded Aluminum Connections. *Journal of Engineering Mechanics*, 145(12), 04019103. [https://doi.org/10.1061/\(asce\)em.1943-7889.0001647](https://doi.org/10.1061/(asce)em.1943-7889.0001647)
- NI, 2019. LabVIEW NXG 3.1 User Manual, National Instruments, Austin, TX, <https://www.ni.com/documentation/en/labview/3.1/manual/manual-overview/>. Accessed 10 Dec. 2019.
- Ozturk, F., Sisman, A., Toros, S., Kilic, S., and Picu, R. C. (2010). Influence of aging treatment on mechanical properties of 6061 aluminum alloy. *Materials & Design*, 31(2), 972-975. <https://doi.org/https://doi.org/10.1016/j.matdes.2009.08.017>
- Paik, J. K. (2009). Mechanical properties of friction stir welded aluminum alloys 5083 and 5383. *International journal of naval architecture and ocean engineering*., 1(1), 39-49. <https://doi.org/10.2478/IJNAOE-2013-0005>
- Paik, J. K., Andrieu, C., and Cojeen, H. P. (2008). Mechanical Collapse Testing on Aluminum Stiffened Plate Structures for Marine Applications. *Marine Technology and SNAME News*, 45(04), 228-240. <https://doi.org/10.5957/mtl.2008.45.4.228>
- Paik, J. K., Hughes, O. F., Hess, P. E., and Renaud, C. (2005). Ultimate limit state design technology for aluminum multi-hull ship structures.
- Pérez, J. S., Ambriz, R. R., López, F. F. C., and Vigueras, D. J. (2016). Recovery of Mechanical Properties of a 6061-T6 Aluminum Weld by Heat Treatment After Welding. *Metallurgical and Materials Transactions A*, 47(7), 3412-3422. <https://doi.org/10.1007/s11661-016-3483-x>
- Poolperm, P., Nakkiew, W., and Naksuk, N. (2020). Finite element analysis of the effect of porosity on residual stress in 2024 aluminium alloy GTAW. *Materials Research Express*, 7(5), 056518. <https://doi.org/10.1088/2053-1591/ab906a>
- Portevin, A., & Le Chatelier, F. (1923). Comptes rendus de l'Academie des sciences,.
- Ramaswamy, A., Malarvizhi, S., and Balasubramanian, V. (2020). Effect of variants of gas metal arc welding process on tensile properties of AA6061-T6 aluminium alloy joints. *The International Journal of Advanced Manufacturing Technology*, 108(9), 2967-2983. <https://doi.org/10.1007/s00170-020-05602-5>
- Ramberg, W., & Osgood, W. R. (1943). Description of stress-strain curves by three parameters. NACA, Tech. No902.
- Rice, J. R., & Tracey, D. M. (1969). On the ductile enlargement of voids in triaxial stress fields*. *Journal of the mechanics and physics of solids*., 17(3), 201-217. [https://doi.org/10.1016/0022-5096\(69\)90033-7](https://doi.org/10.1016/0022-5096(69)90033-7)
- Romhanji, E., and Popović, M. (2006). Problems and prospect of Al-Mg alloys application in marine constructions. *Metalurgija : časopis Fakulteta, instituta i željezare Sisak*., 12(4), 297.
- Rossini, N. S., Dassisti, M., Benyounis, K. Y., and Olabi, A. G. (2012). Methods of measuring residual stresses in components. *Materials & Design*, 35, 572-588. <https://doi.org/10.1016/j.matdes.2011.08.022>

- Sarkar, A., Chatterjee, A., Barat, P., and Mukherjee, P. (2007). Comparative study of the Portevin-Le Chatelier effect in interstitial and substitutional alloy. *Materials Science and Engineering: A*, 459(1-2), 361-365.
- Sensharma, P., Collette, M., & Harrington, J. (2011). Effect of welded properties on aluminum structures, SSC-460. *Ship Structure Committee*.
- Siddiqui, R. A., Abdullah, H. A., and Al-Belushi, K. R. (2000). Influence of aging parameters on the mechanical properties of 6063 aluminium alloy. *Journal of Materials Processing Technology*, 102(1), 234-240. [https://doi.org/https://doi.org/10.1016/S0924-0136\(99\)00476-8](https://doi.org/https://doi.org/10.1016/S0924-0136(99)00476-8)
- Skejić, D., Dokšanović, T., Čudina, I., and Mazzolani, F. M. (2021). The basis for reliability-based mechanical properties of structural aluminium alloys. *Applied Sciences*, 11(10), 4485. <https://doi.org/10.3390/app11104485>
- Swanson, J. A. (2003). Ultimate strength prying models for bolted t-stub connections. <https://api.semanticscholar.org/CorpusID:110817931>
- Tercelj, M., Fazarinc, M., Kugler, G., and Perus, I. (2013). Influence of the chemical composition and process parameters on the mechanical properties of an extruded aluminium alloy for highly loaded structural parts. *Construction and Building Materials*, 44, 781-791. <https://doi.org/https://doi.org/10.1016/j.conbuildmat.2013.03.052>
- Tian, N., Wang, G., Zhou, Y., Liu, K., Zhao, G., and Zuo, L. (2018). Study of the Portevin-Le Chatelier (PLC) characteristics of a 5083 aluminum alloy sheet in two heat treatment states. *Materials*, 11(9).
- Torres, R. J. H. J. A. P. J. E., and Vargas, J. A. (2013). Analysis of heat input effect on the mechanical properties of Al-6061-T6 alloy weld joints. *Materials in engineering*, 52, 556. <https://doi.org/10.1016/j.matdes.2013.05.081>
- Tucker, M. T., Horstemeyer, M. F., Whittington, W. R., Solanki, K. N., and Gullett, P. M. (2010). The effect of varying strain rates and stress states on the plasticity, damage, and fracture of aluminum alloys. *Mechanics of Materials*, 42(10), 895-907. <https://doi.org/https://doi.org/10.1016/j.mechmat.2010.07.003>
- Wang, T., Hopperstad, O. S., Larsen, P. K., and Lademo, O. G. (2006). Evaluation of a finite element modelling approach for welded aluminium structures. *Computers & structures*, 84(29-30), 2016-2032.
- Woelke, P. B., Hiriyyur, B. K., Nahshon, K., and Hutchinson, J. W. (2017). A practical approach to modeling aluminum weld fracture for structural applications. *Engineering Fracture Mechanics*, 175, 72-85. <https://doi.org/https://doi.org/10.1016/j.engfracmech.2017.02.010>
- Yi, J., Cao, S.-f., Li, L.-x., Guo, P.-c., and Liu, K.-y. (2015). Effect of welding current on morphology and microstructure of Al alloy T-joint in double-pulsed MIG welding. *Transactions of Nonferrous Metals Society of China*, 25(10), 3204-3211. [https://doi.org/https://doi.org/10.1016/S1003-6326\(15\)63953-X](https://doi.org/https://doi.org/10.1016/S1003-6326(15)63953-X)
- Yi, J., Zhang, J.-m., Cao, S.-f., and Guo, P.-c. (2019). Effect of welding sequence on residual stress and deformation of 6061-T6 aluminium alloy automobile component. *Transactions of Nonferrous Metals Society of China*, 29(2), 287-295. [https://doi.org/https://doi.org/10.1016/S1003-6326\(19\)64938-1](https://doi.org/https://doi.org/10.1016/S1003-6326(19)64938-1)

- Yi, M.-S., and Park, J.-S. (2022). Study of Heat Source Model and Residual Stress Caused by Welding in GMAW of Al Alloy. *Metals*, 12(6), 891.
<https://doi.org/10.3390/met12060891>
- Yun, X., Wang, Z., and Gardner, L. (2021). Full-Range Stress–Strain Curves for Aluminum Alloys. *Journal of Structural Engineering*, 147(6), 04021060.
[https://doi.org/10.1061/\(ASCE\)ST.1943-541X.0002999](https://doi.org/10.1061/(ASCE)ST.1943-541X.0002999)
- Zha, Y., and Moan, T. (2001). Ultimate strength of stiffened aluminium panels with predominantly torsional failure modes. *Thin-Walled Structures*, 39(8), 631-648.
[https://doi.org/https://doi.org/10.1016/S0263-8231\(01\)00027-1](https://doi.org/https://doi.org/10.1016/S0263-8231(01)00027-1)
- Zhang, B., Liaw, P. K., Brechtel, J., Ren, J., Guo, X., and Zhang, Y. (2020a). Effects of Cu and Zn on microstructures and mechanical behavior of the medium-entropy aluminum alloy. *Journal of Alloys and Compounds*, 820, 153092.
<https://doi.org/https://doi.org/10.1016/j.jallcom.2019.153092>
- Zhang, F., Bower, A. F., and Curtin, W. A. (2012). The influence of serrated flow on necking in tensile specimens. *Acta Materialia*, 60(1), 43-50.
<https://doi.org/https://doi.org/10.1016/j.actamat.2011.09.008>
- Zhang, H. J., Zhang, G. J., Cai, C. B., Gao, H. M., and Wu, L. (2009). Numerical simulation of three-dimension stress field in double-sided double arc multipass welding process. *Materials Science and Engineering: A*, 499(1), 309-314.
<https://doi.org/https://doi.org/10.1016/j.msea.2007.10.119>
- Zhang, H.-R., Zhao, H., Wang, R., Liang, X.-X., and Zhu, Y. (2022). Coupling influences of elevated temperature and strain rate on the behaviour of 6061-T6 aluminium alloy used as construction material. *Structures*, 40, 596-606.
<https://doi.org/10.1016/j.istruc.2022.04.052>
- Zhang, L., Zhong, H., Li, S., Zhao, H., Chen, J., and Qi, L. (2020b). Microstructure, mechanical properties and fatigue crack growth behavior of friction stir welded joint of 6061-T6 aluminum alloy. *International journal of fatigue*, 135, 105556.
<https://doi.org/10.1016/j.ijfatigue.2020.105556>
- Zhao, S., Li, Y., Huang, R., and He, Z. (2021). Numerical study of the residual stress and welding deformation of mid-thick plate of AA6061-T6 in the multi-pass MIG welding process. *Journal of Mechanical Science and Technology*, 35(11), 4931-4942.
<https://doi.org/10.1007/s12206-021-1012-3>